

University of Rijeka
Faculty of Engineering

Tomislav Bazina

**Data-Driven Characterization of Grip
Strength and Grasp-Oriented
Kinematics in Rehabilitation Robotics**

Doctoral Thesis

Rijeka, 2025

University of Rijeka
Faculty of Engineering



Tomislav Bazina

Data-Driven Characterization of Grip Strength and Grasp-Oriented Kinematics in Rehabilitation Robotics

Doctoral Thesis

Supervisor:
Assoc. Prof. D. Sc. Ervin Kamenar

Rijeka, 2025

Sveučilište u Rijeci
Tehnički Fakultet



Tomislav Bazina

**Podatkovno vođena karakterizacija
kinematike i snage hvatova za
primjenu u rehabilitacijskoj robotici**

Doktorski rad

Mentor:
izv. prof. dr. sc. Ervin Kamenar

Rijeka, 2025.

Doctoral thesis supervisor: Assoc. Prof. D. Sc. Ervin Kamenar, University of Rijeka, Faculty of Engineering, Croatia

The doctoral thesis was defended on _____ at the University of Rijeka, Faculty of Engineering, Croatia, in front of the following Evaluation Committee:

1. _____
2. _____
3. _____

I dedicate this thesis to my wife, who supported me through countless hours, and to my daughter, whose smile provided me with the motivation I needed.

Acknowledgements

I express my gratitude to those who supported me throughout my doctoral journey.

I am deeply grateful to my supervisor, Assoc. Prof. Ervin Kamenar, for his patience, help, and friendship during my doctoral study. I thank Prof. Saša Zelenika for mentoring me during the first three years and improving the last thesis chapter, and my colleagues from the Department of Engineering Design for their support.

Thanks to my students who participated in the experiments, especially Marko Kladarić for his contributions to the rehabilitation device. I appreciate Assoc. Prof. Goran Gregov for his expertise in pneumatics during device design and Assoc. Prof. Ivan Volarić for his assistance with signal processing.

My appreciation goes to Prof. D. Sc. Igor Mezić for valuable insights regarding the operator-theoretic approach to nonlinear dynamical systems, and to my colleagues at AIMdyn Inc. for solving complex and engaging problems together.

To my friends David and Jelena, thank you for the joy you brought during this period. I am grateful to my parents and family for their unwavering support.

Finally, I give my deepest gratitude to my wife Virna for her endless patience and unconditional support, and to my daughter Aria, who is my greatest motivation.

The following grants supported this research:

- Air Force Office of Scientific Research: *Koopman Operator Theoretic Methods for Efficient Training and Analysis of Deep Neural Networks*, FA9550-22-1-0531 (PI: M. Fonoberova; Co-PI: W. Redman)
- University of Rijeka grants: *Rehabilitation devices based on soft robotics and bio-mechatronic sensors*, uniri-iskusni-tehnic-23-47 (PI: E. Kamenar); *Development of an advanced rehabilitation device using machine learning methods*, UNIRI-INOVA-1-22-10 (PI: E. Kamenar); *Development and design of soft pneumatic actuators for multi-axis motion systems*, uniri-iskusni-tehnic-23-174 (PI: G. Gregov); *Advanced mechatronics devices for smart technological solutions*, uniri-tehnic-18-32 (PI: S. Zelenika)

Abstract

This thesis advances anthropomorphic soft robotic devices for hand rehabilitation in patients with neurological disorders, such as stroke and multiple sclerosis, focusing on restoring grasping capabilities needed for activities of daily living. The research integrates three complementary methodological approaches.

First, it establishes a real-time system for estimating and predicting grip force using surface electromyography. Using only one sensing position with optimized spectral masking and Koopman Operator Theory, the method achieves $\sim 5.5\%$ error for grip force estimation and $\sim 17.9\%$ for short-term predictions, with processing times of just 30 ms, making it suitable for real-time adaptive assistance based on patient volition.

Second, it develops simplified hand kinematic models by analyzing data from 77 participants performing 23 functional grasps. The approach identifies 116 highly correlated joint relationships, models them using regularized generalized linear and mixed-effects models, and clusters into 30 similar model groups. This reduces the degrees of freedom during grasping to 5 to 15 while maintaining high accuracy, offering a practical basis for designing rehabilitation devices with reduced complexity.

Third, it details the design and fabrication of a 3D-printed soft robotic rehabilitation glove based on reduced hand kinematics. The innovative finger soft pneumatic actuator combines cylindrical and ribbed geometries with a reinforcing element, creating an asymmetric bellows actuator validated through finite element method simulations and a modified pseudo-rigid-body model with positioning errors below 3.8 mm.

These advances in EMG-based force feedback, sparse kinematic modeling, and soft actuator design constitute a comprehensive framework for developing effective hand rehabilitation devices.

Keywords: Rehabilitation Robotics, Hand Rehabilitation, Surface Electromyography (sEMG), Grip Force Prediction, Simplified Hand Kinematic Models, Soft Rehabilitation Glove Development

Prošireni sažetak

Ova disertacija doprinosi razvoju antropomorfnih mekih robotskih uređaja za rehabilitaciju šake kod pacijenata s neurološkim poremećajima, uključujući moždani udar i multiplu sklerozu, s ciljem učinkovitijeg obnavljanja sposobnosti hvatanja potrebne za svakodnevne aktivnosti (ADL). Rad integrira tri metodološka pristupa: predviđanje sile za povratnu vezu, reducirano kinematičko modeliranje i inovativni razvoj aktuatora.

Prvi dio disertacije predstavlja novu metodu u stvarnom vremenu za procjenu i predviđanje sile stiska tijekom cilindričnog hvata korištenjem površinske elektromiografije (sEMG). Robotska rehabilitacija temeljena na EMG-u pokazala je poboljšanu funkcionalnu obnovu u usporedbi s konvencionalnim metodama terapije prisilno inducirano pokreta i tradicionalne fizikalne terapije. Metodologija omogućuje izravan pristup kontrolnoj varijabli—sili stiska—što omogućuje robotsku asistenciju koja se adaptivno prilagođava voljnom djelovanju pacijenta. Dok suvremene metode zahtijevaju više sEMG mjernih pozicija za točna predviđanja, predstavljena metoda postiže usporedive rezultate koristeći samo jednu mjernu poziciju kroz optimiziranu spektralnu masku tijekom obrade signala i pristup temeljen na teoriji Koopmanovog operatora (KOT). Korištenjem naprednih tehnika transformacije podataka sa statičkim Koopmanovim operatorom omogućuje se procjena trenutne sile stiska šake iz obrađenih EMG signala, dok se dinamički Koopmanov operator primjenjuje za kratkoročno predviđanje sile stiska na temelju tih procjena. Eksperimentalna validacija s 13 sudionika pokazala je robusnu izvedbu na dvije sEMG mjerne pozicije na podlaktici, bez značajne osjetljivosti na položaj elektroda. Metoda postiže ponderiranu srednju apsolutnu postotnu pogrešku (wMAPE) od približno 5.5% za procjenu sile stiska i 17.9% za kratkoročna predviđanja tijekom horizonta od 0.5 s. Značajno je da algoritam obrađuje, procjenjuje i predviđa silu stiska unutar vremenskog prozora od 0.5 s sEMG podataka u samo 30 ms, što ga čini pogodnim za implementaciju u stvarnom vremenu u rehabilitacijskim uređajima.

U drugom dijelu disertacije razvijaju se interpretabilni reducirani kinematički modeli hvatova šakom za rješavanje izazova prevelike složenosti prilikom konstrukcije

rehabilitacijskih uređaja. Analizom najvećeg dostupnog skupa podataka o kinematici šake, s podacima od 77 sudionika koji izvode 23 funkcionalna hvata vezana uz ADL, ovo istraživanje uvodi novi pristup za modeliranje međuzglobnih ovisnosti unutar prsta tijekom fleksije/ekstenzije (FE). Predložena metoda pojednostavljuje modeliranje uspostavljanjem izravnih zavisnosti između parova zglobova, identificirajući 116 visoko koreliranih odnosa koji su modelirani pomoću regulariziranih generaliziranih linearnih modela (GLM) u kombinaciji s ponderiranim linearnim modelima miješanih učinaka (LME). Hijerarhijsko grupiranje dodatno konsolidira ove odnose u 30 različitih klastera uz zadržavanje visoke točnosti. Ovaj sustavni pristup značajno smanjuje stupnjeve slobode (DOF) potrebne za modeliranje FE tijekom hvatanja na 5–15, nudeći praktičnu osnovu za razvoj protetičkih i rehabilitacijskih uređaja sa značajnim smanjenjem mehaničke i upravljačke složenosti.

Treći dio disertacije predstavlja sveobuhvatan proces za konstruiranje, simulaciju i izradu 3D-tiskane meke robotske rehabilitacijske rukavice. Inovativni meki pneumatski aktuator za prst (SPA) razvijen je koristeći kinematička svojstva i radni prostor anatomske prstiju kao konstrukcijsku osnovu. Aktuator integrira cilindričnu geometriju s rebrima i ojačavajućim elementom—debljom, manje rastezljivom strukturom—na donjoj strani, što rezultira asimetričnim cilindričnim aktuatorom s mješovitom pogonjenim pozitivnim tlakom. Dobiveni segmentirani kinematički modeli krutog tijela za aktuatore kažiprsta i malog prsta omogućuju precizno upravljanje pokretima. Simulacije metodom konačnih elemenata (FEM) pri različitim tlakovima između 0 to (numerical range) 3 bar potvrdile su performanse aktuatora i njegovu usklađenost s putanjama ljudskog prsta. Za pojednostavljenje iterativnog procesa konstruiranja, uveden je modificirani model pseudo-krutog tijela (PRB), značajno smanjujući računalnu složenost uz zadržavanje odstupanja u pozicioniranju ispod 3.8 mm u usporedbi s FEM simulacijama. Aktuatori su uspješno izrađeni korištenjem termoplastičnog poliuretana (TPU), a ergonomsko testiranje meke rukavice pokazalo je njenu funkcionalnost.

Ova disertacija uvodi nove metode obrade EMG signala za povratnu vezu o sili, reducirane kinematičke modele hvatova i okvir za razvoj mekih robotskih aktuatora. Integracija ovih pristupa unaprjeđuje razvoj personaliziranih rehabilitacijskih uređaja za širok raspon funkcionalnih hvatova ključnih za svakodnevne aktivnosti.

Ključne riječi: rehabilitacijska robotika, rehabilitacija šake, površinska elektromiografija (sEMG), predviđanje sile hvata, reducirani kinematički modeli šake, razvoj meke rehabilitacijske rukavice

Contents

1	Introduction	1
1.1	Contributions of the Dissertation	6
1.2	Structure of the Dissertation	6
2	EMG-based Forecasting of Hand Grip Force Using Koopman Framework	9
2.1	Hand Grip Force Forecasting: State-of-the-Art	10
2.2	Experimental Setup and Design	13
2.2.1	Equipment and Measurement Setup	13
2.2.2	Design of Experiment	14
2.3	Sensitivity Analysis and Procedural Parameter Optimization	16
2.3.1	Preliminary Sensitivity Analysis	18
2.3.2	Iterative Multi-Step Sensitivity Analysis and Optimization	20
2.4	Real-Time Forecasting of Hand Grip Force	24
2.4.1	Koopman Operator Theory Introduction	24
2.4.2	Estimating Grip Force	25
2.4.3	Forecasting Grip Force	29
2.5	Results and Experimental Validation	33
3	Grasp-oriented reduction of hand kinematics in robotic rehabilitation	41
3.1	Reducing Hand Kinematics: State-of-the-Art	42
3.2	Data Cleaning, Exploration and Joint Dependency Identification	45
3.2.1	Data Relabeling and Preprocessing	45
3.2.2	Intra-Finger Correlation Analysis	52
3.3	Dependency-Movement Relationship Modeling	59
3.3.1	Random and Fixed Effect Predictors	62

3.3.2	Model Error Metric Analysis	64
3.3.3	Clustering Based on Model Coefficient Analysis	66
4	Design and Development of a Rehabilitation Glove: A Soft Robotics Approach	71
4.1	Soft Rehabilitation Gloves Design: State-of-the-Art	73
4.2	Kinematics Characterization and Implementation of the Hand Model	74
4.2.1	Geometric Model of Index Finger	75
4.2.2	Forward Kinematics – Modified Denavit-Hartenberg Convention	76
4.2.3	Joint Dependency Effects on ROMs and Anatomical Limits	80
4.2.4	Inverse Kinematics Solvers	82
4.3	Kinematic Characterization, Morphology, and Modeling of SPAs	86
4.3.1	Kinematic Characterization Using Segmented Rigid Model Approach	86
4.3.2	Finger SPA Specifications	89
4.3.3	Finite Element Modeling	90
4.3.4	Pseudo Rigid Body Modeling Approach	99
4.4	Soft Rehabilitation Glove Prototyping and Experimental Validation	113
5	Conclusion	117
	Bibliography	123
	Nomenclature	131
	List of Figures	139
	List of Tables	141
	Appendix A Raw sEMG Measurements, Grip Force and Processed EMG Data	143
	Appendix B LME Model Coefficients’ Detailed Analysis and Model Error Metric Analyses	147

Chapter 1

Introduction

Hand function impairments pose a significant global health challenge, impacting activities of daily living (ADLs) and imposing substantial societal burden (O’Sullivan et al., 2019). These impairments primarily result from neurological disorders like stroke and multiple sclerosis, and musculoskeletal conditions such as arthritis. Stroke affects over 12 million individuals annually worldwide, with approximately one in four adults over age 25 experiencing it in their lifetime (Feigin et al., 2025). Despite declining age-adjusted rates, absolute case numbers continue rising due to aging populations and lifestyle factors such as hypertension and obesity (Cheng et al., 2024).

The impact on hand function post-stroke is both severe and persistent. Welmer et al. (2008) found that 70% of stroke patients have limited fine hand use in the first week, improving to 41% at three months, but plateauing with 45% still exhibiting limitations at 18 months. This chronic impairment underscores the need for effective rehabilitation strategies.

Low- and middle-income countries bear the most significant stroke burden while lacking adequate rehabilitation infrastructure (Feigin et al., 2025; Kayola et al., 2023). Even high-income countries face challenges through workforce shortages and therapist burnout, compromising rehabilitation quality (Patel and Bartholomew, 2021). The combination of increasing stroke incidence, rehabilitation specialist shortages, and rising healthcare costs necessitates innovative, scalable solutions capable of delivering intensive therapy necessary for optimal recovery (Lang et al., 2015). Addressing these challenges requires evidence-based strategies that operate within resource constraints while maximizing functional recovery.

Neuro-rehabilitation following stroke employs a multidisciplinary approach to restore neurological function by harnessing brain neuroplasticity—the capacity to reorganize neural circuitry in response to experience. Effective rehabilitation centers on structured, repetitive, task-specific training that stimulates adaptive neural reorganization (Dobkin, 2004).

Evidence-based interventions include constraint-induced movement therapy (CIMT, which restrains the unaffected limb while promoting intensive practice with the affected side), functional electrical stimulation (FES, which applies electrical impulses to nerves causing paralyzed muscles to contract), virtual reality (VR) environments (immersive, interactive simulations that increase patient engagement and motivation through customized scenarios), and robotic-assisted therapy systems (devices that automate repetitive exercises while providing precise assistance, detailed progress tracking, and consistent high-intensity training). These approaches facilitate neural rewiring by engaging patients in goal-directed activities that mirror daily tasks, reinforcing functional neural pathways through context-specific practice (Maier et al., 2019).

Optimal timing and intensity are critical parameters in rehabilitation protocols. Current guidelines recommend initiating therapy within days post-stroke to leverage heightened neuroplasticity, though the exact therapeutic window remains under investigation. Substantial evidence demonstrates that higher-intensity interventions consistently yield superior motor recovery outcomes (Lang et al., 2015; Maier et al., 2019). This dose-response relationship highlights the need for rehabilitation strategies that deliver sufficient therapeutic intensity within existing healthcare constraints.

Rehabilitation robotics emerges as a promising frontier at the intersection of robotics, neuroscience, and biomedical engineering, offering sophisticated solutions to the challenges of stroke rehabilitation (Colombo and Sanguineti, 2018). This interdisciplinary field has developed specialized devices that deliver precisely controlled, repetitive, task-specific elements for stimulating the neural reorganization necessary for functional recovery. For stroke survivors experiencing hemiparesis or spasticity, these robotic systems provide significant advantages, including the ability to deliver consistent, high-intensity therapy that far exceeds the repetition counts possible in conventional treatment. Additionally, integrated sensor systems enable continuous, quantitative assessment of movement parameters such as range of motion, force production, and movement quality. This allows for objective tracking of recovery trajectories and data-driven therapy adjustments.

Despite these advantages, traditional rehabilitation robots employing rigid exoskeletal designs present significant limitations when applied to the biomechanically complex hand. The mechanical constraints of rigid structures frequently fail to accommodate the hand's intricate articular geometry and natural movement patterns, resulting in kinematic misalignment during therapy. This misalignment often manifests as compensatory movements—maladaptive motor strategies that can reinforce non-physiological movement patterns and potentially impede functional recovery. Furthermore, unnatural movement constraints of rigid systems can diminish patient engagement and motivation, critical factors for optimal therapeutic outcomes (Peng and Huang, 2019). These limitations have driven the exploration of alternative approaches that better align with the hand's natural biomechanics while maintaining the quantitative advantages of robotic rehabilitation.

Soft robotics has emerged as a solution, characterized by its compliant, adaptable actuators that fundamentally reimagine how robotic systems interact with the human body (Chu and Patterson, 2018). This rapidly evolving field represents a significant departure from conventional rigid robotic systems through its biomimetic approach to design and actuation. Unlike their rigid counterparts, soft robotic gloves utilize materials and mechanisms that emulate the viscoelastic properties of biological muscle-tendon complexes, thereby facilitating physiologically appropriate force transmission patterns, superior conformity to complex joint kinematics, and inherent mechanical compliance that adapts to individual anatomical variations (Polygerinos et al., 2015).

The biomechanical advantages of soft robotic systems are particularly significant in hand rehabilitation contexts with extraordinarily complex articular geometry and fine motor control requirements. By employing flexible materials and distributed actuation mechanisms, these systems can facilitate functional grasp patterns without imposing constrained movement trajectories that might otherwise promote compensatory strategies (Chu and Patterson, 2018). This capacity for accommodating natural movement variability while simultaneously providing targeted assistance represents a critical advancement for rehabilitation of neurological conditions such as stroke and multiple sclerosis, where restoration of hand functionality directly impacts independence in ADLs (Proulx et al., 2020).

Preliminary clinical investigations into soft robotic glove interventions have yielded promising indicators regarding user experience and engagement metrics. Participants generally report high satisfaction levels and demonstrate increased participation in therapeutic activities when utilizing these devices. However, translating these positive

experiential outcomes into standardized clinical practice requires substantial additional validation (Proulx et al., 2020).

Hand rehabilitation devices must align with the hand’s natural biomechanics while addressing its inherent complexity. The human hand, with its 27 bones, 21 intrinsic muscles, and more than 20 degrees of freedom excluding the wrist, represents one of nature’s most intricate mechanical systems (Sobinov and Bensmaia, 2021). Attempting to replicate this complexity entirely through multi-joint linkages and actuators inevitably results in rehabilitation devices that are excessively bulky, heavy, and prohibitively expensive to manufacture.

Reducing this complexity is, therefore, essential for developing clinically viable, patient-friendly rehabilitation gloves with improved compliance, scalability, and modularity. Since hand biomechanical models form the foundation of rehabilitation device design, overly detailed models unnecessarily complicate development without proportional functional benefits. Instead, simplified yet interpretable kinematic models that accurately represent essential hand movements provide a more effective development pathway. By strategically prioritizing grasp patterns critical for activities of daily living, these models enable the creation of lightweight, cost-effective devices that achieve their intended therapeutic functionality without extraneous complexity.

Adaptive assistance—a fundamental principle in rehabilitation robotics—utilizes real-time biosignals like EMG to dynamically adjust support based on patient effort, amplifying rather than replacing natural motor commands. These systems integrate sensor data with machine learning algorithms to provide precisely calibrated assistance as needed, detecting motor intent while minimizing the “slacking” phenomenon often observed in passive robotic therapy. Research by Arantes et al. (2023) demonstrates that EMG-based adaptive controllers effectively reduce slacking in stroke patients by necessitating active muscle engagement during task performance. Another approach deliberately emulates skilled therapist techniques, incorporating principles of task variability and active participation that drive neuroplasticity (Hasson et al., 2023). By maintaining the patient’s volition in rehabilitation, adaptive assistance promotes improved motor outcomes and enhanced neural reorganization—key factors in meaningful functional recovery.

Despite significant advances in soft robotics, critical barriers remain in translating research prototypes into clinically viable devices, including regulatory challenges, integration within healthcare workflows, and cost-effectiveness concerns.

Building on these insights, this research establishes a structured framework for developing soft robotic rehabilitation devices through three complementary approaches:

- **EMG-based adaptive assistance:** Real-time grip force estimation from sEMG signals that accurately represents voluntary effort, enabling dynamic support adjustment based on patient capabilities.
- **Simplified kinematic modeling:** Interpretable reduced-order models based on hand synergies that maintain essential biomechanical properties while minimizing actuation complexity.
- **Grasp-oriented design:** Optimized soft actuators prioritizing ADL-related functional grasps through iterative simulation and fabrication processes.

By integrating EMG-driven force estimation with biomechanically-informed kinematic models and purpose-designed soft actuators, this framework enables the development of rehabilitation devices that simultaneously address effectiveness and practical implementation challenges. These complementary innovations advance soft robotic rehabilitation toward scalable solutions, providing personalized therapy adaptive to patient capabilities while maintaining the affordability and usability.

Research Aims and Hypotheses

According to the above considerations, the aims of this research are threefold. First, it seeks to develop a framework based on Koopman operator theory for real-time signal processing and modeling to assess and short-term predict hand grip strength. Second, it aims to devise applicable grasp-oriented, kinematically reduced hand models by introducing intra-finger joint dependencies to simplify and enhance the accuracy of rehabilitation-oriented hand modeling. Finally, the research focuses on developing a prototype of a hand rehabilitation device using a soft robotic approach.

The research hypotheses of this thesis are as follows:

- Hand grip, measured on one sensing position via sEMG, is highly correlated with forearm muscle activity. Grip force can be assessed and predicted in real time using a data-driven approach.
- Complex hand kinematics during grasping can be significantly simplified and generalized by introducing 1-to-1 dependencies.

- Simplified hand kinematic models, combined with soft-actuator modeling techniques, can be leveraged to design and fabricate 3D-printed soft robotic devices tailored for rehabilitation purposes.

1.1 Contributions of the Dissertation

The main contributions of this work are as follows:

1. **Signal processing and grip force prediction:** We optimized EMG signal processing methods, achieving high peak cross-correlations between EMG and grip force signals using a single sensing position on the forearm, enhancing the accuracy of grip force estimation.
2. **Real-time execution and adaptive assistance:** We developed a Koopman-based data-driven approach for real-time grip force estimation and short-term prediction. This approach enables adaptive assistance by dynamically supplementing patients' voluntary efforts with only the necessary force, advancing predictive intent recognition for improved rehabilitation outcomes.
3. **Intra-finger dependency modeling:** We established motion patterns for intra-finger dependencies across subjects, generating simplified yet accurate models that significantly reduce the degrees of freedom (DOFs) involved in grasping. Additionally, we identified clusters of similar dependencies across different grasps, streamlining human hand modeling while preserving precision.
4. **Soft robotics design:** We devised an iterative methodology for designing, modeling, and fabricating 3D-printed soft actuators tailored for a rehabilitation glove. An initial prototype was developed and tested to validate functionality and usability in rehabilitation applications.

1.2 Structure of the Dissertation

This thesis is structured into five chapters, complemented by appendices, offering a systematic and detailed presentation of the research conducted. The graphical abstract given as Figure 1.1 provides a visual overview of the thesis structure and the key methodology used to achieve the research objectives. The elements depicted in the

abstract correspond to specific chapters in the thesis, which explore these topics in depth.

Chapter 1 outlines the scientific motivation underlying the study, details the research aims and hypotheses, and highlights the research contributions.

Chapter 2 explores time-series data on muscle activity using sEMG alongside grip force measurements with a dynamometer. Advanced signal processing techniques were applied to extract features strongly correlated with grip force, and offline optimization enhanced model accuracy. Finally, Koopman operator theory was used to estimate grip force during medium wrap using a single sEMG sensor pair.

Chapter 3 uncovers intra-finger dependencies during finger flexion and extension by analyzing trajectories from 23 functional movements—grasps—involving 77 test subjects. The process includes data cleaning, correlation analysis to identify 116 dependency-movement relationships, and the use of regularized linear models to select uncorrelated predictors. A linear mixed-effect model and agglomerative clustering are then applied to balance accuracy and reduction, enabling grasp modeling with just 5–15 degrees of freedom.

Chapter 4 details the design, simulation, and development of a rehabilitation glove prototype powered by soft pneumatic actuators. A geometric model of the index finger and kinematic analysis informed the design of an asymmetric bellow actuator optimized for ADL workspace requirements. FEM simulations validated its performance, while a simplified pseudo-rigid-body (PRB) model streamlined the design process. Fabricated with TPU for durability, the actuators were assembled into a prototype glove, which ergonomic testing confirmed as suitable for rehabilitation applications.

Chapter 5 summarizes the key findings of the research and outlines the necessary next steps to integrate the presented components into a functional rehabilitation device.

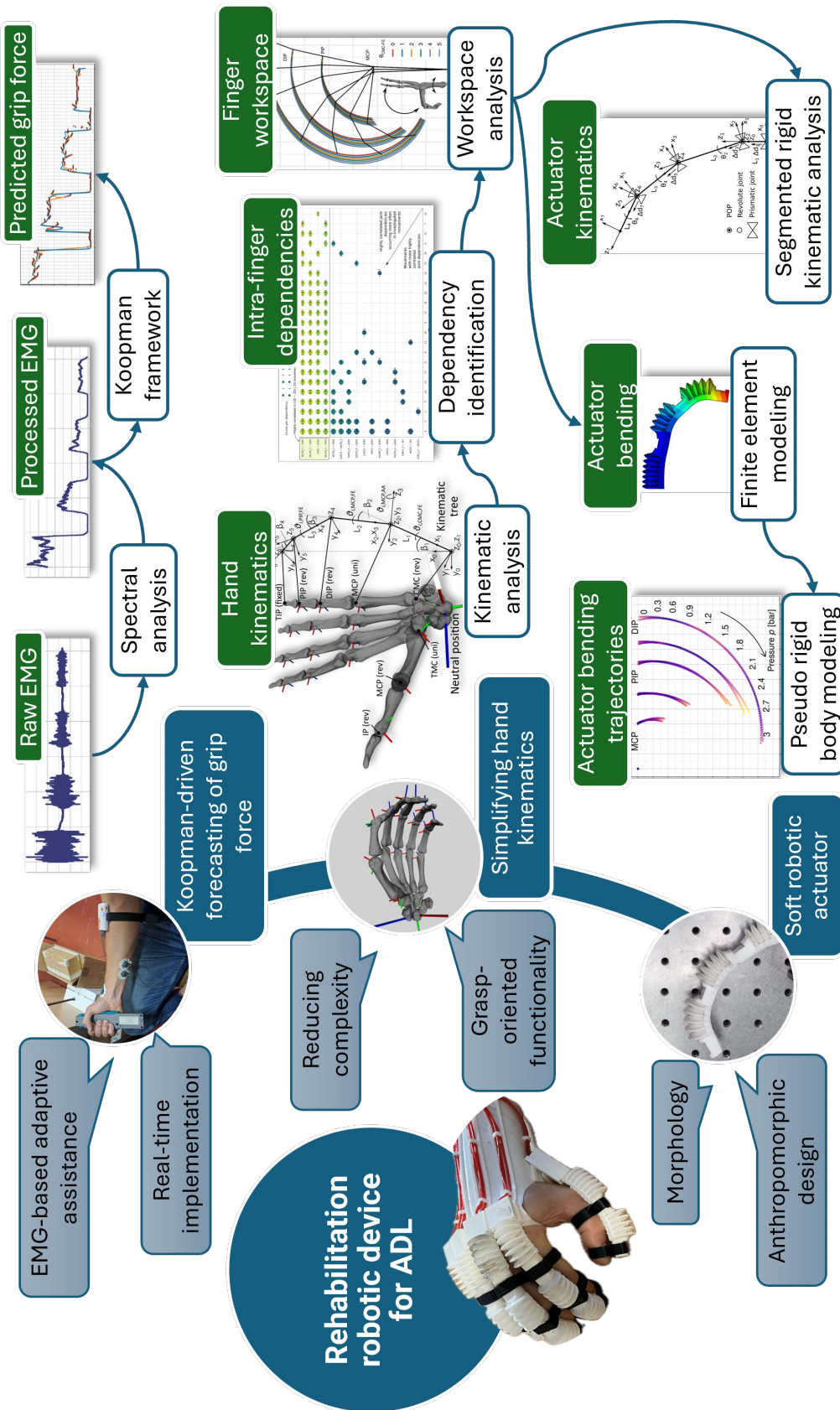


Figure 1.1 Visual overview of the thesis structure

Chapter 2

EMG-based Forecasting of Hand Grip Force Using Koopman Framework

THIS chapter introduces a novel method for accurately estimating grip force during medium wrap using a single surface electromyography (sEMG) sensor pair, addressing the challenge of increasing sensor demands for precise predictions¹. EMG-based robotic rehabilitation surpasses traditional physical therapy methods by enhancing motor recovery, reducing spasticity, and boosting patient engagement.

We conducted sEMG measurements on 13 participants at two forearm positions, with validation performed using a hand dynamometer.

The methodology employs flexible signal-processing steps that achieve high peak cross-correlations between the processed sEMG signal (reflecting meaningful muscle activity) and grip force. Sensitivity analysis identified influential parameters.

Using a data-driven Koopman operator theory-based approach and problem-tailored data-lifting techniques, a method was developed for estimating and short-term predicting grip force from processed sEMG signals.

We achieved a weighted mean absolute percentage error (wMAPE) of $\sim 5.5\%$ for estimated grip force and $\sim 17.9\%$ for predictions with a 0.5-second horizon. The method demonstrated robustness to electrode positioning, as the sensing location had no significant effect on error metrics. Additionally, the algorithm processes, estimates, and predicts a 0.5-second sEMG signal batch in ~ 30 ms, enabling real-time implementation.

¹Bazina et al. (2024a)

Chapter Contribution

The key contributions of this chapter can be summarized as:

- Development and optimization of a composition of sEMG signal processing steps that achieve high peak cross-correlations between sEMG and grip force signals.
- Introduction of a novel Koopman-based, data-driven approach with problem-specific observables for estimation and short-term prediction of grip force during both transient and plateau phases.
- Design of a fast-executing methodology suitable for real-time implementation, utilizing a single forearm sensing position and a three-electrode system.

Ethical Considerations

Consent was obtained from all participants prior to their involvement in the study. The research was conducted under the supervision of the University of Rijeka Faculty of Engineering Ethics Committee, with reference number 2409.17340.

2.1 Hand Grip Force Forecasting: State-of-the-Art

Electromyography (EMG)-based robotic rehabilitation outperforms conventional methods, such as constraint-induced movement and physical therapy. This approach improves motor recovery, reduces spasticity, and enhances patient engagement by maximizing their voluntary action Huo et al. (2023). Estimating grip force from real-time EMG signals enables direct access to the control variable—force—allowing robotic assistance to supplement patients’ voluntary effort adaptively.

The idea of measuring grip force through muscle activity using non-invasive surface electromyography (sEMG) relies on motor units (MU), groups of muscle fibers activated by the brain motor neurons. The resulting EMG signal is an inference of firing signals from each MU, referred to as motor unit action potentials (MUAPs). Various factors affect the variability of the EMG signal, including electrode placement, size, and inter-electrode distance, as well as tissue properties such as fat layers and skin conductivity, the temporal and spectral features of firing patterns, and cross-talk from adjacent muscles Stegeman et al. (2000).

In Ma et al. (2020a), the authors predicted pinching force using a 6-channel sEMG sleeve, focusing on the RMS feature of the signal. They applied a gene expression programming algorithm and reported RMSE errors ranging from 7.5 to 8.5 %, with cross-correlation coefficients reaching up to 95 %. The study analyzed four levels of maximum voluntary contraction (MVC)—20, 40, 60 and 80 %—but lacked forecasts during the transient states between these levels. In Khan et al. (2024), the authors utilized sEMG with four bipolar electrodes on the forearm along with finger force signals to predict the grip force. They used five EMG signal features and eleven finger force features, achieving a mean accuracy of ~ 90 % for grip force prediction during the transient phase. The study identified that the optimal sensor configuration stabilized at three sensing positions with 2 to 4 features.

Electrode positioning for grip force sensing on the forearm was also explored in Barański and Kozupa (2014), where sensing near the brachioradialis muscle was identified as optimal, based solely on EMG signal strength. In Siavashani et al. (2023), EMG signals were collected using an eight-channel Myo armband. A Long Short-Term Memory (LSTM) network predicted normalized pinching force 1, 3 and 5 s ahead directly from the EMG data. Additionally, Zhang et al. (2021) used eight sEMG sensors and 24 healthy subjects to demonstrate that extrinsic muscle coordination was more reliable in predicting grip and pinch force levels. This was attributed to its greater sensitivity to force changes compared to intrinsic muscles.

Additionally, in Martinez et al. (2020a), online predictions of gripping force were obtained from 8 sEMG sensors placed on the forearms of 16 participants. The model included ten features extracted from the EMG signal. Predictions were made 330 ms ahead using the elastic net regression algorithm, resulting in errors of 2 % of MVC.

Several studies, such as Martinez et al. (2020a,b), have explored predicting gripping force during the transient phase of the EMG signal—the initial burst that occurs as the muscle begins exerting force. In Martinez et al. (2020b), a high-density sEMG setup with 192 acquisition channels was used on 12 subjects to forecast the grasp force. This approach utilized a comprehensive set of ten signal features with a regularized linear regression model. The method achieved highly accurate predictions, with absolute errors as low as 2.5 % of the MVC. Similarly, Martinez et al. (2020a) showcased a technique for real-time gripping force predictions using eight sEMG sensors placed on the forearms of 16 participants. The approach involved extracting ten distinct features from the sEMG signals, which were then used as inputs to an elastic net regression

model. This model predicted grip force for the subsequent 330-millisecond interval, achieving high accuracy with an error of only 2% relative to MVC.

Based on the above analysis and the findings presented in Wu et al. (2021), it is clear that although most research has demonstrated favorable accuracy outcomes, it heavily depends on an ever-growing number of sEMG sensors to predict grasping force accurately. Furthermore, many existing methods tend to neglect advanced signal processing techniques, essential for isolating the meaningful components of the raw EMG signal. This clean signal is critical for the causal modeling of the grip force, yet it is frequently contaminated by noise. Additionally, forecasts during the transient state are seldom considered in existing approaches. Our study is the first to introduce an online modeling and signal-processing framework for estimating and short-term forecasting grip force, utilizing Koopman operator theory (KOT) Mezić (2005) while limiting the number of sEMG sensing positions to just one. We apply KOT to represent nonlinear dynamics through linear operators, distinguishing between "dynamic" and "static" types Mezić (2021). Instead of acting directly on the system's state, these operators operate on observables—functions that map the state to scalar or vector values. The dynamic operator advances observables over time, making it ideal for short-term grip force prediction, while the static operator maps observables across different spaces, enabling real-time estimation of grip force from EMG signals.

An important step of this research is the signal processing, which is vital for making proper inferences from EMG signals that are often heavily influenced by noise and muscle cross-talk. Typically, the signals are processed using notch filtering at 50 Hz to remove ground noise Khan et al. (2024), bandpass filtering between 10 to 500 Hz to eliminate artifacts caused by wire movement (Martinez et al., 2020a,b; Wu et al., 2021; Zhang et al., 2021), and bandpass filtering between 100 to 500 Hz (Barański and Kozupa, 2014). Additionally, bandpass filtering is applied to isolate power spectrum peaks in the 20 to 60 Hz range (Siavashani et al., 2023).

Unlike the typical filtering approaches, our focus was on signal processing designed to extract only the meaningful features from the sEMG signal—specifically, those strongly correlated with grip force. These difficult-to-identify signal components primarily contribute to the measured grip force and align with the structural approach to sEMG modeling outlined in Stegeman et al. (2000). It suggests that recruiting MUs is essential for generating muscle force. As more MUs are recruited, the muscle generates greater force, with the firing rate of each MU further increasing this force. Typically, the firing rates of MUs rise almost linearly with the muscle's force output. These firing patterns,

along with the interference between active MUs, characterize the measured sEMG signal. To isolate meaningful signal components from unwanted noise, we developed a spectral mask that selectively targets specific spectral elements by utilizing Fast Fourier Transformation (FFT) and sensitivity analysis (SA). These features can then be used within the KOT framework for improved modeling and prediction.

2.2 Experimental Setup and Design

This section details the hardware setup and experimental methods for collecting simultaneous EMG and grip force time-series data, including device selection, calibration protocols, electrode placement, and the 2-factor randomized block design methodology.

2.2.1 Equipment and Measurement Setup

Two wireless devices connected via Bluetooth were used for simultaneous data collection: the Shimmer3 EMG Unit² for muscle activity detection and the Vernier Go Direct® Hand Dynamometer³ for grip force measurement. The EMG unit records electrical signals from the skin surface, reflecting muscle contractions. While it captures signals from entire muscle groups, it is often susceptible to noise. It employs a three-electrode system with two electrodes for the EMG signal and one for a neutral reference, utilizing Common Mode Rejection (CMR). This technique cancels out common noise, such as power line interference, while amplifying the local electrical signals from the muscles, allowing for more accurate EMG readings. It operates at a sampling rate of 1 kHz with a maximum gain of 12. The hand dynamometer operated at 200 Hz, with a force range of 0 to 550 N, resolution of 0.05 N, and 95 % confidence interval uncertainty (1.96 standard deviations).

The reference dynamometer was calibrated in-house following the ASTM E74 standard (*Standard Practices for Calibration and Verification for Force-Measuring Instruments*) using weights conforming to OIML classes F1, M1, and M3. The laboratory environment was controlled at approximately 23 °C. Calibration forces were applied incrementally in the following sequence: 0, 5, 20, 50, 100, 150, 200, 250, 300, 350, 400, 450, 500 and 550 N, with preloading to account for hysteresis and three repetitions to ensure reliability. We conducted a complete unloading of the instrument between

²<https://shimmersensing.com/product/shimmer3-emg-unit/>

³<https://www.vernier.com/product/go-direct-hand-dynamometer/>

each successive loading cycle. For forces above 50 N, uncertainty was less than 4 %, while for forces below 50 N, uncertainty reached up to 10 %. The resulting calibration equation, mapping the raw dynamometer signal g_{raw} to the reported grip force g , is:

$$\hat{g} = 1.0629g_{\text{raw}} - 2.5880 \times 10^{-4}g_{\text{raw}}^2 - 9.0028 \times 10^{-8}g_{\text{raw}}^3 + 7.6152 \times 10^{-10}g_{\text{raw}}^4. \quad (2.1)$$

While the dominant term in (2.1) is linear and close to one, a fourth-degree polynomial was required to meet the strict specifications of the ASTM E74 standard. The integration of multiple devices and the acquisition of time-series data, including raw EMG signals and calibrated dynamometer measurements, were carried out using the Robot Operating System (ROS) and Python. This setup enabled seamless communication between hardware components, ensuring efficient data acquisition and synchronization across all experiments. The developed modules are publicly available in the GitHub repositories `tbazina/shimmer_ros` (Bazina, 2021b) and `tbazina/godirect_ros` (Bazina, 2021a).

Our goal is to predict grip force with high accuracy using a three-electrode system, where two electrodes are placed at a single sensing location, and a third neutral electrode serves as a reference. This setup addresses the challenge of the EMG signal’s low amplitude compared to environmental noise, such as interference from electrical sources. The system employs CMR, using the fact that environmental noise affects all electrodes in a similar manner. Shared noise is reduced by subtracting one signal from another, allowing the local EMG signal—affected by electrode placement—to be preserved and amplified. This method significantly enhances the signal quality, even in the presence of substantial background noise.

2.2.2 Design of Experiment

In the experimental design phase, a 2-factor randomized block design (RBD) (Heckert et al., 2012) was chosen as the most suitable approach. During the preliminary stage, several electrode attachment positions were evaluated. Following a basic screening experiment focused solely on signal strength, two forearm sensing locations near the flexor carpi ulnaris muscle (shown in Figure 2.1) were selected for further analysis. The electrode placement aligns with one of the configurations tested in prior studies (Barański and Kozupa, 2014; Wu et al., 2021). During the design process, the variability introduced by individual subjects was considered a nuisance, so the subject variable



Figure 2.1 Placement of sEMG electrodes near flexor carpi ulnaris muscle on the forearm: (a) Position 1 (P1) and (b) Position 2 (P2).

was treated as a nuisance factor. To isolate the impact of measuring positions on estimation and prediction errors, blocking was employed to control for the subject variable. Randomization was applied within each block to ensure unbiased results.

Before the experiments, participants' skin was prepared by removing hair near the measurement areas and cleaning the skin with alcohol swabs. Each participant was given several minutes to familiarize themselves with the setup and practice achieving five target force levels. For all experiments, the first 5 s of recorded data were used to zero the dynamometer signal in the measurement position. Transitions between grip force levels were recorded to capture dynamic changes and ensure a comprehensive analysis. The experiment, summarized in Table 2.1, involved 13 male participants aged 22 to 24. Recordings of grip force measurements and raw EMG signals from all experimental runs are available in Appendix A, providing a complete dataset for verification and further analysis across different subjects and sensing positions.

Table 2.1 Summary of 2-factor RBD experiment.

Subject Levels	Position levels	Grip force levels/%	Replications	Runs
ac, dp, ds, js, lb, lk, lm, ln, md, mm, nk, pb, ss	1, 2	100, 75, 50, 25, 0	2	52

2.3 Sensitivity Analysis and Procedural Parameter Optimization

The optimization process is designed to maximize the peak cross-correlation between the processed EMG signal and the synchronously recorded grip force. The process began with identifying the most influential spectral components, which act as the decision variables for optimization, through a multi-step SA. The subsequent step involved narrowing the ranges of these decision variables, centering them around their optimal values. This narrowing was achieved by examining scatterplot projections of each decision variable, generated using Latin hypercube (LH) sampling, along with smoothed trends and averages. By integrating optimization with SA, the method ensures that cross-correlation values remain close to their optimal levels, even when small variations are introduced. This approach enhances stability, avoids unstable maxima, and ensures consistent and reliable performance.

The EMG data is processed in batches of ~ 0.5 s (496 data points) at a sampling rate of 992.97 Hz. Each batch is converted to the frequency domain using FFT, with a frequency resolution of 2.002 Hz. A spectral mask, obtained through an optimization procedure, is then applied to selectively enhance or attenuate specific frequency components. After adjusting the amplitudes, an inverse FFT is applied to convert the signal back to the time domain. The signal is subsequently rectified by taking its absolute value, followed by smoothing with a windowed exponential moving average (MA). The smoothing window is applied within each batch, except for the initial (window size - 1) points, which are filled using data from the previous batch. In addition to optimizing the spectral mask, the optimization procedure also focuses on identifying the optimal window size and decay factor for the exponential MA. A flowchart outlining the full procedure for obtaining the optimized processed EMG signal is shown in Figure 2.2. To maximize the average peak cross-correlation across all measurements, a high-dimensional optimization problem was formulated. The optimization relied on a decision vector comprising 250 variables, each representing a parameter in the signal processing pipeline. The entries and initial bounds of the decision vector are defined as follows:

- A spectral mask consisting of 248 entries, each corresponding to a specific frequency bin from the FFT—excluding the DC offset—with values ranging 0–5.
- The window size for exponential smoothing is defined within 2 to 495.

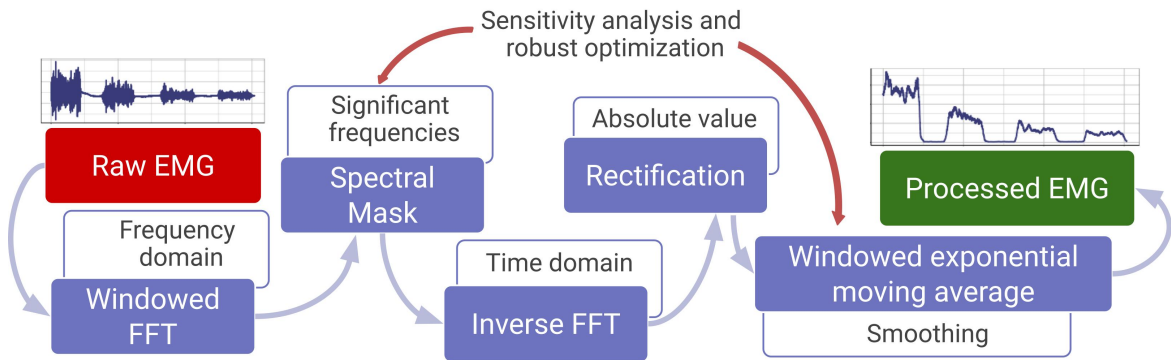


Figure 2.2 Signal processing steps for obtaining optimal processed EMG regarding cross-correlation with measured grip strength.

- The decay factor for exponential smoothing is constrained between 0 and 0.05.

The DC component, representing the zero-frequency spectral component, was set to zero. After applying the inverse FFT, this adjustment eliminates any constant offset in the time-domain signal, resulting in a processed EMG signal centered around zero and free of baseline shifts. Consequently, optimizing the DC component was unnecessary. The initial bounds for the spectral mask were set within the 0 to 5 range, allowing for either complete attenuation or up to five times amplification of each spectral component's amplitude. This enables selective enhancement or suppression of specific frequency components in the time-domain signal. Specifically, components with higher frequencies or those contributing noise can be attenuated, while components that maximize peak cross-correlation with grip force can be amplified, thereby improving the signal quality. Wide bounds for the smoothing window size were set to enable fine-tuned adjustments to the smoothing process. A smaller window size preserves sharp transitions but retains more noise, while a larger one reduces noise at the expense of important fluctuations. The optimal window size is determined through optimization, balancing noise reduction with preserving key EMG signal features. The decay factor bounds were selected to accommodate simple MA when set to 0 and exponential MA when set to a value greater than 0. Along with the smoothing window size, the decay factor determines the rate at which past values are diminished. A higher decay factor gives more weight to recent values, increasing the signal's responsiveness to changes. A lower decay factor preserves more influence from past values, leading to smoother transitions and reduced sensitivity to short-term fluctuations.

The objective function for optimization was formulated as the peak cross-correlation between the processed EMG signal and the measured grip force. As the problem is set

up for minimization, the function returns one minus the mean peak cross-correlation, resulting in values close to zero for high cross-correlations and values near one for low cross-correlations. Because of the differing sampling rates, with the EMG signal being sampled approximately five times faster than the dynamometer, the grip force signal was resampled according to the EMG timestamps. Intermediate values were estimated through linear regression to ensure proper alignment of the signals for cross-correlation calculation.

We hypothesize that not every FFT frequency bin—out of 248 total—substantially affects the cross-correlation. To validate the hypothesis, we perform simultaneous multi-step SA and optimization to narrow the problem scope, identify the most influential spectral components, and find their corresponding near-optimal mask modifiers.

2.3.1 Preliminary Sensitivity Analysis

The initial step involves conducting a preliminary SA using grouped spectral mask variables to obtain broader insights into how cross-correlation responds to smoothing and filtering. Variance-based SA using the grouped Sobol method (Saltelli et al., 2010; Sobol, 2001) was conducted independently for two dataset subsets, recorded on sensing positions P1 and P2 (refer to the Figure 2.1). We generated 65 536 (2^{16}) samples of the previously defined 250-dimensional decision vectors for each subset through Saltelli’s sampling method. To tackle uncertainty, we utilized bootstrapping with 65 536 resamples, forming additional datasets by resampling the original subsets with replacement. We calculated empirical distributions of the sensitivity indices (SIs), using the mean values as approximations for the SIs and the 95 % confidence intervals to assess uncertainty. Figure 2.3 illustrates the resulting first-order and total-order SIs, with narrow confidence intervals reflecting low levels of uncertainty. The SI quantifies how much a specific variable contributes to the mean peak cross-correlation variance, expressed as a percentage. First-order indices estimate the direct influence of an individual variable on the output, while total-order indices account for the variable’s complete contribution, factoring in interactions with other variables. Figure 2.3 shows that all three variables’ first-order and total-order indices are similar in value. This indicates that each decision variable primarily contributes independently to the output, with minimal influence from interactions with other variables. Furthermore, the summed value of all three first-order and total-order indices is ~ 1 , suggesting they can accurately assess the proportion of output variance attributed to each variable.

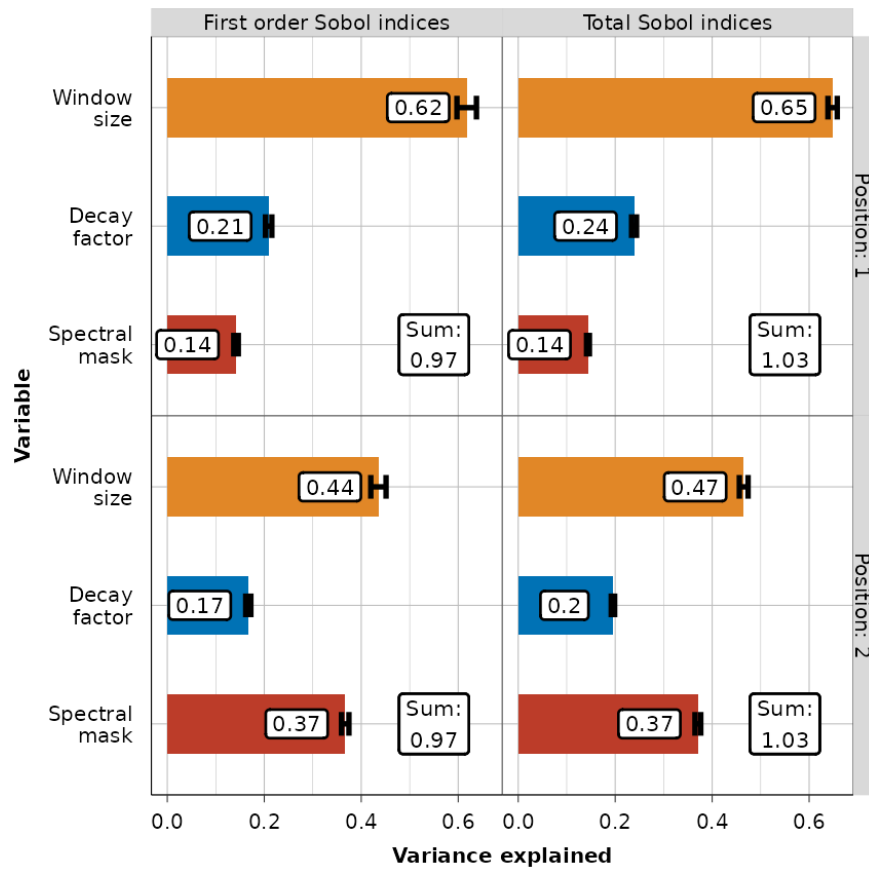


Figure 2.3 First-order and total-order sensitivity indices from preliminary grouped Sobol sensitivity analysis.

The preliminary SA found that the smoothing window size is the most influential factor, representing 44 to 62% of the variance in mean peak cross-correlation for both sensing locations. The rankings of contributions differ for the decay factor and the spectral mask, depending on the sensing position. The decay factor accounts for about 17 to 21% of the variation. In contrast, the impact of the spectral mask fluctuates more significantly—ranging from 14% at position P1 up to 37% at position P2.

An LH sampling of 10000 decision vector samples was performed within identical bounds to assess the partial contributions of the smoothing parameters. LH is a statistical sampling method (Iman et al., 1981) that generates samples to ensure uniform input space coverage. It divides each variable's range into equal intervals and randomly selects one value from each, yielding unique samples. It requires fewer samples than simple random sampling for similar coverage. Figure 2.4 shows the computed mean peak cross-correlation (using sampled decision vectors) projections

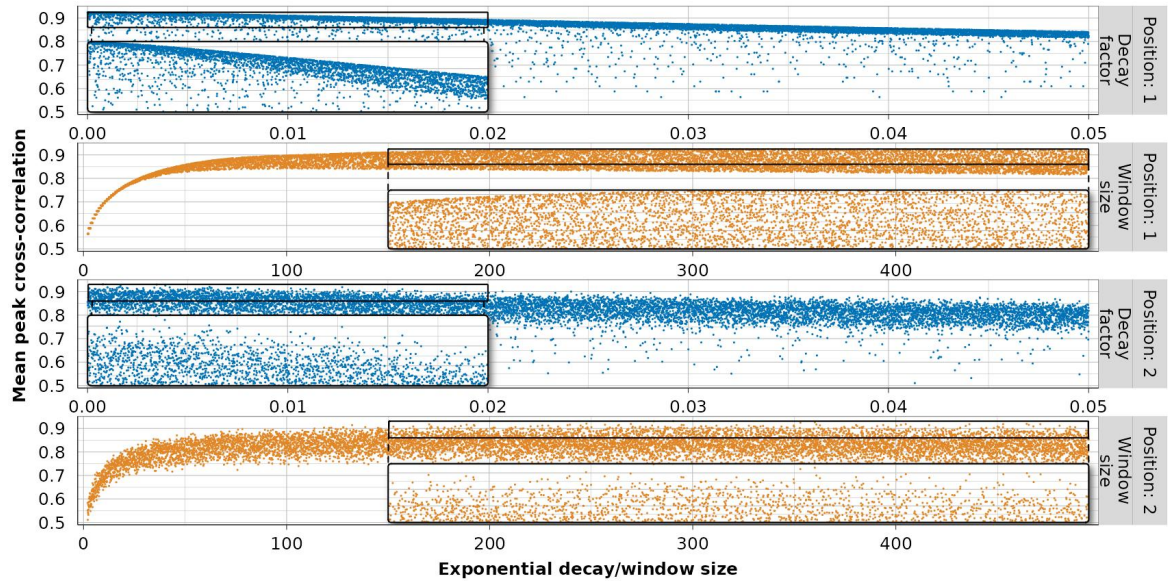


Figure 2.4 Projections of Latin hypercube sampling on smoothing decay factor and window size for both sensing positions: insights from preliminary sensitivity analysis.

onto the smoothing decay factor and window size decision variables. We can observe interesting dependency patterns from the visualized relationships. An increase in the window size causes the mean peak cross-correlation to rise until it levels off. This finding justifies limiting the window size to 200 to 495 for the upcoming SA steps. Conversely, a rise in the decay factor leads to a downward trend in the mean peak cross-correlation, which encourages us to restrict the range to 0 to 0.01.

Again, we conducted the grouped sensitivity analysis using these restricted parameter limits and discovered that the spectral mask explained 88 % of the variance in P1 and 95 % in P2. This highlights the significance of separating the mask for a more thorough investigation in the following steps.

2.3.2 Iterative Multi-Step Sensitivity Analysis and Optimization

The iterative multi-step ungrouped SA aims to streamline the optimization problem by decreasing the dimension of frequencies in the spectral mask and pinpointing those that strongly impact the mean peak cross-correlation variance. In this scenario, we employed an optimized Randomized Block Design Fourier Amplitude Sensitivity Test (RBD-FAST) SA method (Tarantola et al., 2006), which is more efficient than the Sobol

method. This method produces only first-order SIs using 65 536 decision vector samples, followed by a bootstrapping resampling process that involved 8192 (2^{13}) samples for the computation of 95 % confidence intervals.

After each phase, we visualized scatterplot projections onto the most sensitive spectral components or smoothing parameters using LH sampling with 10 000 samples to adjust the decision variable bounds for the next step manually. The initial phase indicated that the 2 Hz spectral component was the most sensitive factor influencing cross-correlation variance, with a SI ranging from 78 to 83 %. The LH sample scatterplot projection onto the 2 Hz component illustrated that increasing its mask multiplier resulted in a considerable decrease in the mean peak cross-correlation (see Figure 2.5). We restricted the 2 Hz multiplier bounds to 0 to 0.5. During the same SA and optimization step, we projected the scatterplot of LH sampling onto the three next highest-ranked variables (Figure 2.5) based on the sensitivity of the mean peak cross-correlation. This analysis revealed trends similar to those observed with the 2 Hz component, specifically a decreasing trend associated with the amplification of spectral components. We modified the limits to these specific ranges: 0 to 1 for 4 Hz, 0 to 2 for 6 Hz, and 0 to 3 for 50 Hz.

An additional 18 iterative steps, 2 to 19, of SA and optimization were performed comparably. Scatterplot projections of LH sampling that support the reasoning behind the obtained limits can be found in the author’s GitHub repository (Bazina, 2022a). The results from all stages of the iterative multi-step SA and optimization are presented in Figure 2.6. This figure highlights the most sensitive spectral components along with their refined limits. As the bounds for the more sensitive spectral components are tightened around the optimum from the previous step, neighboring spectral components become increasingly sensitive in the next step. Therefore, the iterative multi-step SA and optimization figure should be interpreted from left to right. A thorough step-by-step examination reveals a reverse funnel-like pattern (marked by the two red arrows). This pattern originates from low-frequency components and another point around 50 Hz, illustrating the shift from the most impactful spectral components to less significant ones.

Following the 19th step of the SA and optimization, the total contribution of all SIs associated with frequency mask at or above 204 Hz represented less than 2 % of the total variance related to mean peak cross-correlation. Consequently, the highest spectral component selected for further analysis is 202 Hz. This observation is consistent with

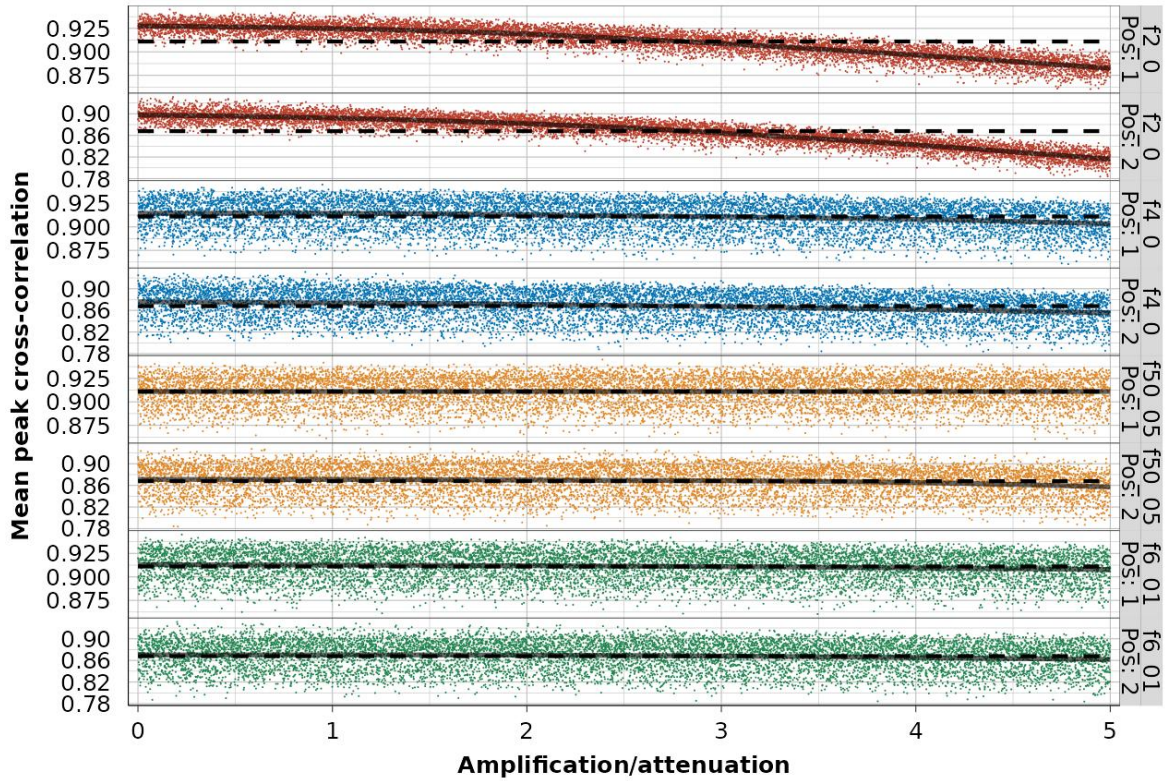


Figure 2.5 Projections of Latin hypercube sampling on spectral mask variables at 2, 4, 6 and 50 Hz for both sensing positions: first sensitivity analysis and optimization step.

Konrad (2006), which indicates that most of the power spectrum in sEMG is focused below 250 Hz.

We performed LH sampling within the newly established parameter ranges in the last steps (steps 20 and 21, as shown in Figure 2.6). We visually analyzed the trends in scatter plot projections for each of the 101 remaining spectral components (spanning from 2 to 202 Hz with a resolution of ~ 2 Hz) and fine-tuned the boundaries around the optimal point. The optimal smoothing parameters exhibited significant trends—an increase in the decay factor resulted in a reduction of peak cross-correlation. The ideal decay factor values were close to zero—between 0 to 5×10^{-4} —signaling a need for simple MA. We identified the optimal window size between 275 to 330.

Section 2.5 comprehensively describes the optimal spectral mask. With the optimal set of signal-processing techniques and parameters now established, the next section will describe the Koopman-driven methodology for estimating and predicting grip force based on the processed EMG signals.

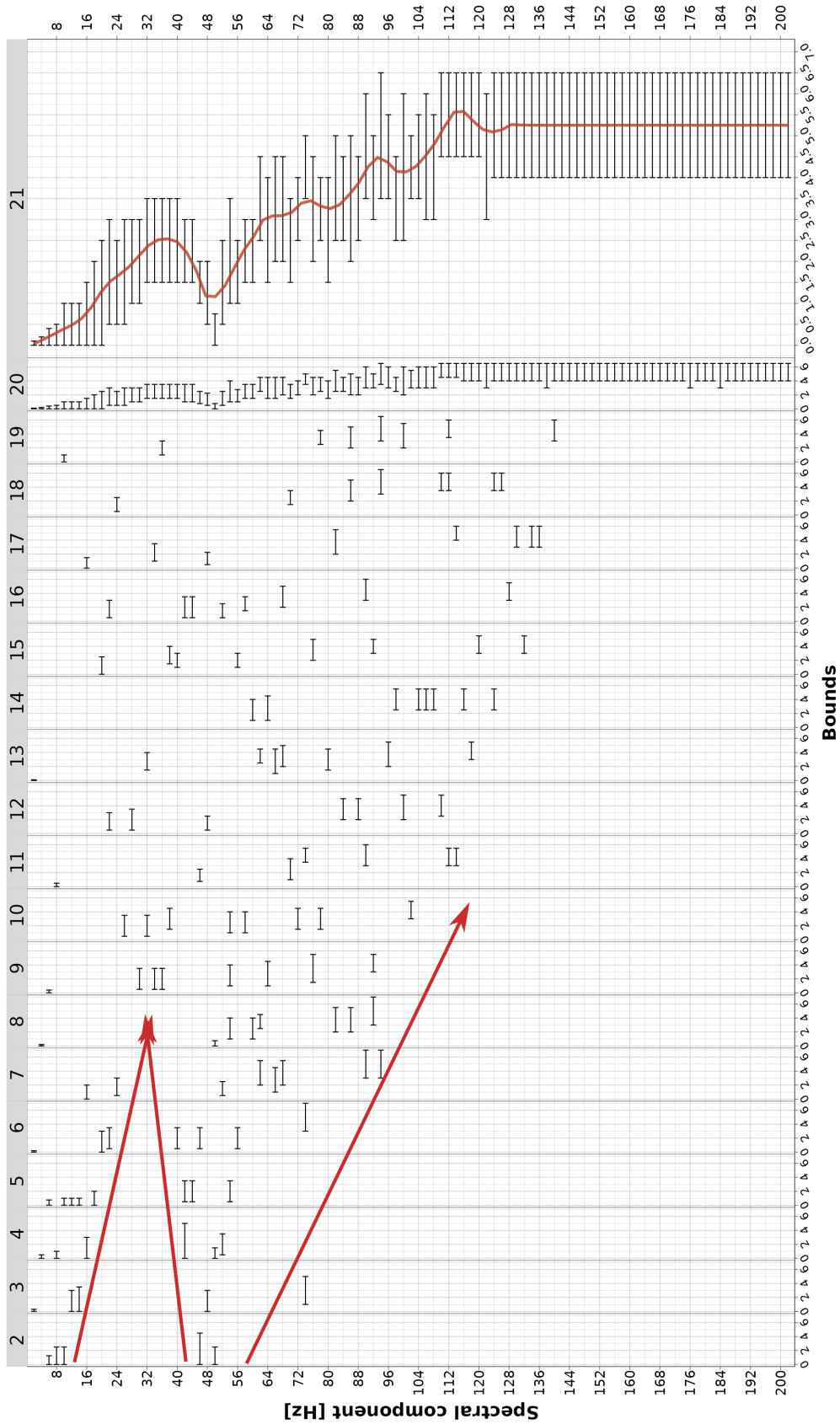


Figure 2.6 Iterative multi-step sensitivity analysis (steps 2-21) and simultaneous optimization by progressively narrowing the decision vector bounds and identifying the most influential frequency components. Initial bounds were set in the 0-5 range.

2.4 Real-Time Forecasting of Hand Grip Force

We divided this section into three parts. The initial part presents a concise overview of the KOT and its associated literature. The second and third parts explain its use in estimating and forecasting grip force.

The framework starts with the subject performing a single calibration experiment that lasts between 20 to 30 s. During this calibration, surface electromyography (sEMG) sensors and a dynamometer are employed, with grip force levels corresponding to those listed in Table 2.1. Once we finish the calibration, the sEMG signal is processed, and we develop a model for estimation using the complete calibration dataset. Following training, the estimation model is applied in batch processing to estimate grip force from the processed EMG data, using only the data available within the same time window. This estimated grip force is then fed to another model to forecast grip force over a 0.5 s interval—the subsequent batch.

2.4.1 Koopman Operator Theory Introduction

Koopman operator theory is a mathematical framework that captures the dynamics of nonlinear systems using an infinite-dimensional linear operator. This theory allows the analysis of complex nonlinear systems within a more manageable linear framework, maintaining the original dynamics of the system. By transforming the study of these systems, Koopman operator theory enables the use of tools like spectral analysis to better understand their behavior. Representing a dynamical system in state-space form involves defining an n -dimensional manifold of state space, denoted as M . The state vector \mathbf{x} is an element of M and is a set of variables that fully describe the system's condition at a specific time step. The evolution of the system in discrete time is expressed as follows:

$$\mathbf{x}_{i+1} = \mathbf{F}(\mathbf{x}_i), \quad (2.2)$$

Instances of state variables include processed EMG signals and grip force. In this context, \mathbf{F} represents a possibly nonlinear state transition function, $\mathbf{F} : M \rightarrow M$, while \mathbf{x}_{i+1} denotes the state at the next time step. Generally, modeling a system in state space requires accounting for the nonlinearities essential for accurately describing its dynamical behavior, which can often be complex or challenging. We adopt an operator-theoretic approach to observable dynamics to address this challenge, as Mezić (2005) described. As a result, the behavior of the nonlinear system represented in

equation (2.2) is mapped onto the dynamics of observables of \mathbf{x} , denoted as $\phi(\mathbf{x})$. Given the nature of the system, this study focuses on real-valued observables only, $\phi : M \rightarrow \mathbb{R}$. The set of all potential observables typically creates an infinite dimensional vector space. The Koopman operator \mathcal{K} , which characterizes how observables evolve over discrete periods Δt , is defined as Schmid (2022):

$$\phi(\mathbf{x}_{i+1}) = \mathcal{K}\phi(\mathbf{x}_i) = \phi[\mathbf{F}(\mathbf{x}_i)]. \quad (2.3)$$

The Koopman operator retains its linearity even when the underlying system is nonlinear. This characteristic holds regardless of the specific dynamics of the observables. However, a significant challenge within the Koopman framework is carefully selecting observables. Choosing the correct observables is crucial to ensure that the linearity of the operator effectively captures the system's dynamics.

2.4.2 Estimating Grip Force

The challenge of estimating grip force (g_i) from the processed EMG signal (e_i) is approached using a different KOT method. Unlike dynamical systems, the Koopman operator can also characterize “static“ nonlinear mappings between distinct spaces $M \rightarrow N$, as Mezić (2021) pointed out. By performing a lifting operation and selecting appropriate observables, we can represent nonlinear mappings through observable space using a linear mapping operator $\mathcal{K} : \mathcal{O}_M \rightarrow \mathcal{O}_N$.

To implement this theory for our specific problem, we lift the processed EMG signal (e_i) using the vector of functions ϕ and recorded grip force (g_i) using a different vector of functions ψ . As a result, the input E and output G matrices, which consist of N realizations of the lifted variables (e_i, g_i), can be expressed as:

$$E = [\phi(e_1), \dots, \phi(e_N)], \quad G = [\psi(g_1), \dots, \psi(g_N)]. \quad (2.4)$$

We obtained the estimate of the static Koopman operator $\bar{\mathcal{K}}$ by minimizing the residuals in the Frobenius norm, as detailed in Mezić (2021):

$$\min_{\mathcal{K}} \|G - \mathcal{K}E\|_F \quad \rightarrow \quad \bar{\mathcal{K}} = GE^\dagger. \quad (2.5)$$

In this context, the symbol \dagger denotes the Moore-Penrose pseudoinverse, which provides a solution in the least squares sense. Consequently, we can view the “static“ Koopman

operator as an estimation model that can be applied in the lifted space as follows:

$$G = \bar{\mathcal{K}}E. \quad (2.6)$$

Batch processing was required to enable real-time estimations. While we utilized the complete calibration dataset to approximate the Koopman operator for the final estimations, we processed each batch sequentially, applying the operator $\bar{\mathcal{K}}$ solely to the data within each batch window. Each batch window spans ~ 0.5 s (equaling 496 data points). The processed EMG data (see the Appendix A for figures from all experiments) was downsampled by a factor of eight before we estimated grip force, reducing the frequency from 993 to 124 Hz. This data was then normalized using min-max scaling to the 0 to 1 range.

Subsequently, we applied Hankel lifting using time-delay embedding, a specific instance of the previously generalized lifting in equation (2.4). We structured the Hankel data matrix E with the state \mathbf{e}_0 as the top row, followed by time-delay embeddings that include d time-delayed observables $\mathbf{e}_{\text{td}(1)}$ to $\mathbf{e}_{\text{td}(d)}$. We applied Hankel lifting to N univariate processed EMG time series data points as follows:

$$E = \begin{bmatrix} \mathbf{e}_0 \\ \mathbf{e}_{\text{td}(1)} \\ \vdots \\ \mathbf{e}_{\text{td}(d-1)} \\ \mathbf{e}_{\text{td}(d)} \end{bmatrix} = \begin{bmatrix} e_1 & e_2 & \cdots & e_{N-d} \\ e_2 & e_3 & \cdots & e_{N-d+1} \\ \vdots & \vdots & \ddots & \vdots \\ e_d & e_{d+1} & \cdots & e_{N-1} \\ e_{d+1} & e_{d+2} & \cdots & e_N \end{bmatrix}. \quad (2.7)$$

We developed a lifting process utilizing a time delay of $d = 60$ for both the downsampled processed EMG and grip data to obtain the observable matrices E and G , respectively. Additionally, we performed another nonlinear lifting of the EMG data to ensure proper mapping between the EMG and grip plateaus, which fits perfectly within the KOT framework. This process involves using gridded indicator observables, a type of observable function. In this approach, we partition the state space into a discrete grid, where each observable acts as an indicator function that activates (equals 1) when the system state resides within a specific grid cell. The concrete implementation includes partitioning a Cartesian plane using three selected time delays into irregular rectangular grid subregions (refer to Figure 2.8). We encoded each subregion as a distinct observable. For three chosen time-delayed data points—spaced τ_1 and τ_2 apart—we need to determine are the data points situated within a certain subregion,

denoted as S_{ijk} . We utilize an indicator function to assign a value of one to those points that fall within the specified subregion and a value of zero to those that do not. Let S_{ijk} represent a subregion within $[0, 1]^3$ defined by the grid bounds:

- For $\mathbf{e}_{\text{td}(n)}[1]$: lower limit b_i , upper limit b_{i+1} .
- For $\mathbf{e}_{\text{td}(n)}[1 + \tau_1]$: lower limit b_j , upper limit b_{j+1} .
- For $\mathbf{e}_{\text{td}(n)}[1 + \tau_2]$: lower limit b_k , upper limit b_{k+1} .

The indicator function is defined in the following manner:

$$\chi_{S_{ijk}}(\mathbf{e}_{\text{td}(n)}, \tau_1, \tau_2) = \begin{cases} 1, & \text{if } b_i \leq \mathbf{e}_{\text{td}(n)}[1] < b_{i+1} \\ & \text{and } b_j \leq \mathbf{e}_{\text{td}(n)}[1 + \tau_1] < b_{j+1} \\ & \text{and } b_k \leq \mathbf{e}_{\text{td}(n)}[1 + \tau_2] < b_{k+1}, \\ 0, & \text{otherwise.} \end{cases} \quad (2.8)$$

The gridded indicator observable $\mathbf{e}_{I, S_{ijk}, \tau_1, \tau_2}$ can be obtained by applying the formula in (2.8):

$$\mathbf{e}_{I, S_{ijk}, \tau_1, \tau_2}[n] = \chi_{S_{ijk}}(\mathbf{e}_{\text{td}(n)}, \tau_1, \tau_2), \quad \text{for } n = 1, \dots, N - d. \quad (2.9)$$

Using this lifting approach can produce a significant number of empty observables filled with zeros and sparse observables that mainly consist of zeros. This situation may result in overfitting within the estimation model. The sparsity of these observables can lead to instability in estimating the Koopman operator since many offer limited valuable insights into the actual dynamics of the system. When many observables are predominantly zeros, their few nonzero values may cause the model to memorize the training data rather than generalize to new, unseen states. We implemented a sparsity constraint to address these issues to ensure we only retained observables with a minimum density of 0.1% during the algorithm testing phase. The effect of sparsity constraint on overfitting was examined visually and can be clearly seen during estimating grip force in Figure 2.7. In the left side subfigure 2.7a, sparsity constraint was not employed, and the model “chose” extremely sparse observables. When fitted to the entire data (top plot in the figure), it performed well, but when fitted only to a subset of the data, divided by blue dashed lines (bottom plot), generalization was unstable. On the other hand, sparsity constraint was employed in the right side subfigure 2.7b. No overfitting occurred when we fitted the model to the entire data or its subset, and the model generalized stable to the previously unseen data.

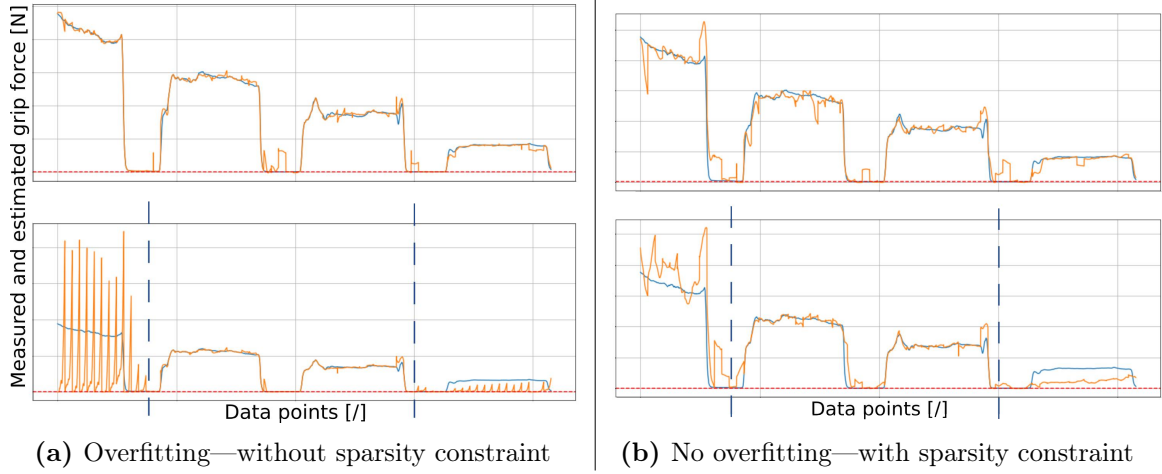


Figure 2.7 The effect of sparsity constraints during modeling using gridded indicator observables.

Through heuristic evaluation, we discovered that a grid (b) with 22 uneven subregions and a power function with an exponent of 1.8 for adjusting spacing in each dimension produced the best results (refer to Figure 2.8). This grid resolution helped reduce the risk of overfitting by avoiding an overly fine grid and the increased computational burden of including too many gridded indicator observables. We identified the exponent for the grid spacing by analyzing plateaus at 100, 75, 50, 25 and 0% in both the processed EMG signals and the measured grip force. The gridding was applied simultaneously to the 1st, 30th, and 60th time delay, with values of $\tau_1 = 29$ and $\tau_2 = 59$. This resulted in gridded identity observables represented as $\mathbf{e}_{I, S_{ijk}, 29, 59}$. The maximum possible number of gridded indicator observables, considering all grid subregions S_{ijk} and the three time delays, is $22^3 = 10648$. However, we excluded most of these due to their high sparsity, as shown in Figure 2.8.

To compute the static Koopman operator estimation model, we constructed the final processed EMG data matrix E by vertically stacking row vectors of time-delayed observables alongside row vectors of gridded indicator observables. For the grip force

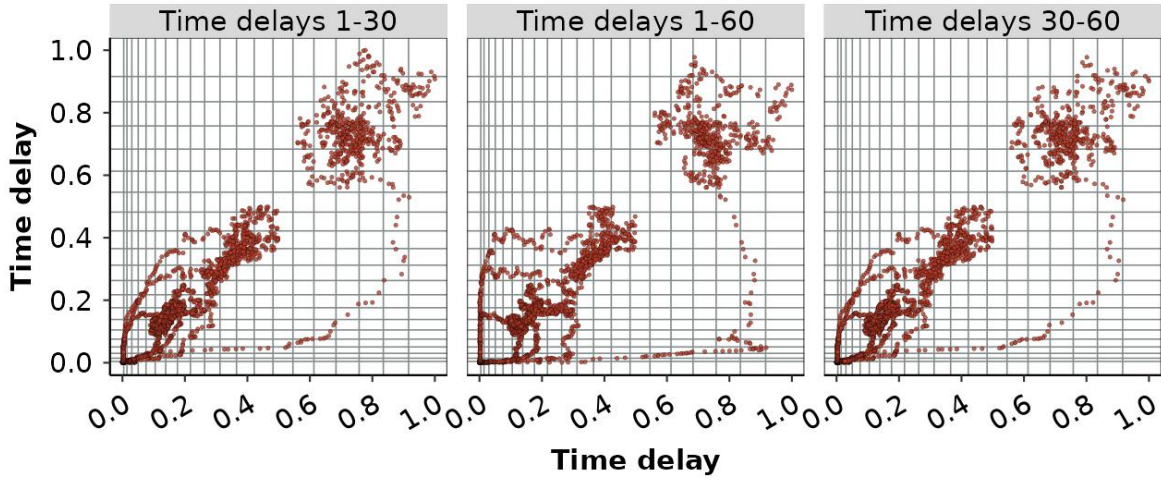


Figure 2.8 Three-dimensional representation of gridded indicator observables $\mathbf{e}_{I,S_{ijk},29,59}$, showcasing optimal grid divisions.

data matrix G , we stacked row vectors of time-delayed observables with rows of zeros:

$$E = \begin{bmatrix} \mathbf{e}_0 \\ \mathbf{e}_{td(1)} \\ \vdots \\ \mathbf{e}_{td(60)} \\ \vdots \\ \mathbf{e}_{I,S_{ijk},29,59} \\ \vdots \end{bmatrix}, \quad G = \begin{bmatrix} \mathbf{g}_0 \\ \mathbf{g}_{td(1)} \\ \vdots \\ \mathbf{g}_{td(60)} \\ \vdots \\ \mathbf{0} \\ \vdots \end{bmatrix}. \quad (2.10)$$

We trained the estimation model using the equation (2.5) on all the calibration data, completing this process in under 1.5 seconds. The model approximations of grip force were limited to a minimum value of -1.

2.4.3 Forecasting Grip Force

We have developed a methodology to make short-term predictions of grip force within a 0.5-second timeframe. This method builds on previously established grip estimates and utilizes the Koopman operator for modeling dynamic systems. The Koopman operator is particularly suitable for this task because it adapts to dynamically changing environments (Mezić, 2021), such as those encountered during object grasping. We aim to identify the Koopman operator for the dynamical system that describes the

evolution of observables in the same space, as outlined in equation (2.2), and to utilize it for forecasting. This approach allows for short training durations on batches of data, enabling adjustments based on the most recent state of the system. Given that the Koopman operator can be infinite-dimensional, we employ the Dynamic Mode Decomposition (DMD) technique to estimate its spectral properties numerically in a finite number of dimensions. These properties are represented in Ritz pairs, consisting of λ_j (Ritz values) and z_j (Ritz vectors):

$$\begin{aligned} Z &= \begin{bmatrix} \mathbf{z}_1 & \mathbf{z}_2 & \dots & \mathbf{z}_r \end{bmatrix}, \\ \mathcal{K}Z = Z\Lambda, \quad \text{where} \quad \Lambda &= \begin{bmatrix} \lambda_1 & 0 & \dots & 0 \\ 0 & \lambda_2 & \dots & 0 \\ \vdots & \vdots & \ddots & \vdots \\ 0 & 0 & \dots & \lambda_r \end{bmatrix}, \\ \mathcal{K}\mathbf{z}_j &= \lambda_j\mathbf{z}_j, \quad j = 1, \dots, r. \end{aligned} \tag{2.11}$$

In this context, r denotes the number of Koopman modes identified after applying DMD. DMD provides a finite-dimensional representation of the Koopman operator by utilizing a set of data snapshots in time. Since DMD relies on a limited collection of these snapshots, the calculated eigenvalues and eigenvectors serve as approximations—known as Ritz values and Ritz vectors—of the actual spectral characteristics of the Koopman operator. These approximations occur due to the finite-rank nature of data-driven decomposition techniques like DMD. The accuracy of these Ritz pairs is influenced by factors such as the dataset’s richness and the observables’ selection.

An eigenvalue λ_j is a scalar that indicates how much the corresponding eigenvector is stretched or compressed during a linear transformation. Eigenvalues can be real or complex numbers and describe the properties of the Koopman operator, representing a dynamic system model. The eigenvalues of the Koopman operator are linked to the stability properties of observable evolution over time. The absolute value of an eigenvalue $|\lambda_j|$ signifies the rate of growth or decay:

- If $|\lambda_j| > 1$: exponential growth,
- If $|\lambda_j| < 1$: exponential decay,
- If $|\lambda_j| = 1$: oscillatory behavior or constancy.

An eigenvector \mathbf{z}_j is a non-zero complex vector scaled by a constant factor when applied linear transformation. Eigenvectors are essential for understanding the direction

of this transformation, as they represent the modes or patterns of a system’s behavior within observable space. Practically, an eigenvector characterizes an observable’s “shape” or form as it evolves. The eigenvectors of the Koopman operator illustrate the spatial distribution of Koopman modes, providing insights into underlying spatial patterns. For a detailed explanation of DMD, refer to Schmid (2022).

To extract the spectral characteristics of the Koopman operator from the data matrix, we utilized pyKMD suite⁴. We implemented the Hankel-DMD embedding method introduced by Arbabi and Mezić (2017), along with the Refined Rayleigh-Ritz Data-Driven Modal Decomposition (DDMD-RRR) technique and QR compression methods, as described by Drmač et al. (2018). The DDMD-RRR technique refines Ritz vectors and improves their accuracy by minimizing residuals, while QR compression enables the efficient execution of algorithms in real time.

The time-delay embedding of the estimated grip force, as shown in equation (2.7) for processed EMG, proved highly effective. The time-delayed model maintained linearity while successfully capturing the non-linearities in grip force prediction. We kept the number of time delays d between 4 to 10 for fine-tuning model.

Before starting the data preparation for forecasting, we applied *Locally Weighted Scatterplot Smoothing* (LOWESS), as outlined by Cleveland (1979), to smooth the grip force estimates. This helped reduce spikes and minimize prediction errors. We set the window size, which we later referred to as the smoothing coefficient, between 1.1 to 1.9 times the batch size for model fine-tuning. Both the currently processed batch and the previous batches were utilized in this smoothing process.

We conducted a heuristic evaluation and created a matrix of first-order interactions based on the natural logarithm transformations of the Hankel-lifted observables to further reduce prediction error. To ensure that all entries remained positive for the logarithmic transformation, we added 10 to each entry. The interaction component $G_{e,int}$ of the input data matrix for forecasting grip force from estimates is as follows:

$$G_{e,int} = \begin{bmatrix} \ln g_{e1} \ln g_{e2} & \ln g_{e2} \ln g_{e3} & \cdots & \ln g_{e(N-d)} \ln g_{e(N-d+1)} \\ \ln g_{e1} \ln g_{e3} & \ln g_{e2} \ln g_{e4} & \cdots & \ln g_{e(N-d)} \ln g_{e(N-d+2)} \\ \vdots & \vdots & \ddots & \vdots \\ \ln g_{e(d-1)} \ln g_{e(d+1)} & \ln g_{ed} \ln g_{e(d+2)} & \cdots & \ln g_{e(N-2)} \ln g_{eN} \\ \ln g_{ed} \ln g_{e(d+1)} & \ln g_{e(d+1)} \ln g_{e(d+2)} & \cdots & \ln g_{e(N-1)} \ln g_{eN} \end{bmatrix}. \quad (2.12)$$

⁴<https://apps.aimdyn.com/>

We constructed the final lifted input data matrix by stacking (2.12) with the time-delay embedding of the estimated grip data. The resulting matrix, $G_{e,\text{lift}}$, can be seen as a sequence of snapshots, denoted as $\mathbf{g}_{e,\text{lift}(i)}$, which include both interaction terms and time delays.

$$G_{e,\text{lift}} = \begin{bmatrix} G_{e,\text{int}} \\ G_{e,\text{td}} \end{bmatrix} = \begin{bmatrix} \mathbf{g}_{e,\text{lift}(1)} & \cdots & \mathbf{g}_{e,\text{lift}(N-d)} \end{bmatrix}. \quad (2.13)$$

We further thin the data matrix (2.13) before inputting it into the DMD by removing certain snapshots through a specific thinning step. Thinning, as presented in Frame and Towne (2023), eases the computational burden during forecasting and helps to prevent unnecessary predictions of high-frequency noise within the data. By applying a thinning step within a range of 3 to 8, we can achieve forecasts with frequencies ranging from 16 to 41 Hz, which is adequate for analyzing gripping dynamics.

After obtaining the spectral decomposition of the Koopman operator \mathcal{K} , we compute the Koopman amplitudes α_j to reconstruct the input data matrix or predict the next state. This can be formulated as a least squares minimization problem:

$$\min_{\alpha_j} \sum_{i=1}^{N-d} \left\| \mathbf{g}_{e,\text{lift}(i)} - \sum_{j=1}^{\ell} \mathbf{z}_j \alpha_j \lambda_j^{i-1} \right\|_2^2. \quad (2.14)$$

Here, ℓ represents the number of retained Koopman modes after dimensionality reduction from r . We implemented the structured least squares solver from Drmač et al. (2020) within the pyKMD framework. This solver automatically selects the appropriate method based on the *scaled condition number* of the problem:

- Well-conditioned systems—solved using normal equations,
- Ill-conditioned systems—solved using QR factorization-based methods.

To ensure physically meaningful predictions, excessively high or low estimates are thresholded within the minimum and maximum grip force values from the calibration experiment. Future snapshots can be predicted over a time horizon τ as:

$$\mathbf{g}_{e,\text{lift}(N-d+\tau)} \approx \sum_{j=1}^{\ell} \mathbf{z}_j \alpha_j \lambda_j^{N-d+\tau-1}, \quad \tau = 1, 2, \dots \quad (2.15)$$

For estimating and forecasting grip force, we selected the *Weighted Mean Absolute Percentage Error* (wMAPE) as the error metric. This relative metric effectively handles

near-zero values by scaling absolute errors against the total absolute sum of actual values. This property makes wMAPE particularly suitable for comparing measurements across both high and low grip magnitudes. wMAPE is computed as:

$$\text{wMAPE} = \frac{\sum_{i=1}^N |\hat{g}_i - g_i|}{\sum_{i=1}^N |g_i|}, \quad (2.16)$$

where \hat{g}_i represents the estimated or predicted grip force, while g_i refers to the actual measured grip force.

The final hyperparameter tuning for the prediction model was conducted using a grid search involving five parameters: the number of Koopman modes after reduction ℓ , the number of time delays d , the smoothing window modifier coefficient, the thinning step, and the forecasting window modifier coefficient. Figure 2.9 shows the final hyperparameter tuning results, excluding the runs with extremely high errors. We can achieve the minimum wMAPE with four Koopman modes, between 7 to 10 time delays, a smoothing window modifier coefficient ranging from 1.1 to 1.2, a thinning step between 7 to 8, and a forecasting window modifier coefficient between 1.2 to 1.4. To improve robustness, we calculated both the mean and median wMAPE for all measurements. The hyperparameters that resulted in the lowest sum of the mean and median wMAPE were identified as the optimal hyperparameters for the prediction algorithm. Optimal hyperparameters are detailed in Table 2.2, and the final error metric, calculated using these parameters, is presented in Table 2.6.

Table 2.2 Optimal hyperparameters for the grip force forecasting model, obtained after tuning the algorithm.

Forecasting window modifier coefficient	Smoothing window modifier coefficient	Thinning step	No. time delays	No. Koopman modes
1.3	1.1	7	8	4

2.5 Results and Experimental Validation

As illustrated in Figure 2.6, the funnel-shaped structure of the iterative multi-step SA highlights the most sensitive frequency ranges. It is essential to first address the lower frequency spectral components, specifically those at or below 14 Hz and those

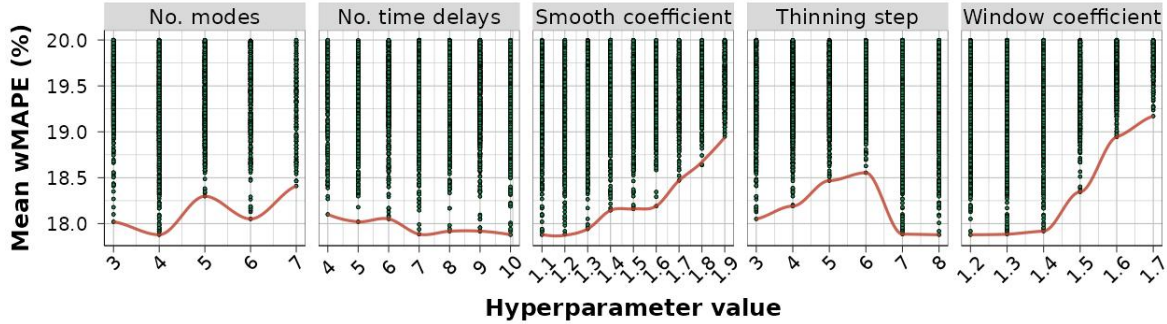


Figure 2.9 Hyperparameter tuning of Koopman prediction algorithm. The wMAPE represents the average of all forecasts across 52 experiments. A smooth red line connects the values of runs with the minimum mean wMAPE.

within the 46 to 50 Hz range. By doing this, we can significantly increase the peak cross-correlations between the processed EMG signal and the measured grip strength. Once we optimize these spectral components, the range of sensitive frequencies expands, gradually bridging the gap between 14 Hz and 46 Hz and extending into higher frequency components of up to 202 Hz.

We typically perform additional parameter optimization after determining the final decision vector bounds. We first gathered summary statistics on the mean peak cross-correlations from LH sampling within these decision vector bounds, as shown in Table 2.3. The minimal variability in standard deviation and the small range between the lowest and highest mean peak cross-correlations indicate no need for further optimization of these near-optimal values. The mean values between each decision variable’s upper and lower bounds will be used as the optimal spectral mask values, illustrated in Figure 2.10. The figure clearly shows five distinct mask sections of the mask.

Table 2.3 Summary statistics of mean peak cross-correlations between processed EMG and grip force signals obtained from LH sampling after the final SA step.

Position	Mean	SD	Min.	Max.
P1	0.956	413×10^{-6}	0.954	0.958
P2	0.960	535×10^{-6}	0.958	0.962

The first section of the mask corresponds with findings in the literature (Konrad, 2006), which relate to the attenuation or removal of lower-frequency components associated with wire movements. The attenuation follows a nearly linear trend: the

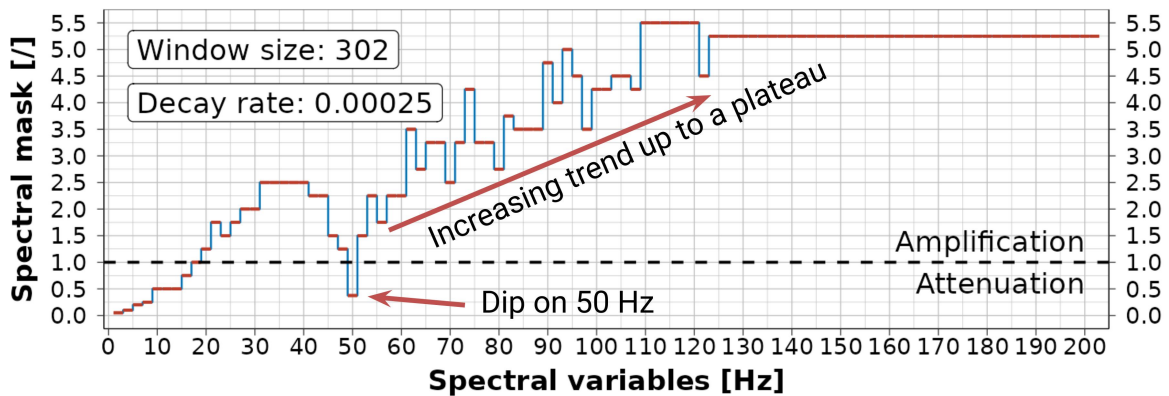


Figure 2.10 Optimized spectral mask for processing EMG signals at positions P1 and P2, showing frequency-specific amplitude modifications that maximize correlation between processed EMG and grip force.

DC component and 2 Hz frequencies are completely filtered out, 10 Hz frequencies are reduced by 50 %, and 18 Hz frequencies remain unaltered.

For frequencies between 20 Hz and 48 Hz in the second part of the mask, the amplification follows an inverted U-shaped curve, starting and ending at 25 %, with a peak amplification of 150 % occurring between 32 to 42 Hz.

In the third part of the mask, we observe how electrical ground noise affects the recorded signal, causing the inverted U-shaped curve to transition into a sharp drop at the 50 Hz component. Processing the 50 Hz spectral component poses a significant challenge: retaining it at nominal amplitudes fails to produce adequate results while eliminating it with a notch filter is equally ineffective. Our analysis demonstrates that maintaining the 50 Hz component at 37.5 % of its amplitude optimally preserves signal power for grip force modeling. This result aligns with the findings of Konrad (2006), which show that the 50 Hz frequency bin contains a substantial portion of the power spectrum that should not be discarded.

The fourth section of the mask targets the mid-frequency range, specifically between 52 Hz and 110 Hz, where the majority of the signal’s power is concentrated. As the amplitudes of the spectral components decline, the mask applies a linear amplification strategy, gradually increasing from 50 % at 52 Hz to 450 % at 110 Hz. This need for mid-frequency amplification can be explained by three physiological mechanisms associated with the spatial low-pass filtering of EMG signals—MU structure, volume conduction, and electrode placement (Stegeman et al., 2000):

- The structure of MUs introduces spatial smoothing at the signal source due to the dispersed arrangement of muscle fibers within a single motor unit.
- Volume conduction causes attenuation and distortion of the signal as it propagates through biological tissues from the source to the skin surface, where it is recorded.
- Electrode positioning contributes to low-pass filtering, as the electrodes average the signal over the sensing area, reducing higher-frequency components.

In the final part of our mask, we observe that the amplification trend stabilizes at approximately 425 to 450 % near 110 Hz, extending up to 202 Hz. We performed a stepwise ablation analysis on the spectral mask plateau to validate these findings. Starting from the full range of 110 to 202 Hz, we systematically disabled frequency bands in 4 Hz increments, progressively narrowing the range down to 198 to 202 Hz. At each step, the mean peak cross-correlation decreased, confirming the role of the mask plateau in achieving our results.

We further performed a follow-up investigation on a previous conclusion that the higher-frequency components in the range of 204 to 498 Hz had a negligible impact. We conducted an ablation study by varying the mask values from 0 to 5 across this frequency range. Since no notable changes in the mean peak cross-correlation were observed, we set the mask to 0 for frequencies between 204 Hz and 498 Hz. Discarding frequency components in this band protects the system from potential noise. This novel method for processing sEMG signals using a spectral mask offers unique insights that deserve further exploration.

The optimal smoothing window size was 302. Combined with a decay factor of 0.25×10^{-3} , this indicates a simple MA smoothing technique. By applying the optimal spectral mask and smoothing methods, as depicted in Figure 2.2, the processed EMG signals (shown in red in Figure 2.11b) exhibit a strong cross-correlation with the measured grip force. For processed sEMG data across all measurements, see Appendix A.

Table 2.4 summarizes the peak cross-correlations and time lags obtained from within measurements at both sensing positions after optimal signal processing. This summary includes cross-correlations from all 52 measurements obtained using optimal processing parameters. The results show a strong correlation between processed EMG signals and grip force measured at both sensing positions, P1 and P2. Furthermore, the lag analysis indicates that the peak cross-correlations occur when the EMG signals lag

behind the grip force measurements by intervals ranging from 0 to 156 ms, with higher lags observed in P1.

Table 2.4 Summary statistics of peak cross-correlations and time lags between optimal processed EMG signals and grip force measurements at sensing positions P1 and P2.

	Min.	1st Qu.	Median	Mean	3rd Qu.	Max.
Position P1						
Peak cross-correlation	0.891	0.947	0.964	0.958	0.971	0.987
Peak time lag [ms]	0.0	0.0	43.8	54.0	96.4	156.1
Position P2						
Peak cross-correlation	0.924	0.952	0.967	0.962	0.972	0.988
Peak time lag [ms]	0.0	0.0	16.1	25.0	42.8	78.5

The RBD experiment design employed in this study, as detailed in Subsection 2.2.2, allows for the analysis of subject and sensing position effects on both estimation and forecasting wMAPE. Using the methodology described in Section 2.4.2, the wMAPE estimation error was computed for all 52 experimental runs, with results summarized in Table 2.5. The overall mean estimation wMAPE from all 52 runs is approximately 5.5%, highlighting the effectiveness of this approach in accurately estimating grip force using a single sensing position. Beyond error metrics for all 52 experimental runs, we calculated means and effects across blocks grouped by subject or sensing position. The effects were determined by calculating the difference between each block’s mean and the overall mean estimation wMAPE. While the means and effects varied substantially across subjects, ranging from -1.8 to 2.2% , the effect of sensing position P1 on wMAPE was only 0.2% . In contrast, the effect of position P2 was -0.2% .

We employed an analogous methodology and procedure described in Subsection 2.4.3 to generate short-term grip force forecasts in 0.5s batches with a 0.5s forecasting horizon. Using the optimal hyperparameters from Table 2.2, we computed the wMAPE for all 52 measurement runs, with results presented in RBD format in Table 2.6. The overall mean wMAPE for forecasting was approximately 17.9% . While the subject effect on wMAPE varied significantly, ranging from -4.0 to 2.9% , the position effect remained consistently narrow, within a range of $\pm 0.1\%$.

To assess whether sensor positioning significantly impacts estimation or forecasting wMAPE, we performed an analysis of variance (ANOVA) on the blocked data from Tables 2.6 and 2.5, using a significance level of 5% .

Table 2.5 wMAPE for estimating grip force from EMG across all subjects, two sensing positions (P1 and P2), and two replications (R1 and R2), with means and effects calculated per subject and position.

	Subject												Position		
	ac	dp	ds	js	lb	lk	lm	ln	md	mm	nk	pb	ss	Mean	Effect
Position P1															
R1	4.4	6.4	10.0	4.5	7.7	6.6	4.5	8.4	4.3	5.1	2.7	6.1	3.8		
R2	2.3	4.7	5.4	3.9	8.0	6.9	7.6	3.7	5.2	6.8	6.4	7.9	4.3	5.7	0.2
Position P2															
R1	4.0	4.1	4.7	3.9	3.3	5.8	3.6	4.4	7.2	8.5	3.3	6.7	4.4		
R2	3.8	4.3	4.4	5.1	4.9	6.2	4.4	4.6	9.2	9.9	3.2	10.1	3.3	5.3	-0.2
Subject mean and effect															
Mean	3.6	4.9	6.1	4.4	6.0	6.4	5.1	5.3	6.5	7.6	3.9	7.7	4.0		
Effect	-1.8	-0.6	0.6	-1.1	0.5	0.9	-0.4	-0.2	1.0	2.1	-1.6	2.2	-1.5		
Overall mean estimation wMAPE: 5.48%															

Table 2.6 wMAPE for forecasting grip force from EMG across all subjects, two sensing positions (P1 and P2), and two replications (R1 and R2), with means and effects calculated per subject and position.

	Subject												Position		
	ac	dp	ds	js	lb	lk	lm	ln	md	mm	nk	pb	ss	Mean	Effect
Position P1															
R1	24.7	15.0	25.0	18.7	21.4	21.1	13.1	22.7	12.5	15.4	19.4	18.8	13.4		
R2	23.6	15.4	17.9	17.6	15.0	18.9	17.5	15.1	22.3	14.7	18.6	19.6	10.6	18.0	0.1
Position P2															
R1	14.8	17.2	16.7	17.7	16.1	20.4	12.9	18.5	15.8	17.2	19.1	20.2	15.2		
R2	16.8	16.1	17.6	22.3	14.2	22.9	12.3	17.2	20.9	25.2	19.0	20.5	16.7	17.8	-0.1
Subject mean and effect															
Mean	20.0	15.9	19.3	19.1	16.7	20.9	13.9	18.4	17.9	18.2	19.0	19.8	14.0		
Effect	2.1	-2.0	1.4	1.2	-1.3	2.9	-4.0	0.4	-0.0	0.2	1.1	1.8	-4.0		
Overall forecasting mean wMAPE: 17.92%															

The results, summarized in Table 2.7, show that while the subject effect on estimation wMAPE was statistically significant with a p -value of 0.015, the positional effect—after accounting for subject variability—was not significant with a p -value of 0.422.

Table 2.7 Results of ANOVA conducted on the blocked RBD with estimation and forecasting wMAPE, assessing the subject and position effects at a 5% significance level.

	Estimation					Forecasting				
	Df	Sum Sq	Mean Sq	F value	Pr(>F)	Df	Sum Sq	Mean Sq	F value	Pr(>F)
Position	1	1.91	1.91	0.66	0.422	1	0.35	0.35	0.03	0.853
Subject	12	87.51	7.29	2.52	0.015	12	232.00	19.33	1.94	0.060
Resids	38	110.15	2.90			38	378.55	9.96		

Similarly, for forecasting, the positional effect on forecast wMAPE was non-significant with a p -value of 0.853. The subject effect in forecasting also approached non-significance, with a p -value of 0.06.

These findings indicate that the placement of EMG electrodes on the flexor carpi ulnaris muscle—whether at position P1 or P2—does not significantly affect estimation or forecasting errors. This demonstrates the robustness of the method to variations in electrode placement.

A systematic comparison of the methodology’s impact on signal examples is illustrated in Figure 2.11. This figure contrasts all described sEMG and grip signals, ranging from raw and processed EMG to estimated and measured grip force, culminating in smoothed estimates and short-term batch predictions.

The top panel, Figure 2.11a, displays the raw sEMG signals for three subjects, highlighted in red. The middle panel, Figure 2.11b, presents three representative examples of estimated grip force, with errors corresponding approximately to the first, second, and third quartiles, marked in yellow. This panel also includes the optimally processed sEMG signal (red) and the measured grip force (blue).

The bottom panel, Figure 2.11c, showcases forecast examples with error metric values approximately corresponding to the first, second, and third quartiles, indicated by red dots. The smoothed grip force estimation, which serves as the input for forecasting, is depicted as a yellow line. Complete graphs for all experimental runs are available in the author’s GitHub repository (Bazina, 2022a).

This research developed real-time procedures for sensing hand muscle activity using non-invasive sEMG sensors and estimating exerted grip force with a calibrated dynamometer. By optimizing signal processing steps, we achieved a high cross-correlation coefficient (~ 0.96) between muscle activity and grip force. A Koopman-based methodology enabled accurate force estimation (5.5% wMAPE error) and short-term prediction

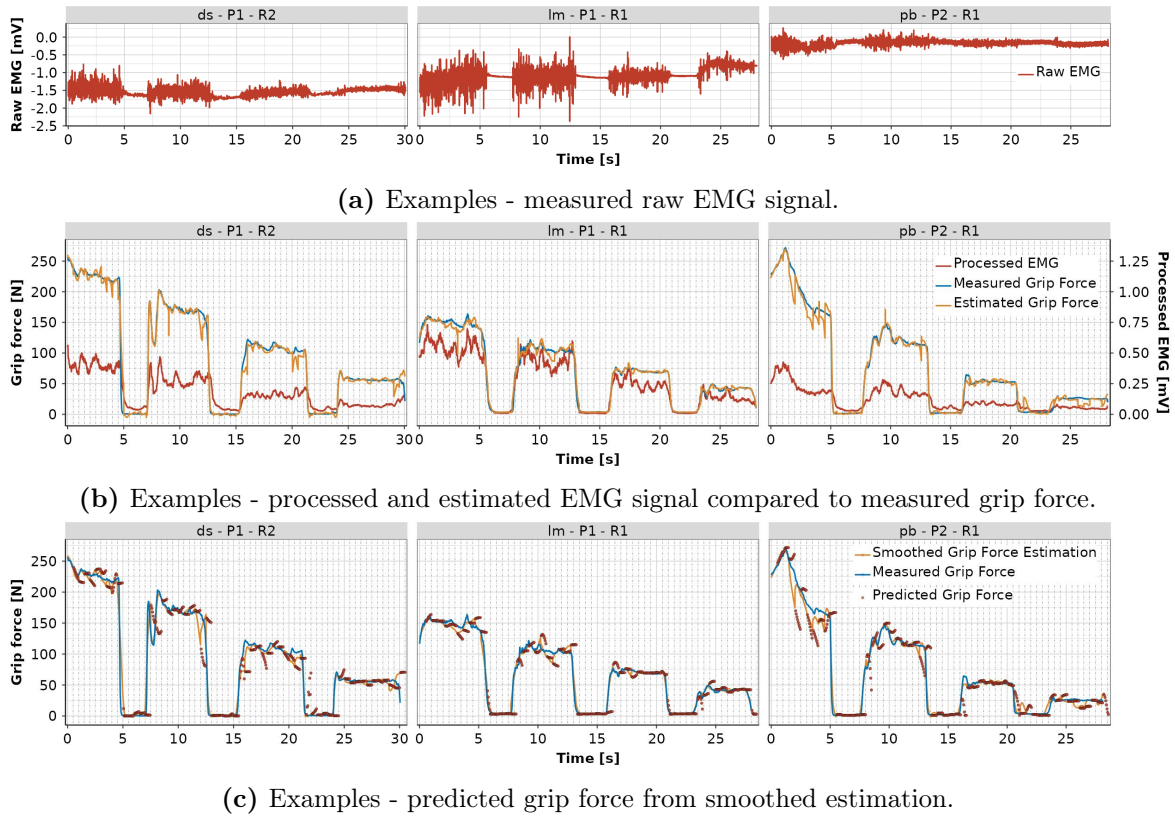


Figure 2.11 Examples of all signals relevant for grip force modeling - raw and processed EMG signals, estimates, smoothed estimates, forecasts, and measured grip force.

(17.9% wMAPE error), demonstrating robust performance across two sensing locations. The framework proved ready for real-time implementation, requiring minimal calibration time (<30 s) and low-latency prediction generation (<30 ms). This work lays the foundation for developing force-adaptive rehabilitation devices based on EMG sensing.

The next chapter focuses on the development of simplified and interpretable models for human hand movements, with an emphasis on grasp-oriented intra-finger dependencies. Leveraging one of the largest publicly available multimodal databases for hand and wrist movements, this research simplifies kinematic modeling for prosthetic and rehabilitation device design.

Chapter 3

Grasp-oriented reduction of hand kinematics in robotic rehabilitation

THIS chapter presents a novel approach to simplifying hand kinematic models through grasp-oriented intra-finger dependencies¹. Utilizing the NinaPro database—the largest publicly available dataset on hand kinematics—comprising synchronously collected hand joint angle values from 77 subjects performing 23 functional movements related to activities of daily living (ADL), we developed sparse models that maintain accuracy while reducing complexity. After rigorous data preprocessing to ensure quality, including isolating only joint angle data within anatomical ranges of motion (ROMs), and removing experiment runs with insufficient ROM for proper inference and modeling, we analyzed 16 finger joints performing flexion/extension (FE) movements, which cover most of the hand’s workspace due to hand anatomy. Through this focused approach, we identified 116 highly to very highly correlated pairwise intra-finger dependency-movement relationships across all grasps.

Through regularized generalized linear models (GLM), we selected uncorrelated predictors for each relationship. We then applied weighted linear mixed-effects models (LME) to account for both subject-specific random effects and dependency-specific fixed effects. This approach produced interpretable models with absolute weighted mean absolute error (wMAE) values ranging from 2.4 to 16° (median 7.5°) and relative double weighted mean absolute percentage error (wwMAPE) values from 11 to 56.1% (median 27.9%). To streamline implementation, hierarchical clustering reduced these 116 dependencies to just 30 clustered models while maintaining prediction accuracy.

¹This chapter is based on the findings presented in (Bazina et al., 2024c).

Our methodology offers a significant advantage over previous approaches by providing reduced grasp-oriented models requiring 5 to 15 degrees of freedom (median 12 DOFs), compared to the hand’s full 16 flexion/extension DOFs, while providing directly interpretable, one-to-one intra-finger joint relationships. This framework provides a foundation for designing more efficient rehabilitation and assistive devices that balance biomechanical accuracy with practical simplicity.

Contribution of this Chapter

The main contributions of this chapter can be summarized as follows:

- Development of a systematic approach for curating hand kinematics data, including preprocessing techniques that ensure anatomically valid joint movements.
- Introduction of a framework for identifying and modeling intra-finger joint dependencies, producing interpretable reduced hand kinematics models for grasping.
- Synthesis of reduction models into clusters across all grasps, reducing implementation complexity while maintaining prediction accuracy.

Limitation of the Study

While the NinaPro dataset used in this study remains the largest publicly available hand kinematic database (77 participants), it has notable demographic limitations, being predominantly male and focused exclusively on young adults (22 to 35 years). The recently released CeTI-Age dataset (Muschter et al., 2023), though 18% smaller with 63 participants and containing 20 distinct grasp types versus NinaPro’s 23, offers better demographic balance (33 female/30 male) and spans a much broader age range (20 to 80 years), enabling more inclusive analysis of hand kinematics across the adult lifespan.

3.1 Reducing Hand Kinematics: State-of-the-Art

The human hand, with more than 20 DOFs excluding the wrist (Engelhardt et al., 2020), excels in precision and power grips, but replicating its full functionality in devices is challenging due to kinematic complexity and spatial constraints. Effective

rehabilitation devices must minimize DOFs while supporting essential ADL tasks like opening bottles, cutting, or writing (Jarque-Bou et al., 2020a).

Developing reduced and representative kinematic models requires a thorough understanding of hand kinematics, achieved through studies based on experimentally recorded hand movements (Li et al., 2022). For example, (Holzbaur et al., 2005) implemented a musculoskeletal model of the 50th percentile male upper extremity, including the wrist, index finger, and thumb, which was later expanded in (Ma et al., 2020b) to include additional fingers using OpenSim (Delp et al., 2007). Similarly, (Engelhardt et al., 2020) employed the AnyBody Modeling SystemTM to develop a comprehensive hand model incorporating detailed anatomical structures with physiologically idealized joint and muscle-tendon units, which enabled realistic simulation of complex hand movements and force transmission mechanisms. These studies primarily focused on detailed hand modeling for musculoskeletal research rather than reducing DOFs.

The human hand, with its 27 bones (8 carpal bones, five metacarpals, and 14 phalanges), 41 muscles (20 in the forearm and 21 within the hand itself), and numerous joints, represents one of the most anatomically complex structures in the human body (Sobinov and Bensmaia, 2021). This intricate architecture enables at least 21 actively articulated DOFs, excluding the wrist, with five corresponding to the thumb (T) and four corresponding to each of the index (I), middle (M), ring (R), and little (L) fingers. Each finger consists of phalanges that move relative to one another, enabling finger flexion/extension (FE). The I, M, R, and L fingers each have two joints between their phalanges (the distal interphalangeal (DIP) and proximal interphalangeal (PIP) joints). In contrast, the thumb has only one interphalangeal joint (IP). Additionally, each digit has a metacarpophalangeal (MCP) joint enabling abduction/adduction (AA) movement with a slight rotation in addition to FE. At the base of each digit are the carpometacarpal (CMC) joints, with those of the thumb and little finger being highly mobile. The thumb's CMC joint enables FE, AA, and rotation, facilitating opposition, while the little finger's CMC joint enables AA and contributes to palmar arching. In contrast, the CMC joints of the index, middle, and ring fingers primarily provide stability. The complexity extends beyond this skeletal framework to the sophisticated neuromusculoskeletal system, where many muscles act across multiple joints, creating complex relationships between muscle activation and joint movement. This anatomical complexity is further compounded by significant interpersonal variability. Understanding these intricacies is essential for developing

effective hand rehabilitation strategies and simplified yet functionally accurate kinematic models.

Efforts to create reduced kinematic models, such as (Cobos et al., 2010; Delp et al., 2007), were limited by small sample sizes (fewer than 10 subjects) and overly simplified grasp types (prismatic and circular division only). In (Zhang et al., 2022), a pneumatically driven soft robotic hand was developed using a kinematic model based on six subjects, establishing a linear relationship between PIP and DIP joints. Similarly, (Kamper et al., 2003) analyzed fingertip trajectories during reach-and-grasp tasks with ten subjects performing five grasps, revealing approximate linear relationships between PIP, MCP, and DIP joint angles, albeit with varying slopes (e.g., PIP—DIP slopes of 0.3 in (Kamper et al., 2003) versus 2/3 in (Cobos et al., 2010; Zhang et al., 2022)).

Principal component analysis (PCA) has been widely used for kinematic reductions. For instance, (Jarque-Bou et al., 2016) applied PCA on six subjects grasping cylindrical shapes, while (Jarque-Bou et al., 2020b) analyzed 22 subjects performing 26 ADL-related grasps, identifying five sparse hand synergies. In (Gracia-Ibáñez et al., 2020), PCA with Varimax rotation on data from 24 subjects performing 24 ADL identified two core synergies involving PIP and MCP joint flexions. More comprehensive analysis by (Jarque-Bou et al., 2019) using the NinaPro dataset required 12 synergies to account for only 80% of the variance. However, (Prevete et al., 2018) criticized PCA for failing to produce sparse synergies, instead combining all available DOF, and suggested alternative methods such as l_1 regularization and sparse dictionary learning.

PCA approaches traditionally interpret low-variance components as merely representing noise rather than meaningful control elements. However, research (Yan et al., 2020) has disproven this assumption. Study shows that grasping objects can be predicted from hand postures with accuracy $>50\%$ even after removing the first 20 synergies explaining $>90\%$ variance. This demonstrates that these supposedly "minor" components contain subtle information still under volitional control.

Implementing all synergies for prosthetic or rehabilitation device design is complex, as each synergy represents a linear combination of all available DOFs. Even simple grasping behaviors would require more than 20 independent control parameters to achieve human-equivalent precision. This highlights the practical challenges in implementing PCA-based approaches in rehabilitation robotics. To address these challenges, we propose a complementary approach by introducing simpler one-to-one joint de-

dependency relations that provide a more implementable framework for rehabilitation applications.

3.2 Data Cleaning, Exploration and Joint Dependency Identification

Kinematic recordings from 77 healthy volunteers (average age: 28.8 years with standard deviation 3.96; 57 males/20 females; 70 right-handed/7 left-handed) were analyzed using the publicly accessible NinaPro multimodal database (Ninapro, 2020). This section outlines the comprehensive data preparation workflow and intra-finger correlation analysis to identify dependency-movement relationships for subsequent modeling.

3.2.1 Data Relabeling and Preprocessing

This subsection outlines the data preparation workflow that creates a reliable dataset for hand kinematics modeling by relabeling data from multiple databases with inconsistent schemas, filtering to isolate relevant movements, and removing outliers to ensure anatomically plausible joint angles. The process eliminates experiment runs with insufficient samples and those covering too little ROM. These preprocessing steps are crucial for establishing valid intra-finger dependency relationships across the diverse subject population.

Data Relabeling

The dataset was compiled from three multimodal databases (NinaPro DB1, DB2, and DB5), each captured at different sampling rates: DB1 at 100 Hz, DB2 at 2 kHz, and DB5 at 200 Hz, comprising calibrated kinematic data from 27, 40 and 10 subjects, respectively (Jarque-Bou et al., 2020a). Significant relabeling was necessary to harmonize the data structure across databases. In the DB1 database, hand configurations and functional movements required correction of movement indices (converting 2 to 1 and 3 to 2) due to incorrect original numbering. Additionally, because multiple databases were merged, subject identifiers in the combined dataset no longer aligned with those in DB9 dataset index (Ninapro, 2020), requiring further relabeling. The compiled dataset contains 40 distinct hand movements plus a rest position, organized into two exercise groups from (Jarque-Bou et al., 2020a): Exercise B (labeled as 1) featuring eight isometric and

isotonic hand configurations with nine basic wrist movements, and Exercise C (labeled as 2) comprising 23 grasping and functional movements with everyday objects.

In the original DB2 dataset (subjects 28 to 67), functional movements for Exercise 2 (labeled as `restimulus` in the source data) required renumbering to ensure consistent movement indexing across databases. This standardization was accomplished by subtracting 17 from each exercise ID. The resulting relabeled dataset—with consistent movement indexing—was stored in `Apache Parquet` file format (see Table 3.1 for complete identifiers). The Parquet format was selected for its columnar storage architecture, which enables efficient data compression and the ability to process large-scale kinematic data in manageable chunks, allowing subsequent analysis steps.

Table 3.1 Dataset identifiers for the relabeled hand kinematic dataset: subject demographics and experimental conditions

Subject	Hand laterality	Gender	Age	Height	Weight	Exercise	Movement	Repetition
1–77	Right, Left	Male, Female	22–45	150–192	44–105	1, 2	1–23	1–6

The relabeled data is then concatenated by rows into a `s1-77_e1-2.parquet` file, consisting of 183 773 343 observations of 22 joint angle features in degrees (a total of 4 043 013 546 data points). Each feature label is created by concatenating joint name, finger number, and joint movement identifiers. Joint names are abbreviated as: `CMC`, `MCP`, `IP`, `PIP`, `DIP`, and `WRIST`. Finger identifiers are numbers from 1 to 5, starting from thumb. Joint movement is denoted with the small letter `f` for flexion/extension, `a` for abduction/adduction, and `d` for `WRIST` deviation. For example, `MCP5_f` represents the MCP joint of the fifth finger performing flexion/extension. Movement indicator can be omitted if the joint supports only a single type of movement. Nine subject and experiment identifiers from Table 3.1 were concatenated to each observation, expanding the dataset to 31 total columns. This completed the data relabeling, producing a comprehensive dataset with kinematic measurements and subject-specific metadata for subsequent analyses.

Data Preprocessing

The dataset was analyzed using `Apache Spark 3.1` with the `tidyverse` package (Wickham et al., 2019) and its `R` interface, `sparklyr` (Luraschi et al., 2019). Rigorous

data preprocessing was essential due to inherent experimental data acquisition errors that produced anatomically impossible joint angles. Initial preprocessing identified all missing values (NAs) in the dataset, revealing that the AA difference between index and middle fingers (MCP2_a column) consisted entirely of NAs. This aligns with (Jarque-Bou et al., 2020a), which noted that these measurements were excluded due to sensor noise, removing this column from further analysis. Since the data was collected as a continuous time series without timestamps, the dataset was filtered to retain only distinct rows, eliminating potential duplicates representing identical hand postures.

In the second preprocessing step, we isolated only Exercise 2 (C), which contains the 23 grasping and functional movements shown in Figure 3.1. All AA movements were excluded from analysis since they represent relative angle differences between adjacent fingers rather than absolute deviations from a neutral position. The rest position was removed as it does not represent functional grasping behavior. These filtering operations reduced the dataset to 25 column features (joint angles and identifiers) and 50 866 742 rows of observations, creating a focused dataset that contains only FE movements and is tailored explicitly for analyzing hand kinematics during functional grasping tasks.

The relabeled hand movement dataset was organized hierarchically according to subject, movement type, and joint angle to facilitate further preprocessing. For each hierarchical grouping, we generated comprehensive boxplot statistics to facilitate summary-based inference:

- Sample size,
- Range boundaries (minimum and maximum values),
- Central tendency measures (mean and median),
- Distribution quartiles (Q1 and Q3).

The interquartile range ($IQR = Q3 - Q1$) is particularly informative, as it represents the middle 50% of angular movement during functional tasks. To comprehensively analyze joint behavior while accounting for individual differences, we structured the data analysis in a two-level hierarchical framework:

1. **Subject level:** All repetitions for each subject were grouped to capture individual movement patterns and variability.
2. **Movement level:** Subject-level statistics were aggregated to characterize joint behaviors across the entire participant population.

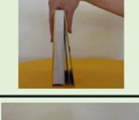
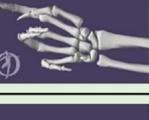
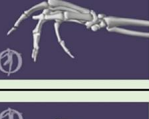
Exercise C							
1	Large diameter grasp			13	Tripod grasp		
2	Small diameter grasp (power grip)			14	Prismatic pinch grasp		
3	Fixed hook grasp			15	Tip pinch grasp		
4	Index finger extension grasp			16	Quadpod grasp		
5	Medium wrap			17	Lateral grasp		
6	Ring grasp			18	Parallel extension grasp		
7	Prismatic four fingers grasp			19	Extension type grasp		
8	Stick grasp			20	Power disk grasp		
9	Writing tripod grasp			21	Open a bottle with a tripod grasp		
10	Power sphere grasp			22	Turn a screw (grasp the screwdriver with a stick grasp)		
11	Three finger sphere grasp			23	Cut something (grasp the knife with an index finger extension grasp)		
12	Precision sphere grasp						

Figure 3.1 Graphical representation of 23 grasping and functional movements from Exercise C, using everyday objects to simulate ADLs (Jarque-Bou et al., 2020a).

This hierarchical approach, detailed in Table 3.2, ensured that each subject contributed equally to the movement-level statistics, preventing subjects with more repetitions or observations from dominating the analysis.

Table 3.2 Grouping data structure for boxplot and summary data on grasping.

Joint Angles	Movement	Subject	Subject level summary	Movement level summary
CMC1_f	1	1	Min, max, mean, median, Q1, Q3, IQR	Median of medians, mean IQR
		2	Min, max, mean, median, Q1, Q3, IQR	
		
MCP1_f	1	1	Min, max, mean, median, Q1, Q3, IQR	Median of medians, mean IQR
		2	Min, max, mean, median, Q1, Q3, IQR	
		
...
CMC1_f	2	1	Min, max, mean, median, Q1, Q3, IQR	Median of medians, mean IQR
		2	Min, max, mean, median, Q1, Q3, IQR	
		

Figures 3.2a and 3.2b illustrate the movement-level distribution of subject-level joint angle medians for DIP3 and MCP2_f across all movements. The authors' GitHub repository (Bazina, 2022b) provides comprehensive boxplots for all joints. Comparing the boxplots reveals significant differences in anatomical validity: most median subject-level joint angle values for DIP3 (Figure 3.2a) fall outside the expected anatomical range, while MCP2_f values (Figure 3.2b) predominantly remain within normal limits. This discrepancy indicates that a negative sign convention was inadvertently used for DIP3 flexion angle measurements in the original database—a pattern also observed with CMC5, DIP4, and DIP5 joints. The database creators themselves acknowledged measurement limitations in (Jarque-Bou et al., 2020a):

"DIP sensors provide reliable angles when a subject's hand size is large (i.e., when the glove properly fits the hand). They may provide partial results when the hand of the subject is small. Therefore, attention needs to be taken when using the information."

This caveat is particularly relevant to our analysis. While most joint angles align with anatomical expectations (as demonstrated by MCP2_f in Figure 3.2b), detailed examination of PIP3 and PIP4 measurements reveals several values extending beyond

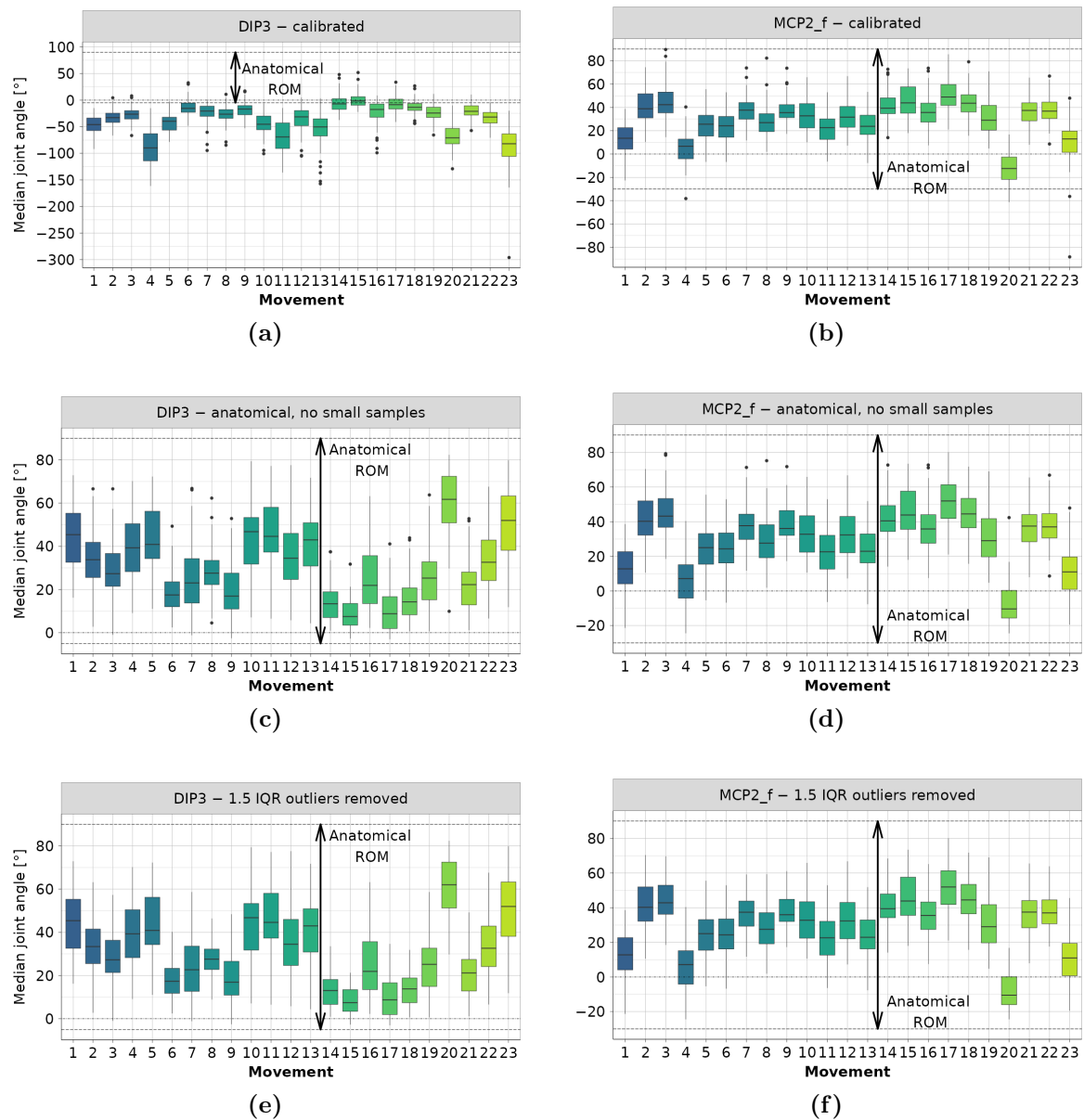


Figure 3.2 Example steps for joint angle data preprocessing: (a) DIP3 – calibrated data, (b) MCP2_f – calibrated data, (c) DIP3 – filtered to anatomical ROM and small samples removed, (d) MCP2_f – filtered to anatomical ROM and small samples removed, (e) DIP3 – outliers removed using iterative 1.5 IQR rule, (f) MCP2_f – outliers removed using iterative 1.5 IQR rule.

anatomical limits. These anomalies likely stem from the combined effects of sensor noise and anthropometric variations when the same data-collection glove was used across subjects with different hand dimensions (Jarque-Bou et al., 2020a).

The following preprocessing step involves implementing anatomical validation by isolating only physiologically plausible joint angles. As illustrated in Figures 3.2c and 3.2d, the sign for PIP3 joint angle data is inverted, and all measurements falling outside established anatomical range constraints (see Table 3.3) were systematically replaced with NA values rather than being removed entirely. This selective NA replacement strategy ensures data preservation. Discarding entire observations due to a single noisy sensor reading would result in unnecessary data loss, given that other sensor readings in the same observation may still be valid.

Table 3.3 Anatomical ROM limits for digit joints during FE movement (Cobos et al., 2010; Colombo and Sanguineti, 2018; Holzbaur et al., 2005).

Finger 1 (Thumb)/°			Fingers 2 to 4/°			Finger 5 (Little)/°			
CMC1_f	MCP1	IP1	MCP_f	PIP	DIP	CMC5	MCP5_f	PIP5	DIP5
-15-50	-40-45	-5-75	-30-90	-5-120	-5-90	0-15	-30-90	-5-135	-5-90

Finally, to ensure high-quality data for modeling, we implemented a two-phase filtering process that preserved only recordings with adequate statistical power and functional relevance. In the first phase, we aggregated joint angle data by joint type and movement to calculate the movement-level IQR—a robust metric representing the middle 50% of angular motion during each grasp (Figure 3.2). Two filtering criteria were applied:

- Samples with fewer than 100 observations were replaced with NA values to ensure statistical reliability.
- Samples where the joint’s motion range was less than 50% of the typical range for that movement ($\text{IQR share} = \frac{\text{subject IQR}}{\text{movement-level IQR}} < 0.5$) were replaced with NA values, as they failed to capture sufficient functional motion.

While this initial filtering eliminated many outliers (Figures 3.2a–3.2d), subtler anomalies remained. The second filtering phase applied an iterative 1.5 IQR rule (Rousseeuw and Hubert, 2011) to each joint-movement combination. After recalculating movement-level quartiles, subject medians outside $Q1 - 1.5 \times \text{IQR}$ or $Q3 + 1.5 \times \text{IQR}$ were identified as outliers and removed. This process was iterated six times until convergence, yielding a refined dataset containing only biomechanically plausible values without outliers (Figures 3.2e–3.2f).

3.2.2 Intra-Finger Correlation Analysis

The distribution of valid data across subjects, fingers, and movements was analyzed through contingency tables to assess subject representation imbalances after preprocessing. A contingency table is a matrix-format visualization that displays the frequency distribution between categorical variables, allowing identification of patterns and potential biases in data representation. Figure 3.3 visualizes this three-way relationship in a matrix plot where each cell represents a subject-finger combination. The size of each shape indicates the number of remaining movements (ranging from 1 to 23) for that specific subject-finger pair following data preprocessing, while the color intensity represents the average number of observations per movement. This visualization effectively highlights both the movement diversity captured per subject across different fingers and the data concentration for each combination, providing critical context for evaluating how specific subject groups might disproportionately influence subsequent analyses and modeling results.

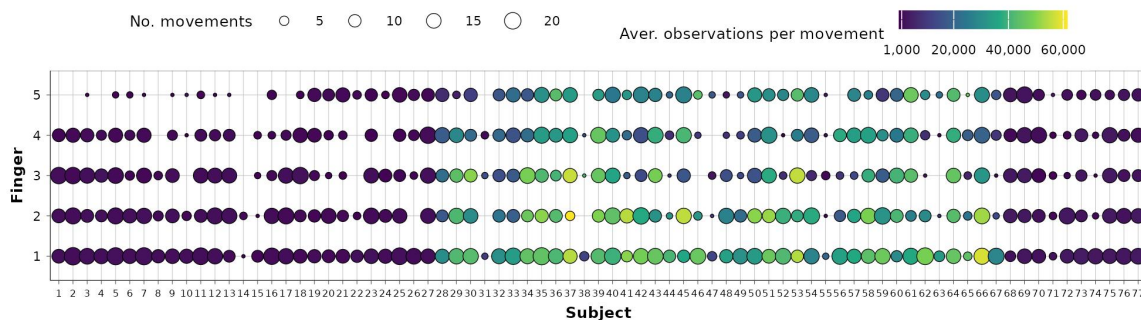


Figure 3.3 Contingency tables showing data distribution across subjects and fingers after preprocessing. Each cell represents a subject-finger combination, with shape size indicating the number of remaining valid movements (ranging from 1 to 23), and color intensity showing the average number of observations per movement.

The contingency analysis reveals a substantial sampling imbalance across database groups. Subjects 1 to 27 and 68 to 77 (from DB1 and DB5) typically contain fewer than 3000 observations per movement (including all repetitions). In contrast, subjects 28 to 67 (from DB2) have an order-of-magnitude higher sampling density, ranging from 20 000 to 60 000 observations per movement. This data distribution disparity stems from different acquisition protocols and sampling rates (100 Hz for DB1, 2 kHz for DB2, and 200 Hz for DB5). Without appropriate sampling strategies, such as stratified sampling or weighted analyses, models trained on the combined dataset would

disproportionately reflect the movement patterns of subjects from DB2, potentially masking important kinematic variations present in the less densely sampled subjects.

For analysis and modeling, 18 potential intra-finger dependencies are identified using 16 finger joints performing FE (Table 3.4). These dependencies systematically combine all joints within each finger, with the proximal joint of the kinematic chain selected as the movement basis. All 18 possible relationships were defined and evaluated for each of the 23 grasps, creating a comprehensive investigation framework of 414 potential dependency-grasp combinations. The feasibility of modeling each specific relationship will be determined through correlation analysis, as not all joint relationships exhibit sufficient correlation to warrant modeling across all grasping patterns.

Table 3.4 18 pairwise intra-finger joint dependencies investigated for hand kinematic model reduction across functional grasping movements.

Thumb	Index	Middle	Ring	Little
MCP1 – IP1	MCP2_f – PIP2	MCP3_f – DIP3	MCP4_f – DIP4	CMC5 – MCP5_f
CMC1_f – MCP1	MCP2_f – DIP2	MCP3_f – PIP3	MCP4_f – PIP4	CMC5 – DIP5
CMC1_f – IP1	PIP2 – DIP2	PIP3 – DIP3	PIP4 – DIP4	CMC5 – PIP5
				MCP5_f – DIP5
				MCP5_f – PIP5
				PIP5 – DIP5

To systematically identify linear relationships between joint movements, data were nested by finger, movement (restimulus), subject, and repetition, and correlation matrices were generated for all FE joints within each nested group across the full range of motions, following the procedure illustrated in Figure 3.4.

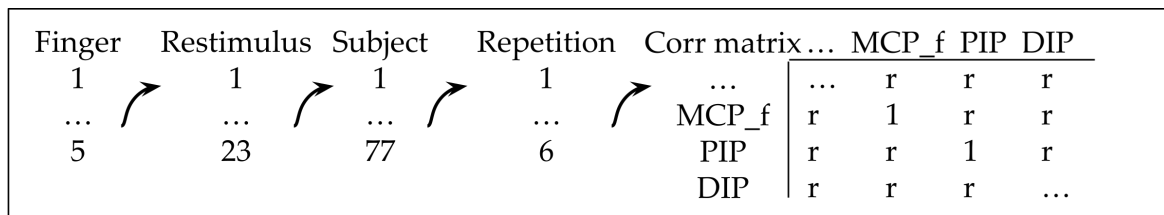


Figure 3.4 Hierarchical data nesting procedure for generating correlation matrices across flexion/extension joints. Data is systematically nested by finger, movement (restimulus), subject, and repetition to isolate meaningful relationships.

This analysis yielded 71 328 Pearson correlation coefficients r , each quantifying the strength and direction of joint-pair relationships on a scale from -1 to 1 . The number of coefficients per movement joint dependency ranged from 56 to 358, with multiple observations from each subject-repetition combination, providing robust statistical

power for assessing potential kinematic couplings across diverse hand sizes and movement patterns. Statistical significance was evaluated using a 5% significance level, ensuring that only meaningful correlations were considered for subsequent modeling of intra-finger dependencies.

Figure 3.5 presents boxplot summary statistics for correlation coefficients across nine intra-finger dependencies, specifically for the third finger during movement 21 (Figure 3.5a) and the fifth finger during movement 2 (Figure 3.5b). Color highlighting indicates the strength of each relationship, with the color map applied only to dependencies exhibiting high or very high correlation (absolute median correlation coefficient $|r| \geq 0.7$) according to the classification system recommended by (Mukaka, 2012).

Despite the generally tight distribution of coefficients around the median for strongly correlated dependencies, some boxplots revealed significant outliers that could potentially distort modeling results. To address this issue, we applied an iterative 1.5 IQR rule to systematically identify and remove statistical anomalies. This outlier removal process eliminated 4037 values (5.7% of the total) while preserving 67 291 valid correlation coefficients. The right panels in Figures 3.5a and 3.5b display the distributions after outlier removal, demonstrating more consistent correlation patterns. Complete visualization sets for all fingers, movements, and intra-joint dependencies are available in the authors' GitHub repository (Bazina, 2022b).

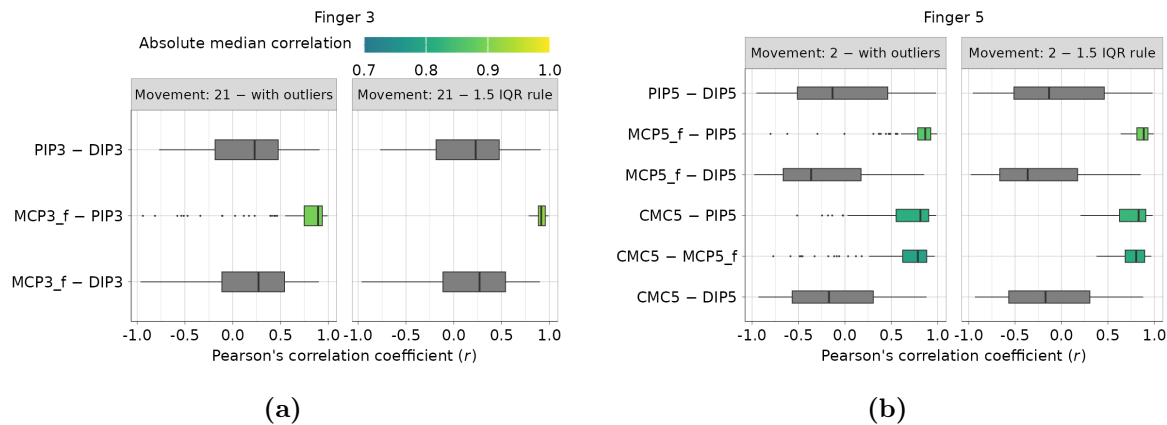


Figure 3.5 Boxplot distributions of correlation coefficients for intra-finger joint dependencies before (left) and after (right) iterative 1.5 IQR outlier removal: (a) middle finger (3rd) dependencies during movement 21, and (b) little finger (5th) dependencies during movement 2. Color highlighting indicates strength of correlation.

Next, we focused exclusively on analyzing dependencies exhibiting an absolute median correlation coefficient of $|r| \geq 0.7$, which are categorized as highly or very

highly correlated according to established thresholds in (Mukaka, 2012). Detailed visual inspection of scatter plots revealed that some movement repetitions captured only partial ROMs, potentially skewing correlation estimates. To ensure data quality and representativeness, we repeated two additional, previously introduced, filtering methods, but at the repetition level for each dependency:

- Repetitions with insufficient ROMs were discarded using an IQR share threshold of 0.5: $\text{IQR share} = \frac{\text{repetition IQR}}{\text{median dependency-movement IQR}} < 0.5$
- Remaining outlier values were removed through an iterative application of the 1.5 IQR rule targeting correlation coefficient distributions.

This rigorous filtering process yielded 11 643 statistically reliable correlation coefficients suitable for subsequent modeling steps. Figure 3.6 visualizes these dependency-movement relationships, where each point represents a median correlation coefficient across all qualifying repetitions. The diagram reveals clear clustering patterns among highly correlated intra-finger dependencies, providing insight into which joint relationships consistently exhibit strong coupling across different grasping movements and subject populations.

Analysis of the 18 defined intra-finger dependencies revealed that 16 demonstrate high correlation in at least one of the 23 functional grasping movements. Notably, two dependencies—PIP5 – DIP5 and PIP4 – DIP4—showed no significant kinematic coupling during any of the examined grasps, suggesting greater independence in the distal joints of the ring and little fingers. The highest number of simultaneous joint dependencies occurred during small diameter grasp (movement 2) and fixed hook grasp (movement 3), with 10 and 11 correlated joint pairs respectively, indicating more constrained finger movements during these grasps. They are followed by 7 identified dependencies during large diameter grasp, medium wrap, power sphere grasp, precision sphere grasp and lateral grasp (movements 1, 5, 10, 12 and 17 respectively). In contrast, the tip pinch (movement 15) exhibited only a single correlation (PIP2-DIP2), demonstrating the highly selective joint control required for precision tasks.

Across different fingers, MCP FE demonstrated consistent coupling with PIP FE for the middle, ring, and little fingers in 18 to 20 movements. Interestingly, this same coupling appeared in only 7 movements for the index finger, highlighting its greater kinematic independence—a finding consistent with its specialized role in precision manipulation. The index finger’s PIP2 – DIP2 relationship, however, remained highly

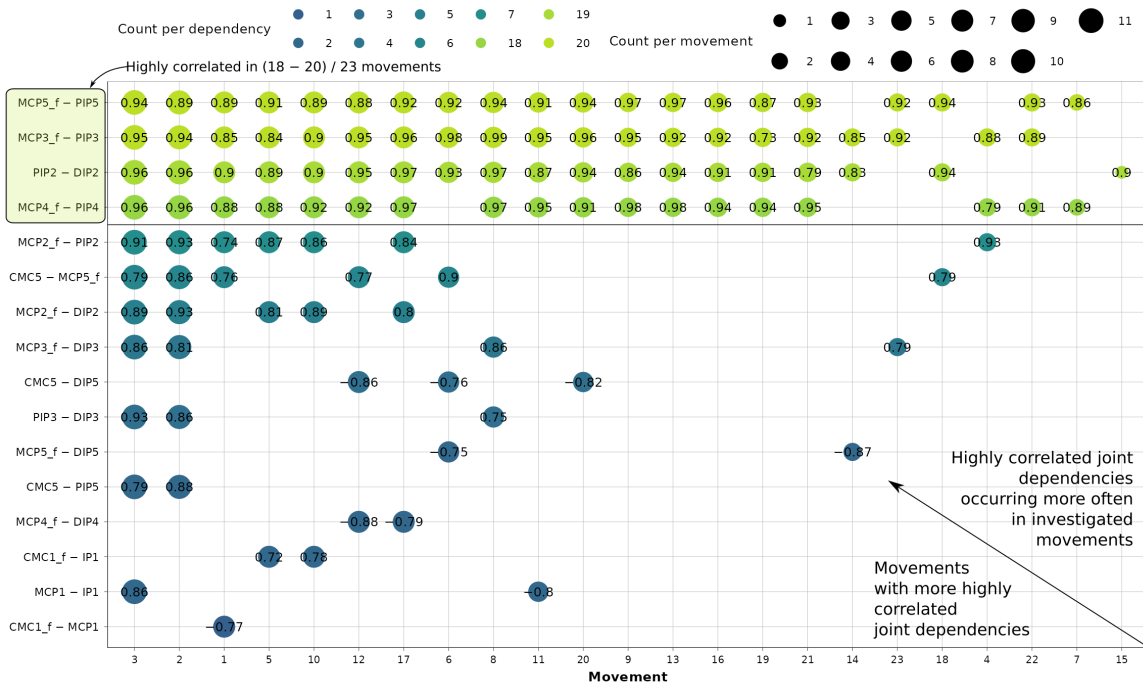


Figure 3.6 Comprehensive visualization of 116 highly and very highly correlated ($|r| \geq 0.7$) intra-finger joint dependencies across 23 functional grasping movements. Each point represents a median correlation coefficient after outlier removal, with colors indicating the number of movements in which the dependency is highly correlated. Horizontal movement sorting is performed based on the number of coordinated joint relations, while vertical sorting indicates frequently occurring dependency patterns across multiple movements. Note the sparse representation of thumb dependencies at the bottom of the diagram, confirming the thumb’s greater independence in functional grasping tasks compared to other fingers.

correlated across 19 movements, suggesting a fundamental mechanical coupling in the distal segments.

Thumb intra-finger dependencies were notably sparse, with only 5 relationships identified across 5 movements, confirming the thumb’s greater functional independence in grasping activities. This finding aligns with previous biomechanical research by (Kamper et al., 2003), which established the thumb’s unique kinematic behavior compared to other digits due to its specialized anatomical structure and critical role in opposition movements. The extensive correlation analysis across all fingers and movements yielded a total of 116 dependency-movement relationships exhibiting high or very high correlation, which were selected for more detailed mathematical modeling and kinematic reduction in the following sections.

To better understand representativeness and potential sampling biases within our dataset, we conducted an in-depth analysis of the distribution of observations across dependency-movement relationships. This analysis is essential for evaluating the generalizability of our models and identifying potential limitations due to subject or database imbalances.

Figure 3.7 presents stacked frequency histograms of observations for two contrasting dependencies: a frequently occurring, highly correlated relationship (MCP3_f – PIP3), and a less common relationship (CMC5 – MCP5_f) with a correlation coefficient of $r = 0.76$. These visualizations reveal important differences in data composition that could influence modeling outcomes.

For the MCP3_f – PIP3 relationship during movement 3 (Figure 3.7a), the dataset includes 34 subjects contributing 155 repetitions and 634 050 total observations. This relationship demonstrates relatively balanced representation, with subjects from DB1 (subjects 1 to 27) and DB2 (subjects 28 to 67) well-represented, and only 4 participants from DB5 (subjects 68 to 77).

In contrast, the CMC5 – MCP5_f relationship during movement 1 (Figure 3.7b) presents a more skewed distribution. This relationship includes 20 subjects performing 75 repetitions, yielding 485 267 observations. Unlike the first example, this dependency is predominantly characterized by subjects from DB2, with notably fewer representations from DB1 and DB5. Comprehensive distribution visualizations for all 116 dependency-movement relationships are available in the authors' GitHub repository (Bazina, 2022b).

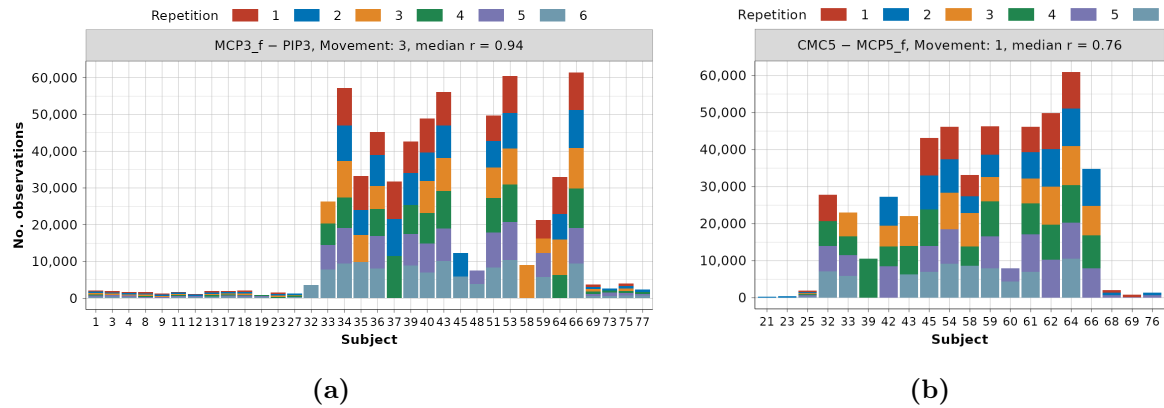


Figure 3.7 Stacked frequency histograms showing data distribution across subjects and repetitions for two intra-finger dependencies: (a) MCP3_f – PIP3 during movement 3, representing a frequently occurring relationship, (b) CMC5 – MCP5_f during movement 1, a less common relationship.

Figure 3.8 summarizes the remaining data per dependency-movement. The minimum number of subjects per relationship is 9, with the middle 50% ranging from 19 to 33. The number of repetitions per dependency-movement spans 25 to 274, with a midsread of 3 to 4.5 repetitions per subject.

Figure 3.8 presents a comprehensive statistical summary of the data distribution across all 116 identified dependency-movement relationships. The analysis reveals substantial variability in subject representation, with a minimum of 9 subjects per relationship and an interquartile range (middle 50%) spanning from 19 to 33 subjects. This robust subject representation enhances the generalizability of derived models across different hand anthropometrics. The within-subject motion variability of the dataset is evidenced by the wide range of repetitions captured per dependency-movement relationship, from 25 to 274 total repetitions across all subjects. When normalized to individual participants, this translates to a midsread of 3 to 4.5 repetitions per subject—sufficient for capturing both consistent patterns and natural variability in movement execution. These statistics confirm the dataset’s adequacy for developing statistically sound models of intra-finger dependencies while accounting for individual differences in grasp execution.

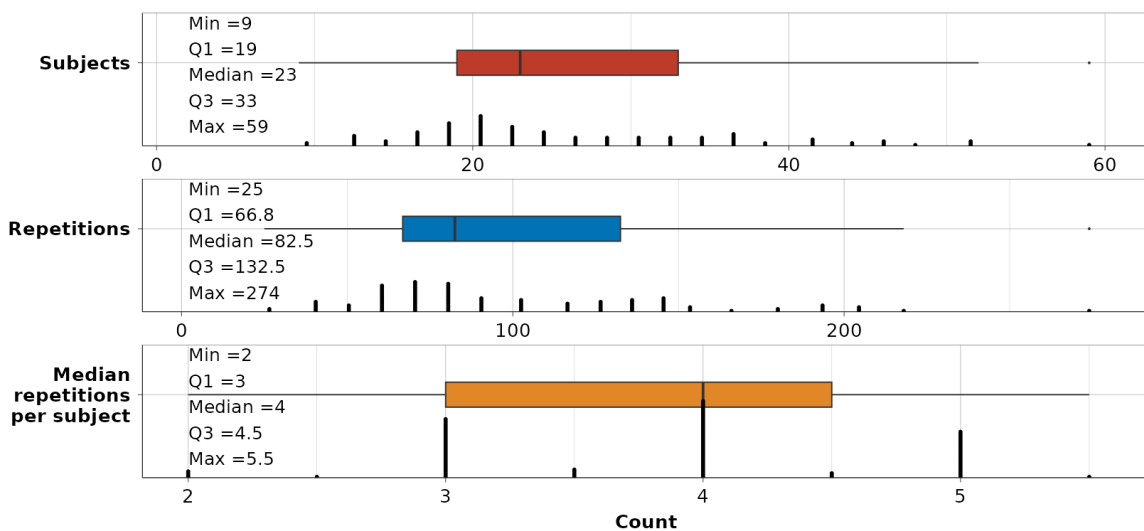


Figure 3.8 Data summary for all 116 dependency-movement relationships.

3.3 Dependency-Movement Relationship Modeling

Traditional machine learning principles are applied to dependency-movement modeling, with approximately 80 % of repetitions allocated for training and the remaining 20 % reserved for testing. It is assumed that both the reaching and returning-to-rest phases follow the same trajectory.

Due to dataset imbalances caused by varying sampling rates across the three dataset parts (DB1, DB2, and DB3), the data is sampled per dependency-movement relationship by setting aside entire repetitions. This ensures that repetitions in the test set belong to different subjects, increasing model representativeness.

Customized Stratified Sampling Procedure

A customized version of stratified sampling is used to split the training data into k folds for hyperparameter tuning through cross-validation. To determine the number of folds, the minimum number of subjects (9) and repetitions (25) from Figure 3.8 is considered. At least 5 repetitions per stratum are deemed sufficient to maintain variability. The data is then split into 5 folds, with one fold (20 % of repetitions) used as a test set and the remaining 4 folds used for cross-validation and hyperparameter tuning.

The customized stratified sampling process is performed as follows:

1. A vector of fold IDs is generated, repeating sequences in the range of 1 to 5, matching the number of repetitions in each relationship.
2. The vector of subjects is randomly shuffled, followed by random shuffling of repetitions belonging to each subject, creating a randomized list of repetitions.
3. Randomized repetitions are assigned to folds sequentially.

This procedure ensures that more unique subjects are present in each fold, resulting in more consistent 4-fold cross-validation compared to simple random repetition assignments. Each fold contains an uneven number of observations but an approximately equal number of repetitions, improving model reliability.

As illustrated in Figure 3.7, the dataset exhibits imbalances. Observation weighting is introduced to ensure that each repetition contributes equally to the model without increasing the dataset size further, in contrast to duplicating observations.

The weighting procedure involves:

1. Counting the total number of observations and repetitions per dependency-movement relationship.
2. Dividing these values to obtain a total weight coefficient for each repetition.
3. Dividing the total repetition weight by the number of observations within that repetition to assign individual observation weights w_i .

Three predicting variables are chosen for the modeling process: the dependee joint, subject height, and subject weight. All variables are transformed using second-order polynomial and exponential functions and fed into a model matrix containing first-order interactions and an intercept term, totaling 46 terms. The model matrix is standardized by subtracting the mean from each variable and dividing by its standard deviation. The same standardization procedure is applied separately for each of the 116 modeled dependencies, including the dependent variable before fitting.

Two different modeling approaches are employed, the first serving as a baseline and a variable selection model, and the second as a main model for inferring about the modeled dependencies.

Generalized Linear Model

For variable selection, a regularized generalized linear model (GLM) is employed using the `glmnet` library (Tay et al., 2023). The GLM consists of:

- A linear combination of predictors,
- A probability distribution for the dependent variable (assumed normal),
- A link function (identity function).

The standardized form of the GLM is expressed as:

$$E\left(\frac{y - \bar{y}}{\sigma_y}\right) = \beta_{s0} + \sum_{i=1}^n \beta_{si} \frac{x_i - \bar{x}_i}{\sigma_{x_i}}, \quad (3.1)$$

where $E(\cdot)$ denotes the expected value, y is the dependent joint, x_i are predictors, \bar{x}_i are variable means, σ_{x_i} are standard deviations, and β_{si} are standardized coefficients.

Lasso regression is used to promote sparsity by minimizing a loss function with a regularization term:

$$\lambda \sum_{i=0}^n |\beta_{si}|, \quad (3.2)$$

where λ is a tuning parameter. Additionally, relaxation of coefficients is introduced by combining regularized and OLS coefficients:

$$\beta_s^{\text{relax}}(\lambda, \gamma) = \gamma \beta_s^\gamma + (1 - \gamma) \beta_s^{\text{OLS}}, \quad (3.3)$$

where γ is the mixing parameter, β_s^γ is the regularized coefficient, and β_s^{OLS} is the Ordinary Least Squares (OLS) coefficient.

GLM models are selected based on sparsity and error metrics. The most regularized model within one standard deviation of the minimum cross-validated error is chosen. Observation weights are also applied to the GLM models.

Linear Mixed-Effect Model

The second modeling approach employed for inference is the linear mixed-effect model (LME), implemented using the `lme4` library (Bates et al., 2015). The LME model accounts for random effects due to subject grouping, observed during visual inspection (see Figure 3.11).

The LME model treats each subject as a random intercept, accounting for person-specific variations in joint relationships. This approach acknowledges that different individuals may have different baseline positions or angular offsets while maintaining similar coordination patterns. The fixed slopes represent population-level effects—the consistent biomechanical relationships between joints that apply across the entire population regardless of individual differences. These fixed effects quantify how much one joint’s movement predicts another joint’s movement, capturing the universal patterns in hand kinematics during specific grasps. This separation of fixed and random effects enables the identification of generalizable joint coordination patterns while accounting for individual variability. The model is expressed as:

$$\frac{y - \bar{y}}{\sigma_y} = \beta_{s0j} + \sum_{i=1}^n \beta_{si} \frac{x_i - \bar{x}_i}{\sigma_{x_i}}, \quad j \in S, \quad (3.4)$$

where β_{s0j} is the intercept for subject j from set S , representing subject-to-subject variability.

Model reduction is performed by retaining predictors with medium to large effect sizes (Cohen’s effect index “d “> 0.30) and high statistical significance ($p < 0.001$) (Cohen, 2013; Nieminen, 2022). The final model is obtained through iterative reduction based on predictor significance and effect size.

The intraclass correlation coefficient (ICC) is used to validate the modeling approach:

$$\text{ICC} = \frac{\sigma_s^2}{\sigma_s^2 + \sigma_r^2}, \quad (3.5)$$

where σ_s^2 is the variance of random effects (subject intercepts) and σ_r^2 is the residual variance.

According to (Koo and Li, 2016), ICC values indicate reliability as follows:

- < 0.5: Poor reliability,
- 0.5 – 0.75: Moderate reliability,
- 0.75 – 0.9: Good reliability,
- > 0.9: Excellent reliability.

The final LME model ensures robustness by accounting for subject-level variability, promoting generalizability across unseen subjects.

3.3.1 Random and Fixed Effect Predictors

The summary statistics of the obtained ICC values and the variance of random effects are presented in Figure 3.9. The median ICC value across all 116 models is 0.78, indicating good reliability of the modeling approach. Four models have an ICC below 0.5 (poor reliability), 46 models fall within the range of 0.5–0.75 (moderate reliability), 51 models are in the range of 0.75–0.9 (good reliability), and 15 models have an ICC above 0.9 (excellent reliability).

Although the inclusion of random effects in four models—23: MCP3_f–DIP3, 4: MCP4_f–PIP4, 17: MCP4_f–DIP4, and 2: MCP2_f–PIP2—is questionable due to ICC values below 0.5, the dependencies were selected based on mean correlations (see Figure 3.6) and are therefore retained in the analysis.

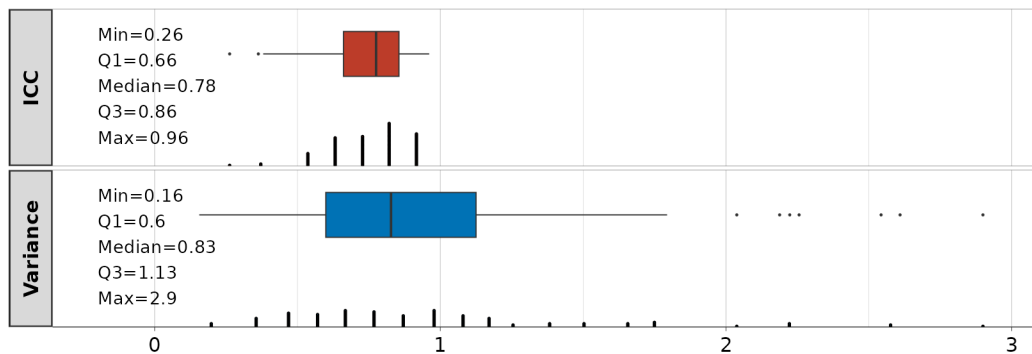


Figure 3.9 Intraclass correlation coefficients (ICC) and variance of random effects related to linear mixed-effect models (LME). The figure presents summary statistics for ICC values across all 116 models and the variance of subject intercepts.

The variance of random effects (subject intercepts) across all 116 LME models ranges from 0.16 to 2.9, with an IQR between 0.6 and 1.13. Detailed variance values and corresponding ICC statistics are available in Table S2 online².

A summary of the selected predictors in the final LME models, both significant and with medium to strong effect sizes, is provided in Figure 3.10. Four standardized predictors were identified: linear (*lin*), polynomial (*poly*), and exponential (*exp*) transformations of the dependee, as well as subject height. Additionally, five standardized interactions (denoted with “:”) were identified:

- Polynomial and exponential transformation of height (*poly:height_exp*),
- Polynomial and exponential transformation of weight (*poly:weight_exp*),
- Exponential and exponential transformation of height (*exp:height_exp*),
- Linear and polynomial transformation of height (*lin:height_poly*),
- Exponential and exponential transformation of weight (*exp:weight_exp*).

Including the random subject intercept, the average number of predictors per model is 2.5. Out of the 116 provided models, 83 contain linear terms, 78 contain polynomial terms, and 45 include both. Additionally, 11 models incorporate other predictors or interactions beyond linear and polynomial terms. A comprehensive analysis of model coefficients is presented in Appendix B (Figures B.1 and B.2).

After presenting the fixed-effect coefficients for each model, the random (subject) effect is summarized by presenting the intercept means across all subjects used for

²https://docs.google.com/spreadsheets/d/1ZnvPCa8ToHPTjjELyRAI_qMwQY0N3a84L_VyKS4ZvSs/edit?usp=sharing

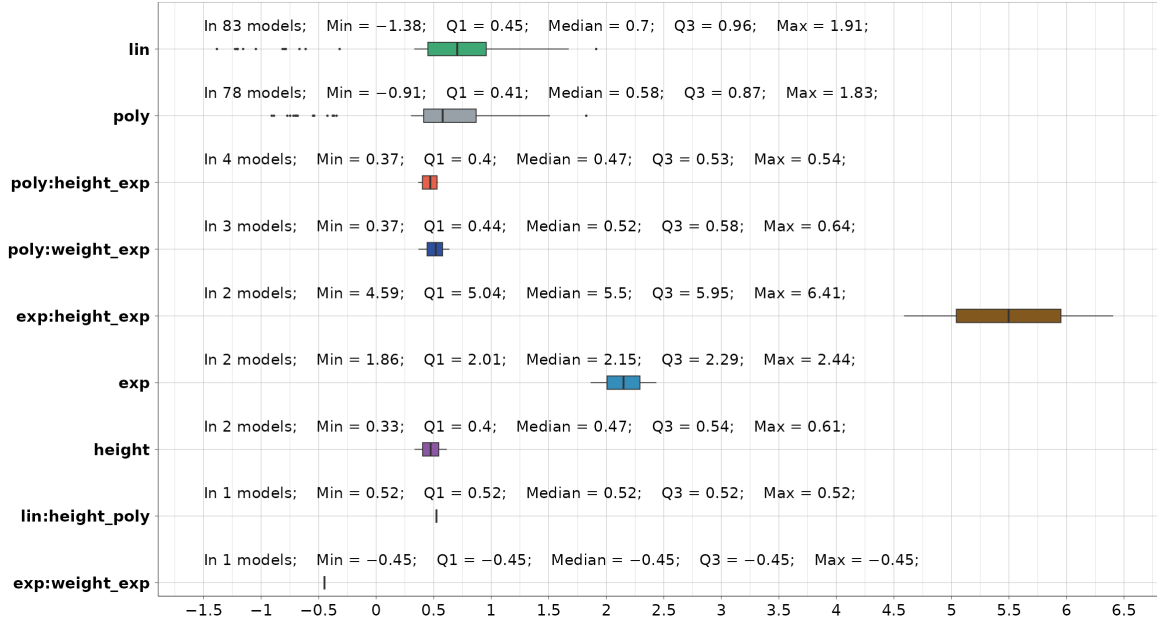


Figure 3.10 Summary statistics on selected predictors in the final LME models. The figure highlights the frequency of linear, polynomial, exponential transformations, and interactions used across 116 models.

modeling. These intercepts can be generalized and used as an unbiased estimator for the entire population, as shown in Figure B.2.

In Figure 3.11, two distinct dependency-movement relationships are presented across a subset of subjects and repetitions used for both training and testing data to visually validate the LME modeling approach. One relationship has a higher correlation coefficient (3: MCP3_f - PIP3), and the other has a lower one (12: MCP4_f - DIP4). A clear natural grouping of the data based on subjects is evident. Scatter plots for all modeled dependencies and subjects can be found in the authors' GitHub repository (Bazina, 2022b).

3.3.2 Model Error Metric Analysis

To validate the models, two error metrics are used, both weighted to balance the dataset. Since the data contains outliers, the weighted mean absolute error (wMAE) is selected as an absolute error metric for evaluating the models:

$$\text{wMAE} = \frac{1}{\sum_{i=1}^n w_i} \sum_{i=1}^n w_i |y_i - \hat{y}_i|, \quad (3.6)$$

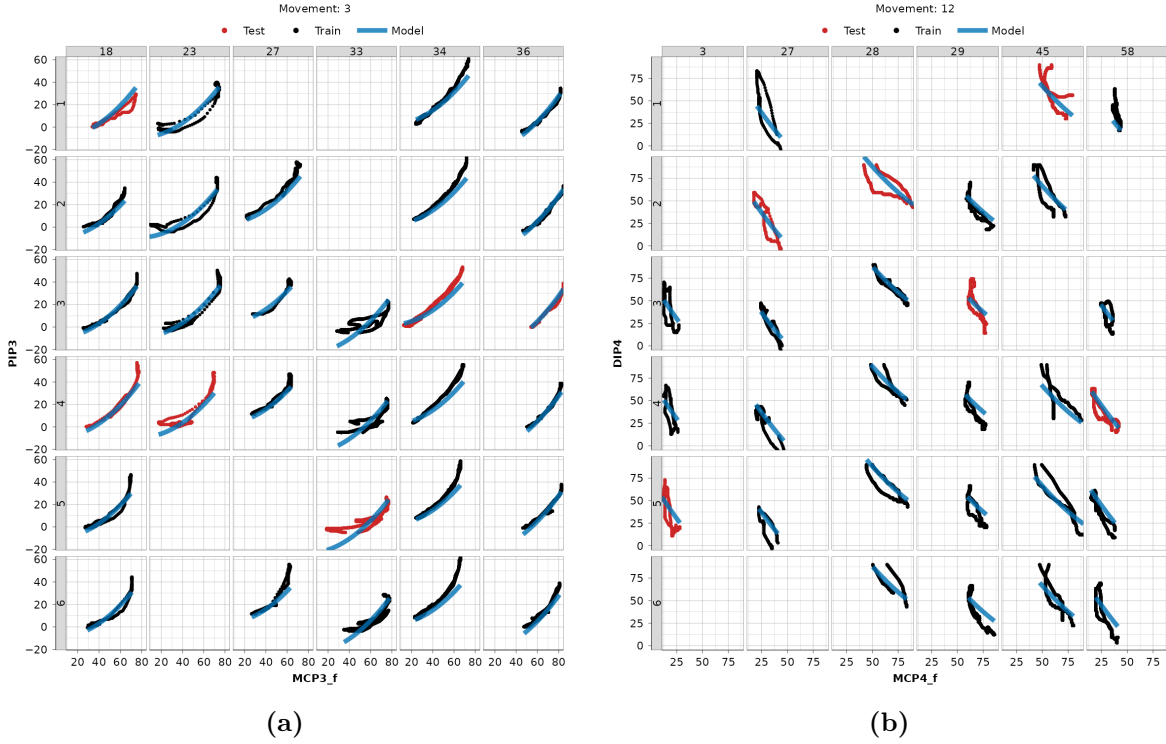


Figure 3.11 Examples of LME model fitted to data (blue) with repetitions belonging to train data (black) and test data (red). Numeration at the top represents the subject ID, and numeration to the left the repetition ID: (a) MCP3_f - PIP3 dependency for movement 3 (fixed hook grasp), (b) MCP4 - DIP4 dependency for movement 12 (precision sphere grasp).

where n represents the length of the train or test dataset, w_i the previously computed observation weight, y_i the observation of the dependent joint, and \hat{y}_i the predicted dependent joint value.

A relative metric, called the double weighted mean absolute percentage error (wwMAPE), is also used:

$$\text{wwMAPE} = \frac{\sum_{i=1}^n w_i |y_i - \hat{y}_i|}{\sum_{i=1}^n w_i |y_i|}, \quad (3.7)$$

with the same nomenclature as in Equation (3.6). wwMAPE is chosen because it behaves well for small, large, and close-to-zero joint angle values.

A summary of the statistics on the error metrics is depicted in Figure 3.12. It is evident that, compared to GLM models, the LME models fit the data with significantly smaller absolute and relative errors. The absolute wMAE for the LME approach across models ranges from 2.4° to 16° (median 7.5°) on the test dataset, and from 1.8° to 15.2° (median 7.2°) on the train dataset.

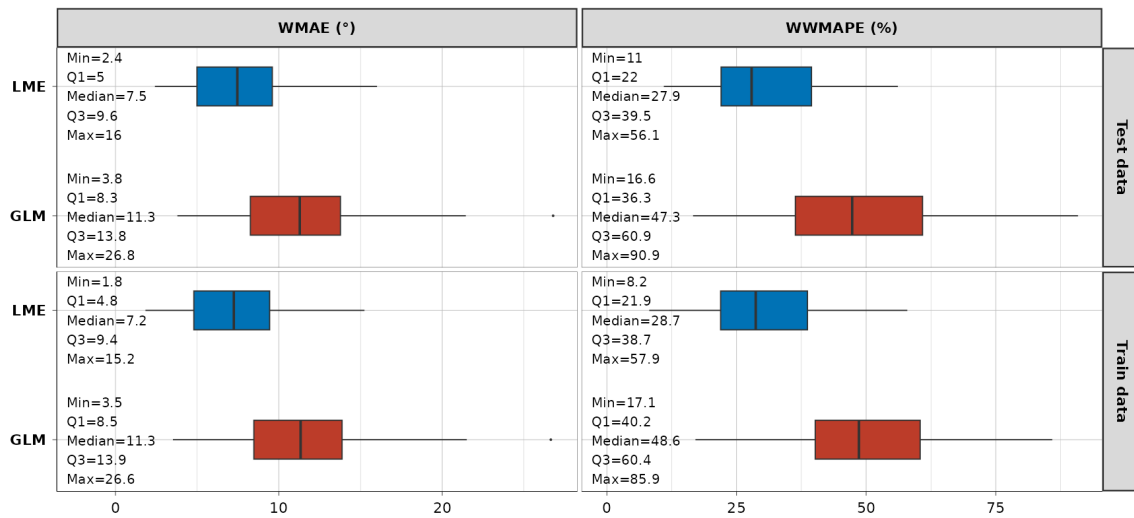


Figure 3.12 Summary statistics on wMAE and wwMAPE error metrics. The figure shows the comparison of absolute (wMAE) and relative (wwMAPE) errors on the train and test datasets for both GLM and LME models.

The relative wwMAPE for the same approach ranges from 11% to 56.1% (median 27.9%) on the test dataset, and from 8.2% to 57.9% (median 28.7%) on the training dataset.

Detailed graphical results of the error metric analyses are provided in Appendix B, with Figures B.3 showing wMAE and Figures B.4 showing wwMAPE. For readers' convenience, a detailed representation of these results is available as Table S1 online³.

3.3.3 Clustering Based on Model Coefficient Analysis

Agglomerative clustering was performed based on standardized coefficients to identify similarities between dependencies across different motions. The clustering utilized both fixed and random effects from the LME models, with missing coefficients replaced by zeros. A pairwise distance matrix was computed for the 116 identified models using Euclidean distance as the similarity metric between model coefficients.

Clustering was performed using the complete linkage method, where the distance between two clusters is defined by the largest distance between any two dependencies in each cluster. This approach, also known as “farthest neighbor clustering,” ensures

³<https://docs.google.com/spreadsheets/d/1JkbfzyNAdGuZEg0mXhJGEHI9DEgz nLNN34KvTpnEcuQ/edit?usp=sharing>

that clusters remain distinct and well-separated. The resulting dendrogram is shown in Figure 3.13.

After inspecting the dendrogram, the authors determined that cutting the tree at a distance of 0.52, resulting in 30 color-coded clusters, is an appropriate reduction strategy. This threshold was selected to ensure that the average absolute difference between standardized coefficients remained below 0.33, with each model containing an average of 2.5 coefficients.

The clustering process reduces the number of models required to describe all kinematic dependencies from 116 to 30 and decreases the number of models necessary to characterize each grasp type (see Table 3.5). The analysis of finger flexion/extension across all functional movements, initially involving 16 DOFs, can be reduced by up to 11 DOFs, with a median reduction of 4. The remaining flexion/extension grasp models consist of between 5 and 15 independent DOFs, with a median of 12. The number of reduced models per grasp ranges from 1 to 9, with a median of 4.

When the models are grouped into 30 clusters, the coefficients for each cluster can be estimated as the mean values of the standardized coefficients (refer also to Figures B.1 and B.2 in Appendix B) belonging to the clustered models, as depicted in Figure 3.14. In the figure, the minimum and maximum coefficient values per cluster are also presented, as are the singular clusters containing only one model.

The results of the LME modeling performed in this study show that the major factor in explaining the variance during the kinematic modeling and the model reduction of flexion/extension angles is the subject-to-subject variation, modeled as a random effect. The median value of variance explained by this “per subject” grouping structure is 78%.

This finding could potentially be attributed to the calibration protocol used for the database, which involved a post-processing procedure performed according to (Gracia-Ibáñez et al., 2016). The procedure utilized 10 subjects and 65 guided movements to compute sensor gain values, as referenced in (Jarque-Bou et al., 2020a), which were then applied to all subjects.

It is also noteworthy that the only selected coefficient for the “per subject” grouping was the intercept, allowing a constant shift in the data. For each of the 116 developed models in this research, all subjects used during the modeling process exhibited a similar pattern during the grasping motion but shifted by a subject-specific constant.

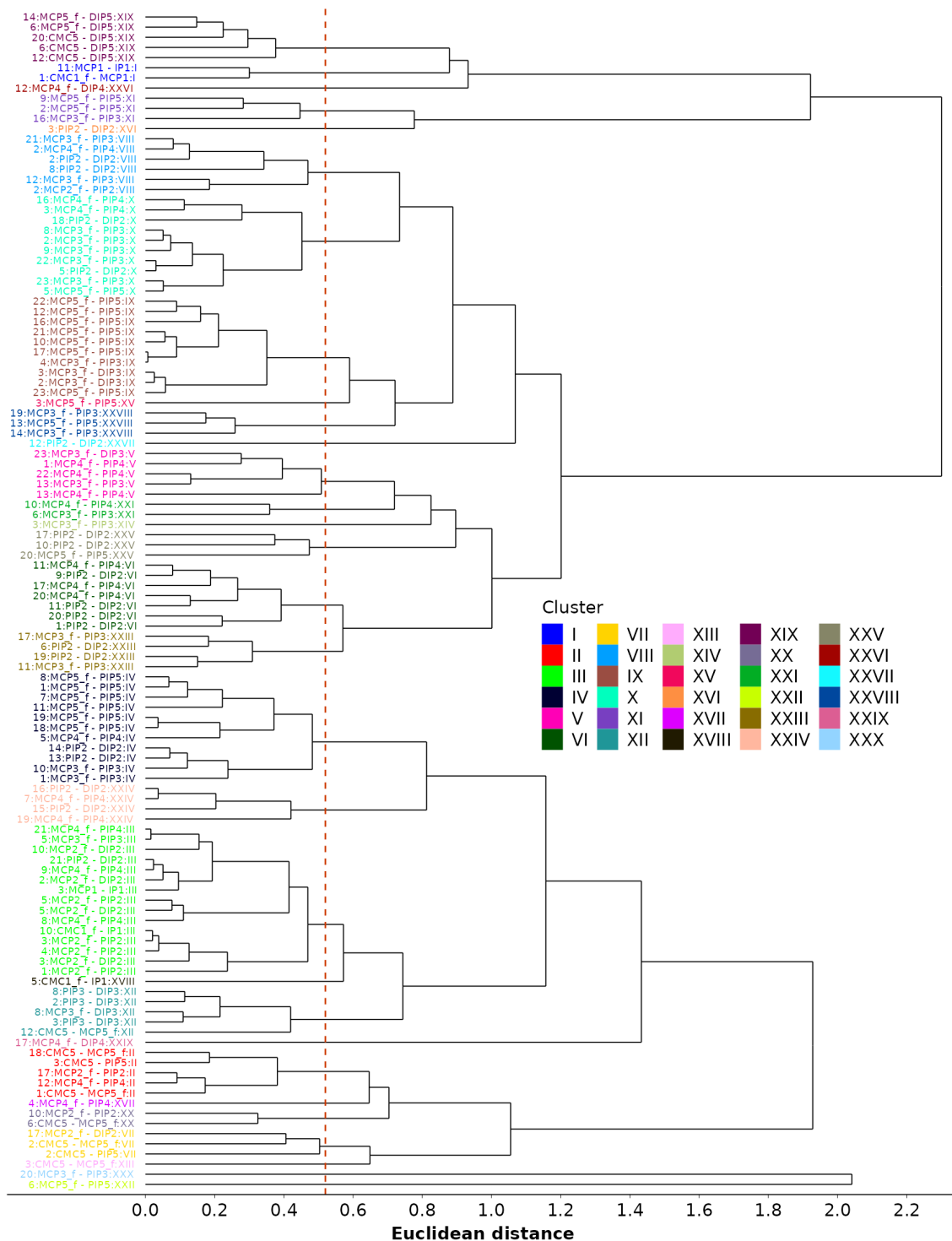


Figure 3.13 Agglomerative (hierarchical) clustering of models based on the similarity of standardized coefficients. The dendrogram shows 30 color-coded clusters obtained by cutting the tree at a distance of 0.52.

Table 3.5 DOF reductions across 23 grasps (functional movements) through intra-finger dependency modeling, showing remaining DOFs and model distribution across clusters.

Functional movement	DOF reductions	No. models per cluster	No. reduction models	DOFs remaining
3	11	3/III	9	5
2	10	2/VII, 2/VIII	8	6
1	7	2/IV	6	9
5	7	3/III, 2/X	4	9
10	7	2/III	6	9
12	7	–	7	9
17	7	–	7	9
6	6	2/XIX	5	10
8	6	2/XII	5	10
11	5	2/VI	4	11
20	5	2/VI	4	11
9	4	–	4	12
13	4	2/V	3	12
16	4	–	4	12
19	4	–	4	12
21	4	2/III	3	12
14	3	–	3	13
23	3	–	3	13
18	3	–	3	13
4	3	–	3	13
22	3	–	3	13
7	2	–	2	14
15	1	–	1	15

This chapter developed reduced kinematic models of human hand movements by analyzing grasp-oriented intra-finger dependencies using the largest publicly available multimodal database for hand movements, comprising synchronized joint angle values from 77 test subjects performing 23 ADL grasps. This methodology provides a foundation for simplifying the design of anthropomorphic devices while retaining functional accuracy.

Data preprocessing techniques were introduced to curate the dataset, isolating finger flexion/extension movements, discarding data outside the anatomical range, and excluding experiment runs with an insufficient ROM for proper inference and modeling. Through correlation analysis, 116 highly to very highly correlated dependency-movement relationships were identified across all grasps.

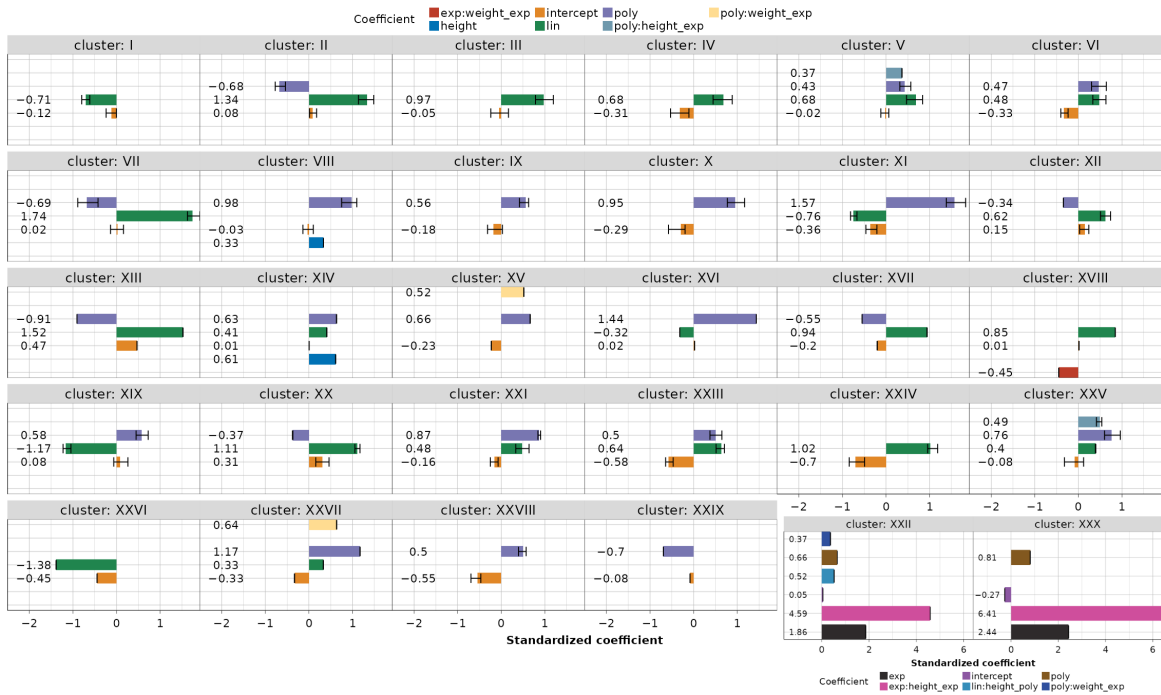


Figure 3.14 Clustered models with mean, minimum, and maximum coefficient values. The figure shows the estimated mean values of standardized coefficients for each cluster, along with the minimum and maximum values per cluster. Singular clusters containing only one model are also highlighted.

Using regularized GLM for uncorrelated predictor selection and weighted LME modeling, joint dependencies were modeled with error metrics on the test dataset: absolute wMAE values ranged from 2.4 to 16° (median 7.5°), and relative wWMAPE values ranged from 11 to 56.1% (median 27.9%). Clustering reduced 116 joint dependencies to 30 clustered models, enabling simplified implementation. We achieved DOF reductions during FE ranging from 1 to 11, with a median of 4.

While this study aimed to concisely present both the methodology and results for reducing grasp-oriented hand kinematic models, certain complex grasps—such as holding and cutting with a knife, turning a screwdriver, prismatic pinching, and parallel extension grasp—posed challenges for reduction, achieving DOF reductions of only 1 to 3. These challenges may stem from joints remaining static during such grasps or requiring alternative modeling approaches for further simplification.

Building on these kinematic reductions and methodologies, the next chapter transitions to the practical application of these findings in designing, simulating, and developing a soft-pneumatic rehabilitation glove.

Chapter 4

Design and Development of a Rehabilitation Glove: A Soft Robotics Approach

THIS chapter outlines the design, simulation, and development of a rehabilitation glove prototype powered by soft pneumatic actuators (SPAs) tailored for finger movement¹. Before detailing the glove's design, a geometric model of the finger is developed, using the index finger as a representative example. A functional forward kinematics model is introduced, along with both numerical and analytical approaches for solving the inverse kinematics of four human fingers, excluding the thumb.

Subsequently, a comprehensive kinematic analysis and activities of daily living (ADL) workspace study of anatomical fingers and their actuators informed the design and development of an innovative SPA. The ADL workspace represents the functional range of motion (ROM) required for performing everyday tasks such as grasping, reaching, and manipulating objects. The proposed actuator design combines cylindrical and ribbed geometries with a reinforcing element—a thicker, less extensible structure—resulting in an asymmetric cylindrical bellow actuator driven by positive pressure. The design process leverages a simplified model of human hand kinematics and its reachable workspace, which serves as the foundation for characterizing the SPAs. This characterization enabled the creation of a 3D-printed glove replicating the functional ROMs of human fingers.

¹This chapter builds upon the findings presented in Bazina et al. (2022) and further expands upon Bazina et al. (2024b).

The morphology of the SPA is derived from detailed analyses of human finger anatomy and motion, followed by the development of a segmented rigid-body kinematics model. These models approximate the soft segments using rigid links, allowing implementation within an open-source framework for robotic prototyping (ROS). The performance of the SPA is validated through numerical simulations under varying pressure levels using Finite Element Method (FEM) analysis, demonstrating strong alignment with human finger trajectories. To streamline an iterative design during the grasp-oriented development process, a modified pseudo-rigid-body (PRB) model is introduced, reducing computational complexity while maintaining minimal error.

The SPAs are fabricated using additive manufacturing techniques with thermoplastic polyurethane (TPU), which was selected for its flexibility and durability. The SPAs were then assembled into a prototype rehabilitation glove, which underwent ergonomic testing in interaction with a human hand. The evaluation confirmed the glove's suitability for practical rehabilitation applications, validating its design for supporting natural finger movements during therapy.

Contribution of this Chapter

The primary contribution of this chapter is the development of a methodology for designing functional, anatomically compatible, 3D-printed soft pneumatic actuators (SPAs) to facilitate the movements required by a rehabilitation glove. The design process begins with a comprehensive kinematic analysis of human hand motion during prismatic and circular grasping. This analysis simplifies the kinematic model while preserving the activities of daily living (ADL) workspace, which serves as the foundation for characterizing the SPAs and constructing a 3D glove model tailored for finger rehabilitation.

Additionally, a segmented rigid-body kinematic model is developed, effectively adapting traditional “rigid” robotics techniques to model soft robotic devices. Numerical simulations using the Finite Element Method (FEM) and modified pseudo-rigid-body (PRB) models are introduced to analyze and optimize actuator performance. The PRB model, in particular, plays a critical role in future design iterations and control system development due to its significantly lower computational complexity compared to FEM.

Limitation of the Study

It should be noted that, while the final outcome of this study is a functional soft rehabilitation glove, the kinematic analyses are focused solely on four human fingers, excluding the thumb. With its significantly different anatomical structure and functional role in grasping, the thumb requires a distinct modeling approach. As such, its inclusion has been left for future work to ensure a comprehensive and accurate representation of hand kinematics. Future research should aim to incorporate thumb kinematics to enhance the model's applicability for a wider range of rehabilitation scenarios and grasp types.

4.1 Soft Rehabilitation Gloves Design: State-of-the-Art

Robotic-assisted rehabilitation presents a promising solution by delivering effective therapy with reduced reliance on healthcare professionals (Colombo and Sanguineti, 2018). Despite its potential, challenges in the design and implementation of these systems remain and warrant further exploration. As discussed in Section 3, the intricate anatomy of the human hand, which comprises up to 25 degrees of freedom (DOF), enabling both power and precision grasping, underscores the need for advanced rehabilitation methods (Bazina et al., 2024c; Colombo and Sanguineti, 2018).

Soft robotic rehabilitation devices have emerged as a compelling alternative to traditional approaches, offering inherent safety, flexibility, and adaptability. Unlike traditional rigid robots, soft robotics provide a more natural interaction with the human hand, making them well-suited for personalized rehabilitation needs (Cappello et al., 2018; Chu and Patterson, 2018; Haggerty et al., 2023; Majidi, 2014; Rus and Tolley, 2015).

The effectiveness of such devices has been demonstrated, with studies showing significant benefits from using a soft robotic rehabilitation glove for patients with spinal cord injuries (Cappello et al., 2018). A similar approach is demonstrated in (Polygerinos et al., 2015), where a robotic glove was developed using SPAs made from composite tubular structures with anisotropic fiber reinforcements embedded in an elastomeric matrix. These actuators mimic finger movements through fluid pressurization, generating significant force when active and exhibiting low impedance when

inactive. Another example is a 3D-printed soft robotic hand exoskeleton with a fold-based actuator design, offering guidelines for fabrication and proposing future revisions to match better the ROMs of a healthy hand (Ang and Yeow, 2017). Similar studies have introduced and validated 3D-printed SPAs for glove rehabilitation devices (Heung et al., 2020; Mohammadi et al., 2018). A further research (Yi et al., 2017) developed a soft robotic glove with a high power-to-weight ratio and enhanced ergonomics, utilizing a bidirectional linear actuator and cable transmission for synchronized finger actuation. Young et al. (2024) present a novel soft robotic extensor inspired by spider legs, tailored for hand rehabilitation in stroke survivors. The device, which curves at rest and extends upon actuation, demonstrates significant potential for at-home rehabilitation by 3D-printed prototypes. While several designs—spanning cable-driven, pneumatic, and hydraulic actuators—have been proposed (Chu and Patterson, 2018), advancements in actuator design, safety, and implementation remain critical. Furthermore, while numerous designs have been proposed, as noted above, little attention has been given to leveraging the advantages of 3D printing technologies with soft materials. These technologies can potentially enable faster, more comfortable, and highly personalized production of rehabilitation devices.

This work aims to push the boundaries of 3D printing by integrating its capabilities with the benefits of soft robotics, paving the way for more adaptable and customized solutions.

4.2 Kinematics Characterization and Implementation of the Hand Model

Before the design and development of the soft rehabilitation glove, a comprehensive analysis of human hand kinematics is conducted. Traditional grasp classifications, as outlined by Cutkosky (1989), categorize movements into power and precision grasps, which can be further subdivided into circular and prismatic types (Jarque-Bou et al., 2019). The GRASP taxonomy (Feix et al., 2016) consolidates all previously defined grasp types from the literature, systematically organizing 33 distinct grasp types based on opposition type, virtual finger assignments, grasp type (power, precision, or intermediate), and thumb position. When focusing solely on hand configuration—excluding object shape and size—these 33 grasp types can be generalized into 17 broader categories.

In contrast to the methodology presented in Chapter 3, which includes 23 functional movements, this study simplifies the analysis by focusing exclusively on circular and prismatic grasps, specifically tailored for the development of a soft rehabilitation device. Previous research (Cobos et al., 2010) highlights subtle differences between these grasping types. To better capture these variations and improve modeling accuracy, this study employs distinct dependency equations.

Key simplifications include expressing joint dependencies linearly, with the metacarpophalangeal (MCP) joint serving as the primary reference. This approach is justified by the fact that the MCP joint, being the first joint in the kinematic chain with a large ROM, has the most significant influence on the overall hand posture. The dependency constraints are formulated as follows:

$$\theta_{\text{dependent}} = K \times \theta_{\text{parent}} + B \quad (4.1)$$

where $\theta_{\text{dependent}}/^\circ$ and $\theta_{\text{parent}}/^\circ$ represent the angular positions of the dependent and parent joints, respectively, with K and $B/^\circ$ being the slope and intercept. In most cases, the intercept is negligible, simplifying the dependency to a proportional relationship.

For circular and prismatic grasping, joint motions—such as flexion-extension (FE) and abduction-adduction (AA)—are modeled based on proportional dependencies, with specific scaling factors applied to MCP joint motion. The AA motions exhibit proportional relationships among fingers due to common tendons, while the palmar arc is represented through coupled carpometacarpal (CMC) joint movements. In prismatic grasps, slight modifications in joint flexion dependencies are required, particularly for the index fingers. For rehabilitation applications, inter-finger constraints account for involuntary flexion effects, where motion in one finger induces proportional movement in adjacent fingers. These relationships are linearized within the MCP joint’s range of motion. The simplified 9-DOF hand model effectively captures essential movement constraints while ensuring generalization across various grasp types and rehabilitation scenarios (Bazina et al., 2022; Cobos et al., 2010).

4.2.1 Geometric Model of Index Finger

Here, an example of the analysis of the kinematics of the I finger is introduced using a simplified geometric model defined by eight finger-specific parameters. The same

methodology can be extended to M, R, and L fingers, resulting in equivalent models with distinct parameter values.

According to Holzbaur et al. (2005), the neutral position of the finger is defined when the long axes of the phalangeal and metacarpal bones align. To fully capture finger motion in 3D space, joint centers must be precisely positioned, making the model highly complex. To simplify, approximation planes are introduced (Figure 4.1a), assuming that projecting rotational centers onto the FE plane does not significantly impact accuracy. The FE plane is defined by the CMC and fingertip (TIP) points, with its normal aligning with FE joint axes, while the AA plane is perpendicular to the FE plane.

The proposed kinematic model in Cobos et al. (2010) assumes complete straightness of the finger in all views, simplifying implementation but neglecting natural angular deviations. To address this, additional curvature is introduced by incorporating inclination angles $\beta_1, \beta_2, \beta_3$, and β_4 in the FE plane, as illustrated in Figure 4.1b. The segment lengths L_1, L_2, L_3 , and L_4 represent distances between joint centers.

For clarity, the previously established notation for the five joint parameters omits the index i for finger type. Finger curvature in the AA plane is considered negligible, as small inclination angles only slightly affect the distal DIP and PIP positions. The parameter values for the I finger, used for visual validation, are presented in Table 4.1. To generalize the model across individuals, phalange-to-hand length ratios proposed in Engelhardt et al. (2020) and Buryanov and Kotiuk (2010) are adopted, noting that they refer to phalange lengths rather than joint-to-joint distances.

Table 4.1 Finger-specific parameters for the index finger measured from the 50th percentile male model.

Finger parameters	L_1/cm	L_2/cm	L_3/cm	L_4/cm	$\beta_1/^\circ$	$\beta_2/^\circ$	$\beta_3/^\circ$	$\beta_4/^\circ$
Measured value	6.34	4.26	2.51	1.80	2	0	7	-3

4.2.2 Forward Kinematics – Modified Denavit-Hartenberg Convention

The forward kinematics solution calculates finger positions within the local coordinate system using three rotations and three translations. This requires known joint parameters: $\theta_{\text{CMC,FE}}, \theta_{\text{MCP,FE}}, \theta_{\text{MCP,AA}}, \theta_{\text{PIP,FE}}, \theta_{\text{DIP,FE}}$. To simplify the model, joints

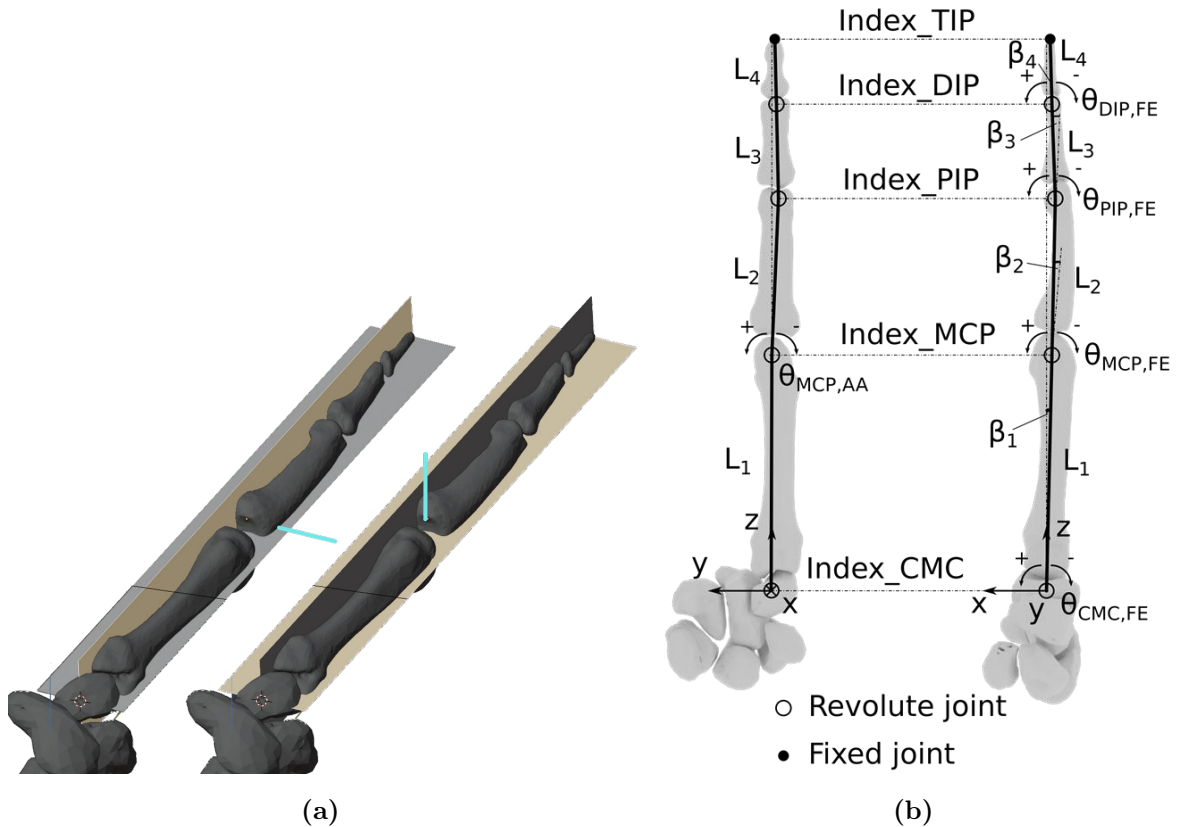


Figure 4.1 Index finger: (a) AA (left) and FE (right) approximation planes with their normals (light blue), (b) kinematic description in FE and AA approximation planes.

are treated as revolute, forming a kinematic chain with a revolute joint for the CMC FE, a universal joint for the MCP FE and AA, and two revolute joints for the PIP and DIP FE. To maintain a single degree of DOF per joint, the MCP universal joint is represented by two revolute joints, ensuring accurate kinematic representation.

Figure 4.2 illustrates the frames and parameters required to define the forward kinematics of the I, M, R, and L fingers. For clarity, the inclination angles β_i are exaggerated. The frames are assigned following the widely recognized modified Denavit-Hartenberg (DH) notation (Craig, 2014). The forward kinematics procedure is structured into three key steps:

1. Attaching coordinate frames to the finger links,
2. Determining the parameters of the four links, and
3. Deriving the homogeneous transformation matrix to represent the 6D position and orientation of the fingertip relative to the base coordinate system.

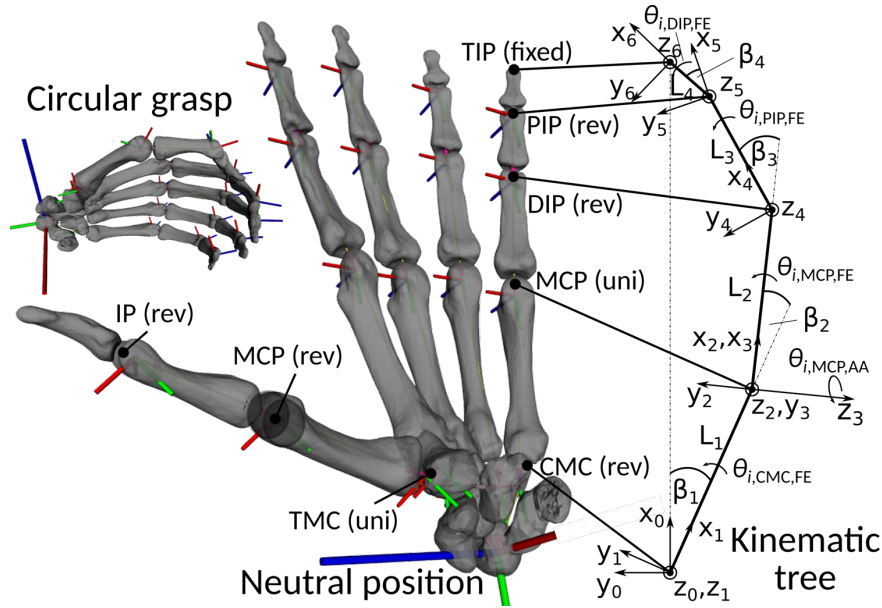


Figure 4.2 Modified DH forward kinematics convention for the I, M, R, and L fingers in the FE plane.

Since no prismatic joints are present in this finger representation, the DH procedure is explained based on an all-revolute configuration. The frames are assumed to be rigidly attached to the assigned links, ensuring that joint rotations result in identical shifts in the frame positions. The z_i -axis of each frame aligns with the axis of revolution of the i -th joint, following the attachment method described in Craig (2014):

1. Place the origin of the i -th frame at the intersection of two axes or where the common perpendicular meets the i -th axis.
2. Align the z_i axis along the i -th joint axis.
3. Point the x_i axis along the common perpendicular, or, if the axes intersect, make x_i perpendicular to the plane containing both axes.
4. Align frame 0 with frame 1 when the first joint parameter is zero.
5. For the n -th frame origin, select x_n arbitrarily to simplify joint parameters.

By attaching frames to the links, the modified DH parameters for the finger are defined as follows:

- α_{i-1} : Angle from z_{i-1} to z_i around x_{i-1} ,
- a_{i-1} : Distance from z_{i-1} to z_i along x_{i-1} ,
- d_i : Distance from x_{i-1} to x_i along z_i ,

– θ_i : Angle from x_{i-1} to x_i around z_i .

The general form of the general transformation matrix T_i^{i-1} , which consists of a 3×3 rotational matrix R_i^{i-1} and a 3×1 translation vector P_i^{i-1} , is obtained through two sequential transformations: translation along a_{i-1} and rotation about α_{i-1} , followed by translation along d_i and rotation about θ_i :

$$T_i^{i-1} = \begin{bmatrix} R_i^{i-1} & P_i^{i-1} \\ 0 & 0 & 0 & 1 \end{bmatrix} = \begin{bmatrix} c\theta_i & -s\theta_i & 0 & a_{i-1} \\ s\theta_i c\alpha_{i-1} & c\theta_i c\alpha_{i-1} & -s\alpha_{i-1} & -d_i s\alpha_{i-1} \\ s\theta_i s\alpha_{i-1} & c\theta_i s\alpha_{i-1} & c\alpha_{i-1} & d_i c\alpha_{i-1} \\ 0 & 0 & 0 & 1 \end{bmatrix} \quad (4.2)$$

where simplifying notation symbols are defined as follows:

$$\begin{aligned} c\theta_i &\implies \cos \theta_i, & s\theta_i &\implies \sin \theta_i & \forall i \in [1, 6], \\ c\alpha_{i-1} &\implies \cos \alpha_{i-1}, & s\alpha_{i-1} &\implies \sin \alpha_{i-1} & \forall i \in [1, 6]. \end{aligned} \quad (4.3)$$

Finally, the homogeneous transformation matrices can be obtained by substituting the modified DH parameters defined in Table 4.2 into the general transformation matrix (4.2).

Table 4.2 Modified DH parameters for a human finger.

Link	α_{i-1}	a_{i-1}	d_i	θ_i
1	0	0	0	$\theta_{\text{CMC,FE}} - \beta_1$
2	0	L_1	0	$\theta_{\text{MCP,FE}} - \beta_2$
3	$\pi/2$	0	0	$\theta_{\text{MCP,AA}}$
4	$-\pi/2$	L_2	0	$\theta_{\text{PIP,FE}} + \beta_3$
5	0	L_3	0	$\theta_{\text{DIP,FE}} + \beta_4$
6	0	L_4	0	0

Six resulting matrices ($T_1^0, T_2^1, T_3^2, T_4^3, T_5^4, T_6^5$) describe the transformations between neighboring frames according to Figure 4.2. The position and orientation of each frame with respect to the base frame are obtained through matrix multiplications.

To minimize human errors, these multiplications are automated, and the results are simplified using trigonometric relations with the symbolic mathematics library (Meurer et al., 2017), implemented in `Python`.

For the sake of simplicity, only the final homogeneous transformation matrix for the fingertip is presented here:

$$\begin{aligned}
T_6^0 &= T_1^0 T_2^1 T_3^2 T_4^3 T_5^4 T_6^5 \\
&= \begin{bmatrix} c_{12}c_3c_{45} - s_{12}s_{45} & -c_{12}c_3s_{45} - c_{45}s_{12} & -c_{12}s_3 & a_1c_1 + a_3c_{12}c_3 + a_4(c_{12}c_3c_4 - s_{12}s_4) + a_5(c_{12}c_3c_{45} - s_{12}s_{45}) \\ c_{12}s_{45} + c_3c_{45}s_{12} & c_{12}c_{45} - c_3s_{12}s_{45} & -s_{12}s_3 & a_1s_1 + a_3c_3s_{12} + a_4(c_{12}s_4 + c_3c_4s_{12}) + a_5(c_{12}s_{45} + c_3c_{45}s_{12}) \\ c_{45}s_3 & -s_3s_{45} & c_3 & s_3(a_3 + a_4c_4 + a_5c_{45}) \\ 0 & 0 & 0 & 1 \end{bmatrix} \tag{4.4}
\end{aligned}$$

Please note that the rehabilitation problem involves not only controlling the trajectory of the fingertip but also the motion of all joints. Therefore, the homogeneous transformation matrices for the MCP FE (T_2^0) and AA (T_3^0), as well as for the PIP (T_4^0) and DIP (T_5^0), are of significant importance.

All these matrices are available in the authors' GitHub repository².

4.2.3 Joint Dependency Effects on ROMs and Anatomical Limits

Incorporating joint dependency constraints into the human arm model affects ROMs, necessitating further evaluation to ensure compliance with anatomical joint limits. The ROM of each joint must remain within these limits during rehabilitation exercises, as exceeding them could lead to strain injuries and patient discomfort, making safety a top priority. The anatomical static joint ROMs used in this study are derived from previous research (Holzbaur et al., 2005; Kapandji, 2007).

Since the MCP joint serves as the parent for most dependencies, implementing MCP joint constraints indirectly determines the available ROMs for the proximal interphalangeal (PIP), distal interphalangeal (DIP), trapeziometacarpal (TMC), and interphalangeal (IP) joints. Consequently, the MCP ROMs must be restricted during FE movements, as shown in Table 4.3. During circular and prismatic grasps involving the index (I), middle (M), ring (R), and little (L) fingers, the MCP FE exhibits a lower bound deficit (LBD) of 20° in hyperextension to prevent PIP and DIP overextension. Full MCP flexion is permitted, resulting in an upper bound deficit (UBD) of 25° to 50° in the PIP and DIP ROMs.

²<https://github.com/tbazina/rehab/tree/master/kinematics/Hand9DOF/Index>

Table 4.3 Intra-joint FE dependency coefficients and ROMs.

Finger FE	Joint	K	$B/^\circ$	$LB/^\circ$	$UB/^\circ$	$LBD/^\circ$	$UBD/^\circ$
Circular I, M, R, L	MCP (parent)	–	–	–10	90	–20	–
	PIP (dependent)	0.75	0	–7.5	67.5	–	25
	DIP (dependent)	0.5	0	–5	45	–	35
Prismatic I, M	MCP (parent)	–	–	–10	90	–20	–
	PIP (dependent)	0.6	0	–6.6	60	–1	32.5
	DIP (dependent)	0.3	0	–3.3	30	–1.5	50

A comparison of inter-finger joint dependencies during AA, presented in Table 4.4, reveals significant reductions in ROMs, with lower and upper bound deficits of approximately 15° . These constraints prevent finger overlapping and allow for slight finger contact, which is typical during grasping. Finger overlapping can be further explored in individual finger training modes.

Table 4.4 Inter-finger AA dependency coefficients ROMs

Finger AA	K	$LB/^\circ$	$UB/^\circ$	$LBD/^\circ$	$UBD/^\circ$
I – MCP (parent)	–	–15	15	–15	15
M – MCP (dependent)	0.2	–3	3	–17	17
L – MCP (parent)	–	–15	15	–10	10
R – MCP (dependent)	0.5	–7.5	7.5	–15	15

The ROMs covered by the L, R, M, and I fingers during the palm’s arch-like motion are outlined in Table 4.5. During this motion, the little finger exhibits the largest ROM in CMC FE.

Table 4.5 Palmar arc chained dependency (CMC FE) coefficients and ROMs.

CMC FE	K	$LB/^\circ$	$UB/^\circ$	$LBD/^\circ$	$UBD/^\circ$
L (parent)	–	0	15	–	–
R (dependent, parent: L)	0.6	0	10	–	–
M (dependent, parent: R)	0.5	0	5	–	–
I (dependent, parent: M)	1.0	0	5	–	–

4.2.4 Inverse Kinematics Solvers

In robotic systems, forward kinematics provides only a partial solution, as it determines the position and orientation of the end-effector but not the required joint parameters. To achieve precise control, inverse kinematics (IK) is essential for determining the joint parameters $\theta_{\text{CMC,FE}}$, $\theta_{\text{MCP,FE}}$, $\theta_{\text{MCP,AA}}$, $\theta_{\text{PIP,FE}}$, $\theta_{\text{DIP,FE}}$ when the 6D position of the TIP is known. Thus, the inverse kinematics solvers, that leverage numerical and analytical approaches for accurate finger motion planning are introduced.

In both approaches, the process begins with the TIP position, which is represented by the transformation matrix (Bazina et al., 2022):

$$T_6^0 = \begin{bmatrix} R_6^0 & P_6^0 \\ 0 & 0 & 0 & 1 \end{bmatrix} = \begin{bmatrix} r_{11} & r_{12} & r_{13} & p_x \\ r_{21} & r_{22} & r_{23} & p_y \\ r_{31} & r_{32} & r_{33} & p_z \\ 0 & 0 & 0 & 1 \end{bmatrix} \quad (4.5)$$

Numerical Approach

To numerically solve the overdetermined nonlinear system with six equations and five unknowns, a custom `SymPy` script and the `SciPy` least-squares solver (Virtanen et al., 2020) are utilized. To simplify the problem and reduce the degrees of freedom (DOFs), dependency equations are introduced to link the DIP and PIP flexions to the MCP joint, incorporating the coefficients K_{PIP} and K_{DIP} into the transformation matrices.

The IK problem is tackled using the full transformation matrix and the position vector alone. The position vector approach enhances computational efficiency by reducing evaluations. Additionally, an analytical Jacobian matrix derived from the position vector minimizes numerical approximations, further improving speed. Symbolic differentiation of the position vector using DH parameters and dependency coefficients yields the Jacobian columns:

$$\frac{\partial P_6^0}{\partial \theta_{\text{MCP,AA}}}, \quad \frac{\partial P_6^0}{\partial \theta_{\text{MCP,FE}}}, \quad \frac{\partial P_6^0}{\partial \theta_{\text{CMC,FE}}} \quad (4.6)$$

Joint parameters are constrained by dependencies in Tables 4.3, 4.4 and 4.5, with an initial guess of 0° and a termination tolerance of 10^{-5} . The average execution time for the full transformation matrix approach is approximately 21 ms, while using the

position vector and analytical Jacobian reduces the time to 13 ms, achieving a 38 % speed improvement. These results align with literature benchmarks.

To validate the solvers, a grid of $40 \times 40 \times 40$ parameter values (64 000 total) is generated using $\theta_{\text{MCP,AA}}$, $\theta_{\text{MCP,FE}}$, and $\theta_{\text{CMC,FE}}$ with values constrained between the upper and lower bounds specified in Tables 4.3, 4.4, and 4.5. Forward kinematics, as defined by equation (4.4), is applied to the grid to compute the corresponding rotation matrices and position vectors. The accuracy of the inverse kinematics solver is then evaluated by testing its ability to reconstruct the correct input joint parameters θ_i given either the full transformation matrix or the position vector alone.

When tested using the full transformation matrix, the solver accurately reconstructed the input joint parameters in 100 % of cases, covering all 64 000 simulations. When tested using only the position vectors, the solver accurately reconstructed the input joint parameters in 98 % of cases. In the remaining 2 % of simulations, while the solver obtained valid θ_i values, they did not match the original input values used for generating the simulations. These discrepancies occurred near the finger's neutral position, where multiple possible solutions exist. In such cases, the solver returned one valid solution, even if it did not correspond to the original input parameters used for simulation generation.

Overall, the numerical IK solver demonstrates reliable performance for the I, M, R, and L fingers, confirming its validity and applicability in hand modeling.

Analytical Approach

In addition to the numerical approach described above, a closed-form set of equations can be employed to improve the efficiency of motion planning algorithms. The details of this approach are presented below. Initially, the overdetermined system, consisting of six equations and five unknowns, was addressed using the Inverse Kinematics Behavior Tree (IKBT) solver (Zhang and Hannaford, 2019); however, no solutions were obtained. Subsequently, a semi-automatic process utilizing a custom `SymPy` script was attempted.

To reduce the problem complexity and the number of DOFs, general dependency equations linking DIP and PIP FE to MCP FE are employed:

$$\begin{aligned}\theta_{\text{PIP,FE}} &= K_{\text{PIP}} \times \theta_{\text{MCP,FE}} \\ \theta_{\text{DIP,FE}} &= K_{\text{DIP}} \times \theta_{\text{MCP,FE}}\end{aligned}\tag{4.7}$$

By introducing (4.7) into the homogeneous matrix (4.4), the problem was redefined as an overdetermined system, where three unknown joint parameters— $\theta_{\text{CMC,FE}}$, $\theta_{\text{MCP,FE}}$, and $\theta_{\text{MCP,AA}}$ —are computed from six transformation matrix equations: three for rotation and three for position (Bazina et al., 2022).

Due to the transcendental nature of the equations containing complex trigonometric functions, a semi-automatic procedure is employed to introduce substitutions and manually select the solving order. The arccos function, commonly appearing in IK equations, returns values in the range 0 to 180°. However, all joint parameters are constrained to -10 to 90° per Table 4.3, Table 4.4 and Table 4.5. Thus, the following equations utilize the \pm arccos function to cover the range -180 to 180° , exploiting the even property of cosine.

The set of solutions for the $\theta_{\text{MCP,AA}}$ is trivially expressed as:

$$\theta_{\text{MCP,AA}} = \pm \arccos(r_{33}) \quad (4.8)$$

To solve the remaining two joint parameters, it is necessary to introduce the following simplifications and substitutions for composite angles:

$$u_{\text{MCP,PIP}} = K_{\text{PIP}}\theta_{\text{MCP,FE}} + 2\beta_3 \quad (4.9)$$

$$u_{\text{MCP,DIP,PIP}} = K_{\text{DIP}}\theta_{\text{MCP,FE}} + 2\beta_4 + u_{\text{MCP,PIP}} \quad (4.10)$$

$$u_{\text{CMC}} = \beta_1 - \theta_{\text{CMC,FE}} \quad (4.11)$$

$$u_{\text{CMC,MCP}} = \beta_2 + \theta_{\text{MCP,FE}} - u_{\text{CMC}} \quad (4.12)$$

$$r_s = 1 - r_{33}^2 \quad (4.13)$$

From the following two equations, $\theta_{\text{MCP,FE}}$ can be calculated:

$$r_{31} = \sqrt{1 - r_{33}^2} \cos(u_{\text{MCP,DIP,PIP}}) \quad (4.14)$$

$$p_z = L_4 r_{31} + \sqrt{1 - r_{33}^2} (L_2 + L_3 \cos(u_{\text{MCP,PIP}})) \quad (4.15)$$

The algebraic solutions for $\theta_{\text{MCP,FE}}$ are:

$$\theta_{\text{MCP,FE}} = \frac{-2\beta_3 \pm \arccos\left(\frac{-L_2\sqrt{r_s} - L_4r_{31} + p_z}{L_3\sqrt{r_s}}\right)}{K_{\text{PIP}}} \quad (4.16)$$

$$\theta_{\text{MCP,FE}} = \frac{-2\beta_4 \pm \arccos\left(\frac{r_{31}}{\sqrt{r_s}}\right) \mp \arccos\left(\frac{-L_2\sqrt{r_s} - L_4r_{31} + p_z}{L_3\sqrt{r_s}}\right)}{K_{\text{DIP}}} \quad (4.17)$$

$$\theta_{\text{MCP,FE}} = \frac{-2\beta_3 - 2\beta_4 \pm \arccos\left(\frac{r_{31}}{\sqrt{r_s}}\right)}{K_{\text{DIP}} + K_{\text{PIP}}} \quad (4.18)$$

$\theta_{\text{CMC,FE}}$ is determined from the following equations:

$$r_{13} = -\sqrt{1 - r_{33}^2} \cos(u_{\text{CMC,MCP}}) \quad (4.19)$$

$$p_y = \frac{-L_1\sqrt{1 - r_{33}^2} \sin(u_{\text{CMC}}) - L_4r_{13}\sqrt{\frac{r_{31}^2 + r_{33}^2 - 1}{r_{33}^2 - 1}} + p_zr_{33}\sqrt{\frac{-r_{13}^2 - r_{33}^2 + 1}{1 - r_{33}^2}}}{\sqrt{1 - r_{33}^2}} \\ - \frac{L_3r_{13}\sqrt{\frac{-L_2^2r_{33}^2 + L_2^2 + 2L_2L_4r_{31}\sqrt{1 - r_{33}^2} - 2L_2p_z\sqrt{1 - r_{33}^2} + L_3^2(r_{33}^2 - 1) + L_4^2r_{31}^2 - 2L_4p_zr_{31} + p_z^2}{L_2^2(r_{33}^2 - 1)}}}{\sqrt{1 - r_{33}^2}} \quad (4.20)$$

Three solutions can be obtained for $\theta_{\text{CMC,FE}}$ using (4.19) and (4.20):

$$\theta_{\text{CMC,FE}} = \beta_1 + \arcsin\left(\frac{L_3r_{13}\sqrt{\frac{r_s(L_3^2 - L_2^2) + 2L_2\sqrt{r_s}(p_z - L_4r_{31}) - L_4^2r_{31}^2 + 2L_4p_zr_{31} - p_z^2}{L_3^2r_s}}}{L_1\sqrt{r_s}}\right) \\ + \frac{L_4r_{13}\sqrt{\frac{-r_{31}^2 + r_s}{r_s}}}{L_1\sqrt{r_s}} + \frac{p_y\sqrt{r_s} - p_zr_{33}\sqrt{\frac{-r_{13}^2 + r_s}{r_s}}}{L_1\sqrt{r_s}} \quad (4.21)$$

$$\theta_{\text{CMC,FE}} = \beta_1 - \beta_2 - \theta_{\text{MCP,FE}} \pm \arccos\left(\frac{-r_{13}}{\sqrt{r_s}}\right) \quad (4.22)$$

Structured computation of multiple IK solutions:

1. Calculate both values of $\theta_{\text{MCP,AA}}$ via (4.8), and continue with the solutions in the range -15 to 15° ; if none exist, return no solution.

2. Calculate all eight possible solutions for $\theta_{\text{MCP,FE}}$ from (4.16)–(4.18) and consider those in range -10 to 90° ; if none exist, return no solution.
3. Compute three solutions for $\theta_{\text{CMC,FE}}$ from (4.21)–(4.22) and proceed based on the range in Table 4.5 for L, R, M, or I fingers; if none exist, return no solution.
4. Evaluate the TIP transformation matrix (4.4) for all valid combinations of $\theta_{\text{CMC,FE}}$, $\theta_{\text{MCP,FE}}$, and $\theta_{\text{MCP,AA}}$, and compare it with the initial matrix to validate the finger pose.

With a comprehensive analysis of human hand kinematics completed and its forward and inverse kinematics formulated, a strong foundation for understanding hand motion is established. Building on this groundwork, the kinematic characterization, morphology, and modeling of SPAs are performed to ensure that the actuator design aligns seamlessly with the natural movement of the human hand.

4.3 Kinematic Characterization, Morphology, and Modeling of SPAs

In this section, the kinematic characterization of a SPA is presented using a segmented rigid model approach—essentially a pseudo-rigid model with a rigid-link approximation of the soft structure for kinematic analysis. This characterization is performed using a modified Denavit-Hartenberg (DH) approach, as described in Section 4.2.2. The morphology and dimensioning of the finger actuators are then analyzed. These actuators are subsequently evaluated numerically using the Finite Element Method (FEM) to assess the workspace of the dimensioned fingers and deformations based on the input pressure. Finally, a pseudo-rigid body modeling (PRBM) approach is applied, which provides the key advantage of simplifying the complex, nonlinear deformations of SPAs into an equivalent system of rigid-body segments with localized compliance, enabling efficient analytical modeling while preserving essential deformation characteristics.

4.3.1 Kinematic Characterization Using Segmented Rigid Model Approach

The kinematic modeling of SPAs is performed based on Section 4.2, which provides a detailed kinematic analysis of an anthropometric hand model, incorporating inter-

and intra-joint constraints, and the implementation of this model in an open-source environment. The I, M, R, and L fingers are modeled as a single kinematic tree, each with unique parameters and constraints (see Figure 4.2). Joint parameters are determined using a modified DH approach, and a reachability analysis of the fingers' workspace is conducted. Figure 4.3a illustrates the kinematic trajectories of the anatomical joints of the index finger—CMC, MCP, PIP, DIP, and TIP—in the FE plane.

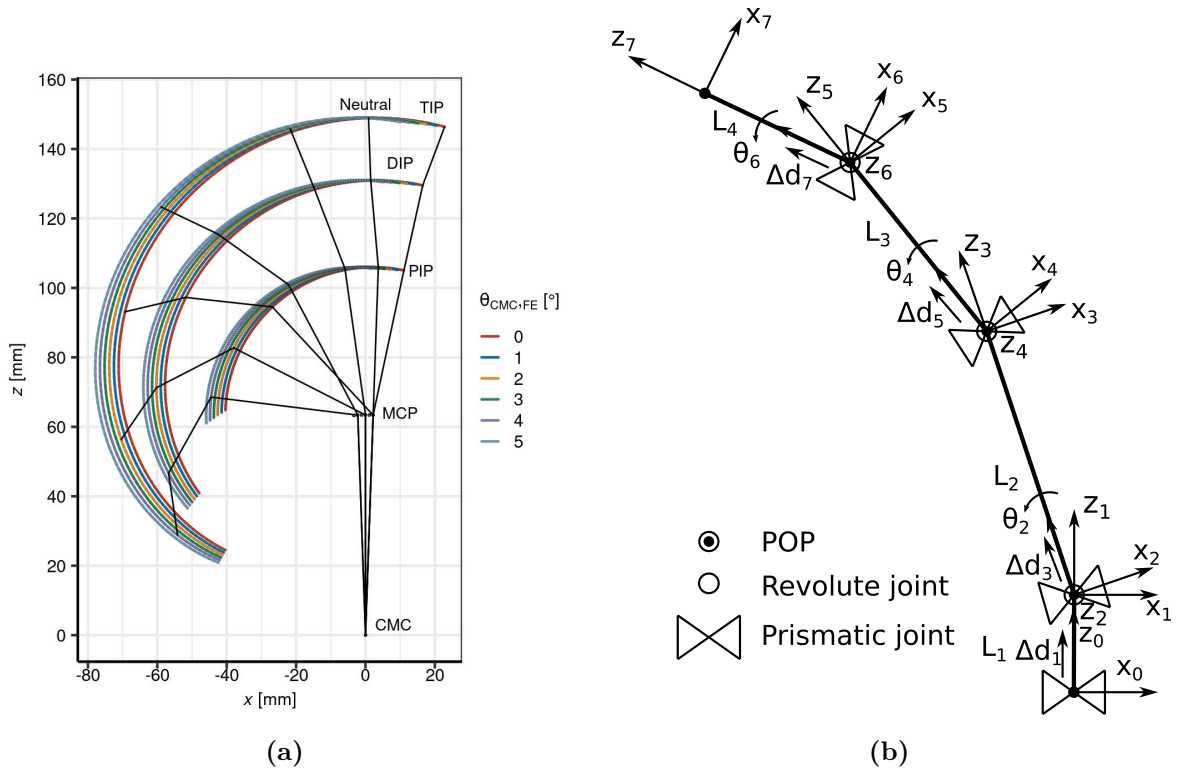


Figure 4.3 Kinematic analysis: (a) Workspace of the index finger in the FE plane, showing joint trajectories (MCP, PIP, DIP, TIP) during circular grasping as described in (Bazina et al., 2022); (b) Kinematic chain of the SPA using a modified DH approach. The diagram highlights revolute and prismatic joints along the actuator's segments, with symbols representing points of rotation (POP), revolute joints, and prismatic joints. Each joint is annotated with its corresponding DH parameters, including joint angle (θ_i) and elongation (Δd_i).

Based on the above-described analysis of human finger reachability, a segmented rigid model was devised to represent the kinematics of a compatible SPA (Armanini et al., 2023). In this approach, soft structures are modeled using rigid links connected by joints, where each joint provides one DOF to allow relative motion. This analysis incorporated revolute joints to represent rotational motion and prismatic joints to account for linear offsets.

The kinematics of the soft structures include three revolute joints, corresponding to the MCP, PIP, and DIP anatomical finger joints, and four additional prismatic joints to compensate for misalignments between the finger and actuator trajectories. Thus, each SPA consists of 7 DOFs. Using the modified DH convention described in Section 4.2.2, eight frames (0–7) were assigned to the links, spanning from the base to the SPA tip. Frames are rigidly attached to the links, and transformations between frames describe relative translations and rotations. The kinematic chain of the SPA is schematically shown in Figure 4.3b, with the y_i -axes omitted for brevity.

For revolute joints, the joint axis was defined as the axis of rotation, while for prismatic joints, it was the axis of translation. Joint parameters were represented as joint angles (θ_i) for revolute joints and link offsets (d_i) for prismatic joints. Frames were assigned to links for each axis pair ($i, i + 1$) following the steps presented in Section 4.2.2. The four DH parameters for the SPA are defined in Table 4.6.

Table 4.6 Modified DH parameters for SPA.

Link i	α_{i-1}	a_{i-1}	d_i	θ_i
1	0	0	$L_1 + \Delta d_1$	0
2	$\pi/2$	0	0	θ_2
3	$-\pi/2$	0	$L_2 + \Delta d_3$	0
4	$\pi/2$	0	0	θ_4
5	$-\pi/2$	0	$L_3 + \Delta d_5$	0
6	$\pi/2$	0	0	θ_6
7	$-\pi/2$	0	$L_4 + \Delta d_7$	0

As a last step in forward kinematics, homogeneous transformation matrices are used to describe the position and orientation of the actuator joints relative to the base frame (Frame 0). To fully define the 3D position and 3D orientation, a 6D transformation is employed. The general form of the transformation matrix between the $(i - 1)$ -th and i -th frame is given by Equation (4.2).

Using the DH parameters from Table 4.6, transformation matrices between each pair of neighboring frames ($T_1^0, T_2^1, T_3^2, T_4^3, T_5^4, T_6^5, T_7^6$) are calculated. The transformation matrix for the tip of the SPA, defining its position and orientation relative to the base frame (Frame 0), is obtained by multiplying all transformation matrices along the kinematic chain:

$$T_7^0 = T_1^0 T_2^1 T_3^2 T_4^3 T_5^4 T_6^5 T_7^6 = \begin{bmatrix} c\theta_{246} & 0 & -s\theta_{246} & -d_3 s\theta_2 - d_5 s\theta_{24} - d_7 s\theta_{246} \\ 0 & 1 & 0 & 0 \\ s\theta_{246} & 0 & c\theta_{246} & c\theta_2 d_3 + c\theta_{24} d_5 + c\theta_{246} d_7 + d_1 \\ 0 & 0 & 0 & 1 \end{bmatrix}, \quad (4.23)$$

where simplifying notation symbols are defined as follows:

$$\begin{aligned} c\theta_{24} &= \cos(\theta_2 + \theta_4), & c\theta_{246} &= \cos(\theta_2 + \theta_4 + \theta_6), \\ s\theta_{24} &= \sin(\theta_2 + \theta_4), & s\theta_{246} &= \sin(\theta_2 + \theta_4 + \theta_6). \end{aligned} \quad (4.24)$$

4.3.2 Finger SPA Specifications

After a detailed kinematic analysis of a SPA, based on the human hand's reachable workspace, the focus shifted to the design, dimensioning, and material selection of SPAs, utilizing pneumatic principles and 3D printing technology.

Dimensioning

The actuator design combines cylindrical and ribbed bellow geometries with intentionally introduced asymmetry through a reinforced structure to induce and control bending. The actuator features three ribbed bellow segments, corresponding to the MCP, PIP, and DIP joints of the finger. Pressurized air is delivered to each segment through three integrated cylindrical channels, each independently actuated to achieve precise motion control. To ensure ergonomic contact with the human hand, rounded grooves were incorporated on the contact surface between the actuator and the finger. Additionally, supporting elements were designed to secure the actuators in place, conform to the natural shape of the hand, and guide pneumatic tubing for seamless integration. The cross-sectional design and dimensions of the SPA are illustrated in Figure 4.4, while detailed measurements are provided in Table 4.7.

Material Selection

TPU (Thermoplastic Polyurethane) was selected for its exceptional flexibility and versatility. It is a widely used polymer in 3D printing, valued for its elasticity, shock absorption, and resistance to oil, grease, and abrasion. A key characteristic of TPU is its

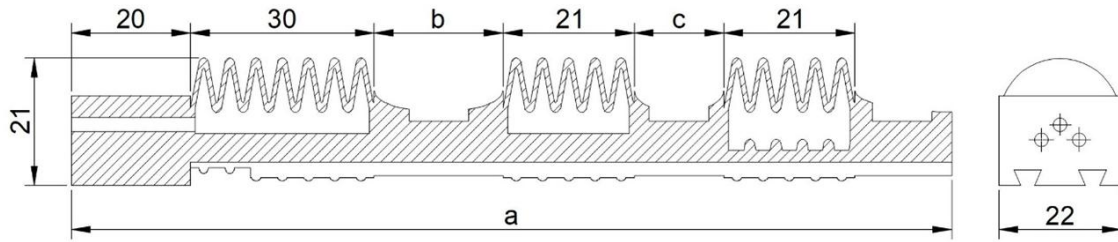


Figure 4.4 Cross-sectional design and dimensions of the SPA. The diagram illustrates key parameters: bellow lengths, connecting segment lengths (b , c), width, and overall actuator length (a).

Table 4.7 Dimensions of SPAs for different fingers.

Finger	Dimensions/mm			Number of ribs		
	a	b	c	MCP	PIP	DIP
Index	147	22	15	7	5	5
Middle	151	24	17	7	5	5
Ring	149	22	17	7	5	5
Little	135	19	13	7	5	4

ability to bend and stretch without breaking, exhibiting a stretchability of 300 to 600 %, meaning it can extend three to six times its original length before failure (Arifvianto et al., 2021). This makes TPU highly suitable for applications requiring a combination of durability and flexibility.

The Shore hardness of TPU (measured on the A scale) typically ranges from 60A (soft and silicone-like) to 95A (firm and nylon-like), providing a wide spectrum of mechanical properties. Its modulus of elasticity generally spans from 10 to 98 MPa (Ang and Yeow, 2017, 2020; Bhat et al., 2023), depending on its specific composition and structure (Bardin et al., 2020). For this study, TPU with a Shore hardness of 85A (AM, 2022) was selected for all subsequent analyses and prototype fabrication. This grade offers an optimal balance between flexibility, mechanical strength, and printability, making it ideal for the intended application (Curkovic and Cubric, 2021).

4.3.3 Finite Element Modeling

A simulation analysis was conducted under different pressure levels using the proposed SPA morphology. As an example, detailed studies of the index and little fingers were

performed, with simulations for the other fingers being analogous. The analyses were carried out using Abaqus Standard 2020 (Assistance, 2020) to model the mechanical behavior of the SPA using the finite element method (FEM). This assessment aimed at validating its functionality and determine the achievable bending angles.

The material properties of the structure were defined by specifying Young's modulus of 27 MPa (AM, 2022), corresponding to TPU 85A produced via the FDM method, and a Poisson's ratio of 0.36 (Haid et al., 2022). Based on the experimental observations in (Zhang et al., 2023), the TPU material demonstrates approximately linear elasticity for strains up to 20%. Beyond this limit, the material transitions into a nonlinear deformation phase characterized by a reduction in elastic modulus. Since the expected strain range for the SPA is within 20%, the material is modeled as linear elastic.

The dynamic implicit solver was utilized to capture the large deformations, incorporating geometric nonlinear effects accurately. The boundary conditions applied to the SPA are depicted in Figure 4.5.

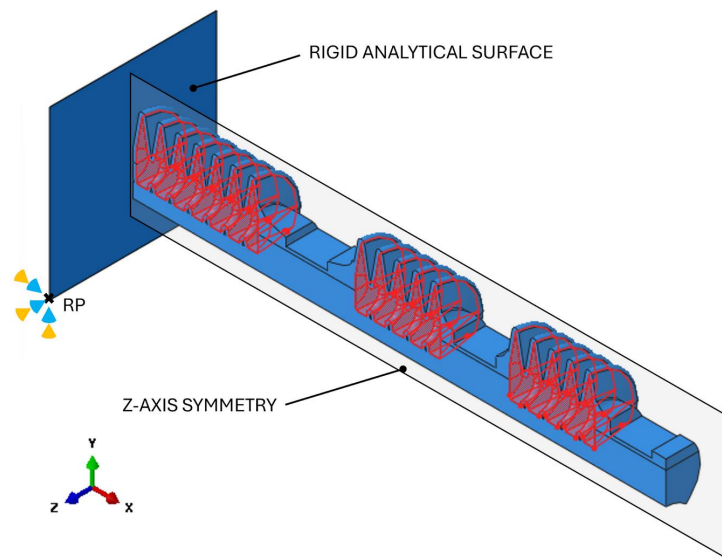


Figure 4.5 Boundary conditions applied to the SPA. The diagram illustrates key constraints and applied forces, defining the interaction between the actuator and its environment.

In the FEM model, the immovable starting section of the SPA, where the tubing connects, was removed. The zero point of the coordinate system was placed at the center axis of the first ribbed bellow, marking its starting point. The SPA was coupled to an analytical rigid surface using a tie constraint. All six degrees of freedom (three translational and three rotational) of the analytical rigid surface were fixed at

its reference point (denoted as RP in Figure 4.5). The tie constraint establishes a connection between the SPA and the analytical rigid surface, ensuring displacement compatibility between their surfaces. This effectively transfers motion and forces between the connected components, enabling them to behave as a unified structure. The analytical rigid surface was introduced to simplify the initial immobilized geometry of the SPA while providing a stable and consistent boundary condition for the attached actuator. This approach reduces computational complexity while maintaining accuracy in simulating interactions.

The pressure was applied to the inner surfaces of the bellows (highlighted as red ribbed bellows in Figure 4.5) and gradually increased in equal increments up to a maximum value of 0.3 MPa (3 bar), using a linear ramp function. The solver's initial increment was set to 0.001, with a minimum of 10^{-5} and a maximum of 0.01. This approach ensured a minimum of 100 simulation steps, linearly increasing the pressure.

Z-axis symmetry was applied to reduce computational time by utilizing the actuator's longitudinal symmetry plane (as shown in Figure 4.5). This approach allowed modeling only half of the actuator while applying symmetry boundary conditions. As a result, displacements perpendicular to the symmetry plane were constrained to zero, and rotations about axes within the plane (representing twisting and bending in the finger's AA direction) were also set to zero.

A hard contact condition, a constraint imposed to prevent penetration between two contacting surfaces, was applied in the direction normal to the outer surfaces of the ribbed bellows (highlighted in red in Figure 4.5). This condition ensures that the ribbed surfaces interact only when they come into contact, enabling forces to be transmitted in the direction normal to the contacting surfaces while preventing material overlap. Applying this constraint is crucial for accurately capturing the mechanical response during bellow inflation.

During inflation, internal pressure acts on the bellows, causing them to expand outward. This expansion results in contact between adjacent ribs, which subsequently induces bending in the SPA. The hard contact condition plays a vital role in modeling these interactions realistically by ensuring proper force transmission and deformation behavior. Additionally, the same contact condition was applied between the rigid analytical surface and the first rib of the bellow to simulate stable attachment and realistic boundary conditions.

The SPA was discretized using second-order tetrahedral elements (C3D10), which consist of 10 nodes (4 at the vertices and 6 at the midpoints of the edges) and employ quadratic interpolation of displacement. The additional mid-edge nodes enable these elements to capture complex deformation patterns more effectively. Combined with their quadratic shape functions, C3D10 elements can accurately represent curved surfaces, making them particularly useful for modeling bending in large deformation analyses. Compared to first-order tetrahedral elements (C3D4), second-order elements provide a more accurate approximation of stiffness by better capturing deformations. Additionally, computational efficiency can be improved because fewer second-order elements are required to achieve a similar level of accuracy. For instance, Pasvanti et al. (2019) demonstrated that second-order elements require 15 to 38 times fewer elements than first-order elements to achieve comparable results.

A global mesh seed of 0.8 mm was applied, while local seeds of 1.5 mm were used in the solid regions to reduce computational time. This approach provided a finer mesh around the bellows, where deformations are more prominent while maintaining a slightly coarser mesh in the solid regions (across the connecting rods), which experience minimal deformation, as illustrated in Figure 4.6. As a result, the final mesh consisted of 127 218 elements and 214 890 nodes.

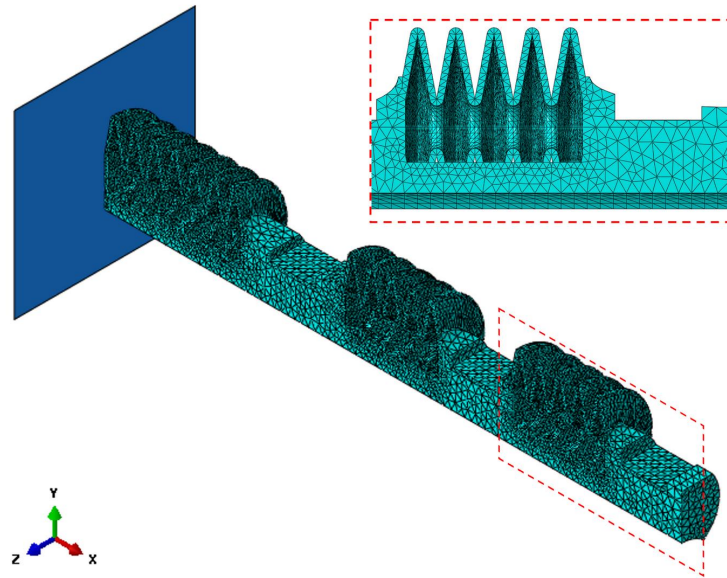


Figure 4.6 Discretized SPA with C3D10 elements and a mesh detail.

Displacements along the x- and y-axes were recorded at 10 specific points on the actuator: the start, middle, and end points of each bellow (corresponding to the MCP, PIP, and DIP joints) and the tip of the actuator (TIP point). As illustrated in Figure 4.7, these displacements were tracked at pressure increments of 0.01 MPa.

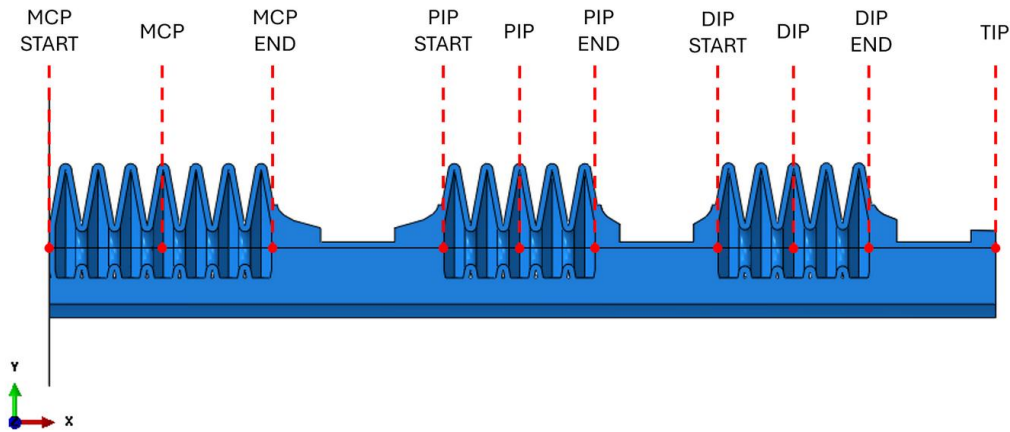


Figure 4.7 MCP, DIP, PIP, and TIP location points. The figure illustrates the measurement points along the SPA, including key joint locations used for displacement tracking.

Using the proposed FEM model, the functionality of the SPA was validated through simulations by analyzing angular movements under varying pressure levels. Images were recorded to evaluate the performance of the actuators for both the I and L fingers. Figure 4.8a illustrates the FEM analysis results for the bending motion of the index finger actuator at pressure levels ranging from 0 to 3 bar. Similarly, Figure 4.8b presents the corresponding results for the little finger actuator over the same pressure range.

The simulations reveal that the bending motion of the finger actuators occurs predominantly in the ribbed bellows, closely mimicking the smooth and controlled natural bending motion of a human finger. Additionally, while the bellows exhibit consistent bending behavior, the connecting rods play a critical role in maintaining and defining the inter-joint distances.

The planar angular motion of ribbed bellow SPA for the I and L fingers in the flexion-extension (FE) plane under varying pressure levels is illustrated in Figures 4.9a and 4.9b, respectively. The simulations demonstrate the actuator's bending behavior, explicitly highlighting the MCP, PIP, and DIP bellows and the TIP position. The starting point, midpoint, and endpoint deflections for each segment are represented by the respective

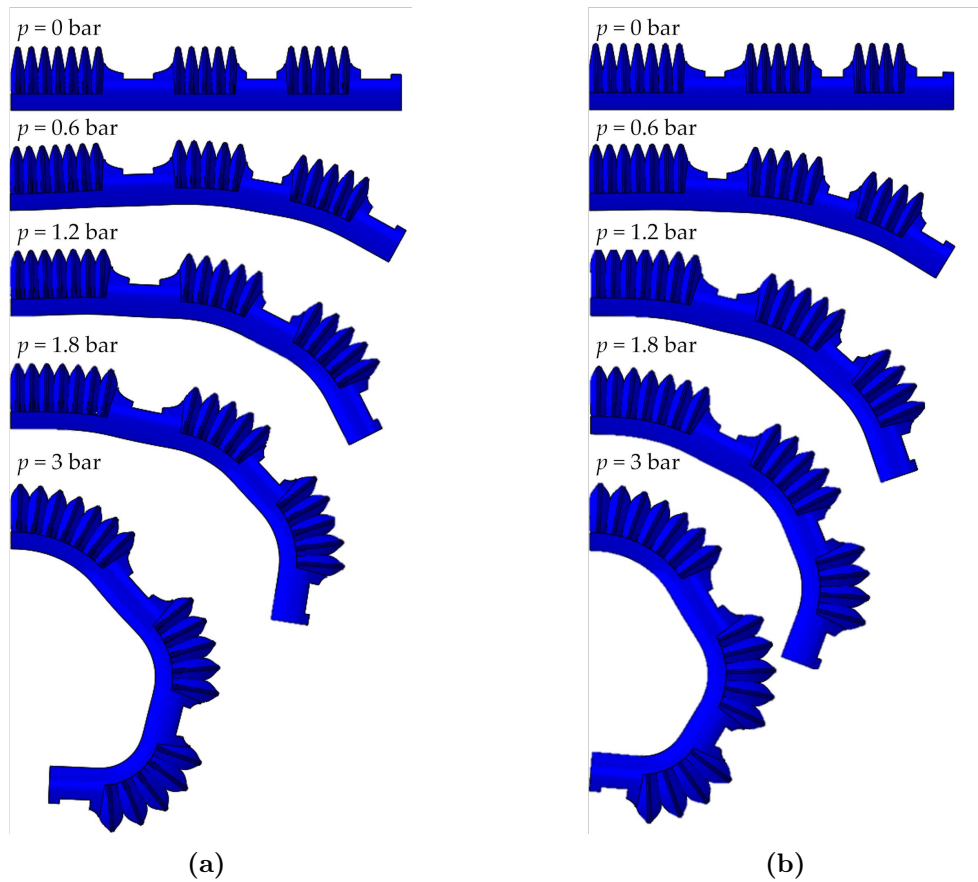


Figure 4.8 FEM analyses demonstrating angular motion of SPAs under varying pressure levels (0, 0.6, 1.2, 1.8 and 3 bar): (a) SPA for the index finger and (b) SPA for the little finger.

(x , y) coordinates. The bending of each bellow is approximated by using a three-point circular arc defined by these points, while the connecting rods are modeled as straight lines. This visualization provides an accurate geometric representation of the actuator's motion, highlighting smooth transitions between bellow segments and connecting rods. By visually comparing the position diagrams of the SPA (Figure 4.9a) and the human finger model workspace (Figure 4.3a), it can be observed that both exhibit a similar form during bending. This similarity highlights the actuator's potential effectiveness in rehabilitation applications, as it closely replicates the natural bending behavior of the finger, enabling functional support during therapy. This geometric representation will also be utilized in Subsection 4.3.4 to extract the necessary dimensions for further analyses.

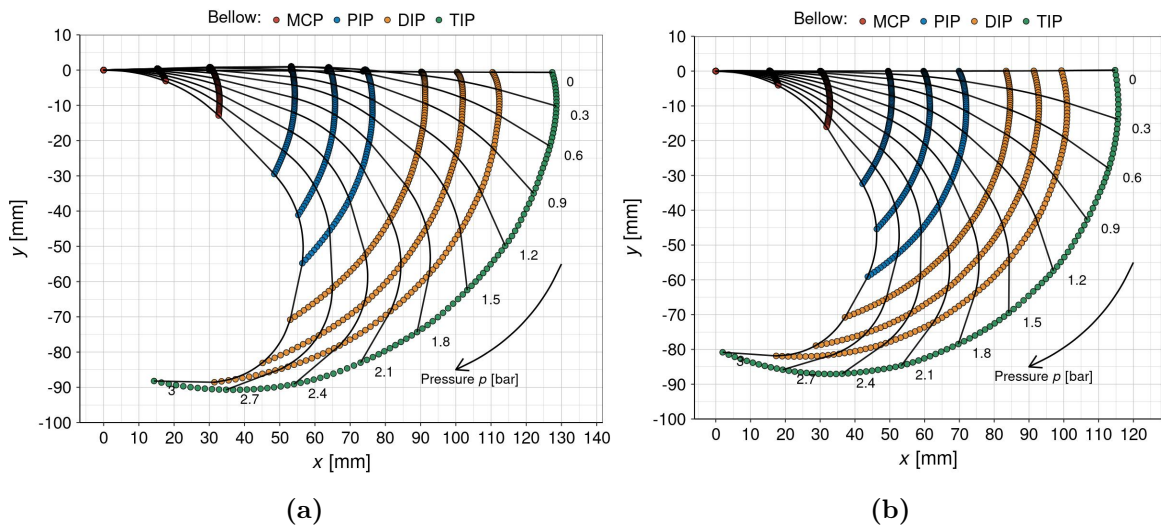


Figure 4.9 FEM simulation of a ribbed bellow SPA bending from 0 to 3 bar. The flexion-extension plane is shown with the (x, y) coordinates of each bellow segment’s start, mid, and endpoints. All three bellows—MCP, PIP, and DIP—are shown, along with the TIP. Each bellow’s bending is approximated using a 3-point circular arc: (a) SPA for the index finger and (b) SPA for the little finger.

Connecting Rod Compression Analysis

The compression of the rods connecting neighboring bellows (see Figure 4.4) was also analyzed. The inter-joint distances are at their maximum length at the start of bending. Due to forces acting on both ends (MCP—PIP and PIP—DIP connecting rods) or on one end (DIP—TIP connecting rod), these distances experience slight compression during actuation. To quantify compressive deformations, the inter-joint lengths were recorded at their maximum (initial) and minimum values (at 3 bar). The length range (maximum minus minimum) and the range-to-maximum compression ratio, expressed as a percentage, were calculated and are reported in Table 4.8. The range-to-maximum compression ratios for the I and L fingers are similar and remain below 1.77% for MCP—PIP and PIP—DIP and below 0.63% for DIP—TIP connecting rods. Results indicate negligible compressive deformation, so the initial maximum values will be used in the modeling approach described in subsection 4.3.4. These values correspond to straight connecting rods at an initial pressure of 0 bar, as shown in Figure 4.9.

Table 4.8 Compression of inter-joint distances for the index and little fingers.

Finger	Joints	Max/mm	Min/mm	Range/mm	Range_ratio/%
Index	MCP—PIP	23.27	22.86	0.41	1.741
	PIP—DIP	16.60	16.32	0.28	1.675
	DIP—TIP	17.05	16.95	0.10	0.569
Little	MCP—PIP	19.57	19.31	0.26	1.34
	PIP—DIP	13.61	13.37	0.24	1.77
	DIP—TIP	15.42	15.32	0.10	0.63

Regression Analysis

From the FEM experimental data, the bending end angles ϑ_i and segment elongations $\Delta L_{\text{total},i}$ were obtained for each of the MCP, PIP, and DIP ribbed bellow segments. The elongations of each segment were calculated along a fitted 3-point arc (see Figure 4.9). A regression analysis was conducted to evaluate the relationship between the bending end angles ϑ_i , link elongations $\Delta L_{\text{total},i}$, and pressure p_{seg} across all three bellow actuator segments for both the index and little fingers. Figures 4.10a and 4.10b display the data alongside the corresponding regression lines for the index finger (red line) and the little finger (blue line). The relationships appear functionally similar, so the same model will be applied to both cases. A certain degree of nonlinearity is evident; therefore, in addition to the linear pressure term, a quadratic pressure term (without an intercept) was included to obtain a more accurate model:

$$\vartheta_i = K_{\vartheta 1,i} \times p_{\text{seg}} + K_{\vartheta 2,i} \times p_{\text{seg}}^2 \quad \forall i \in \{\text{MCP, PIP, DIP}\}, \quad (4.25)$$

$$\Delta L_{\text{total},i} = K_{L1,i} \times p_{\text{seg}} + K_{L2,i} \times p_{\text{seg}}^2 \quad \forall i \in \{\text{MCP, PIP, DIP}\}. \quad (4.26)$$

The coefficients from angle-pressure (4.25) and elongation-pressure (4.26) regression equations for the I and L fingers, along with their goodness-of-fit indicators, are presented in Table 4.9. The coefficients of determination indicate a strong positive relationship (adjusted $R^2 \approx 1$ in all cases) between pressure and bending angle as well as between pressure and joint elongation, consistent with guidelines for interpreting correlation coefficients (Mukaka, 2012). The minimal residual errors, ranging from 0.147 to 0.225° for bending angles and 0.0258 to 0.0709 mm for elongation, indicate that the model effectively captures the compliant behavior of the SPAs. It can also be observed that the linear term exceeds the quadratic term during the bending and

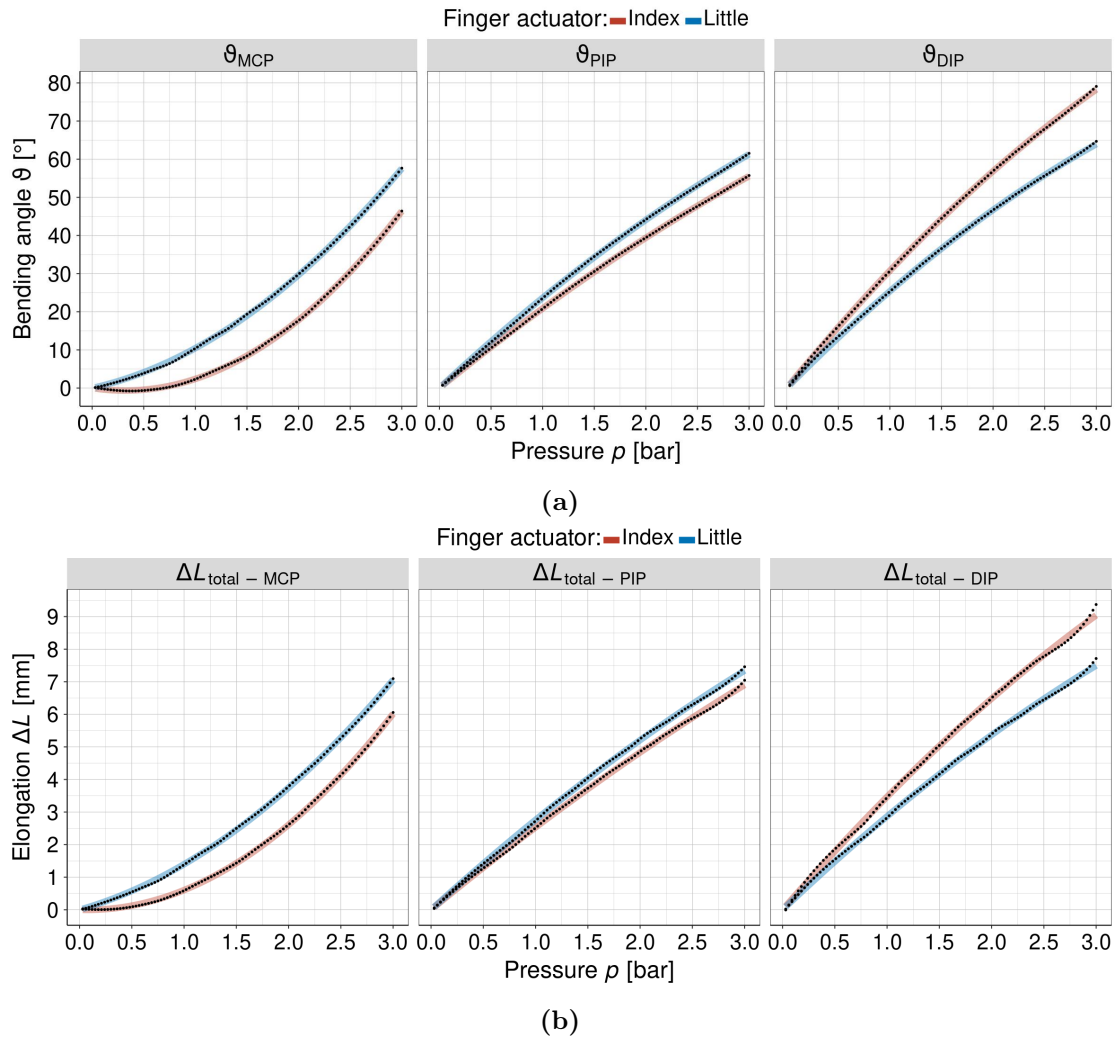


Figure 4.10 FEM obtained linear regression of joint constraints for the index and little fingers depending on pressure: (a) beam end angle vs. pressure, and (b) link offset vs. pressure.

elongation of both the PIP and DIP joints. However, this is not the case for the MCP joint, where the quadratic term becomes more significant, indicating more substantial nonlinearities.

In the following section, the potential of utilizing and adapting the pseudo-rigid body (PRB) model (Howell, 2001; Howell et al., 2013) is explored to approximate the motion trajectories of the entire SPA.

The geometric nonlinearities outlined above (see Table 4.9) and the significant elongations observed during bending indicate that modifications to the PRB model are required, as presented in the following Subsection 4.3.4.

Table 4.9 Linear regression coefficients for joint angles (ϑ) and link elongations (ΔL_{total}) for the index and little fingers.

Finger	Coefficient \ Joint	ϑ_{MCP}	ϑ_{PIP}	ϑ_{DIP}	$\Delta L_{\text{total,MCP}}$	$\Delta L_{\text{total,PIP}}$	$\Delta L_{\text{total,DIP}}$
Index	$K_{\vartheta 1,i}/^\circ \text{ bar}^{-1}$	-4.14	22.05	33.09	-	-	-
	$K_{\vartheta 2,i}/^\circ \text{ bar}^{-2}$	6.53	-1.18	-2.33	-	-	-
	$K_{L1,i}/\text{mm bar}^{-1}$	-	-	-	-0.097	2.644	3.697
	$K_{L2,i}/\text{mm bar}^{-2}$	-	-	-	0.701	-0.114	-0.228
	Adjusted R^2	0.9999	1	1	0.9999	0.9999	0.9998
	Residual SE/ $^\circ$ or mm	0.160	0.147	0.207	0.0258	0.0367	0.0709
Little	$K_{\vartheta 1,i}/^\circ \text{ bar}^{-1}$	6.10	25.27	27.43	-	-	-
	$K_{\vartheta 2,i}/^\circ \text{ bar}^{-2}$	4.36	-1.61	-2.04	-	-	-
	$K_{L1,i}/\text{mm bar}^{-1}$	-	-	-	0.920	2.918	3.051
	$K_{L2,i}/\text{mm bar}^{-2}$	-	-	-	0.477	-0.157	-0.184
	Adjusted R^2	0.9999	1	1	0.9999	0.9999	0.9999
	Residual SE/ $^\circ$ or mm	0.225	0.150	0.200	0.0308	0.0327	0.0468

4.3.4 Pseudo Rigid Body Modeling Approach

Building on the previous conclusion, the bending behavior of the bellows can be effectively analyzed using three-point arc approximations, enabling the possibility of modeling the entire motion analytically. To achieve this, the pseudo-rigid-body (PRB) modeling approach was modified to approximate the bending of each individual bellow segment. The PRB model is an approximation technique that represents compliant structures as a system of rigid bodies connected by joints with spring elements, effectively translating complex deformation behavior into simpler rigid-body kinematics. The results from these segment-level models were subsequently integrated to represent the overall behavior of the entire system. Before presenting the PRB formulation, it is essential to approximate the moments and forces acting on each ribbed bellow segment to ensure successful implementation. These approximations enable the PRB model to represent the system's kinematics accurately and allow for realistic deformation modeling under actuation.

Analytical Approximation of the Moment

First, the moment $M_{\text{seg}}/\text{N m}$ acting on a ribbed segment is determined, caused by an internal pressure p_{seg}/Pa with $n_{\text{r,seg}}$ ribs (Figure 4.11a). Each rib is approximated as a 180-degree semi-annulus with an outer radius R_{seg}/m and an inner radius r_{seg}/m (Figure 4.11b). The reference point for measuring R_{seg} and r_{seg} is positioned at the top surface of the reinforcing element. Although the approximation (red line) appears

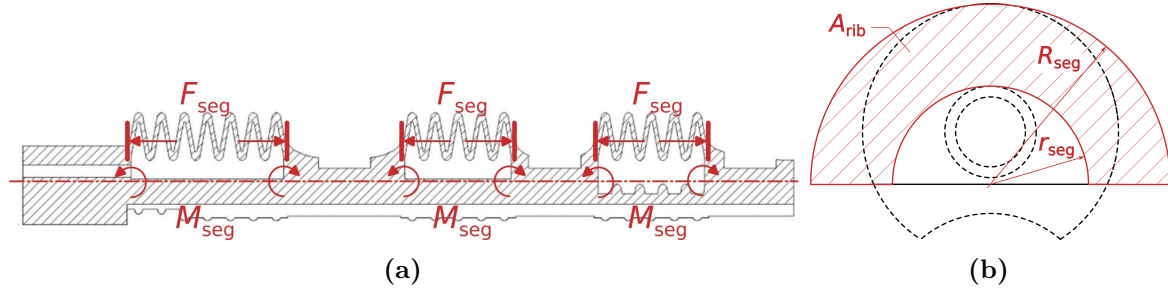


Figure 4.11 (a) Forces (F_{seg}) and moments (M_{seg}) acting on individual segments due to the pressurization of bellows in a SPA. (b) Approximation of the projected surface of a single bellow segment rib A_{rib} for computing forces and moments. The inner (r_{seg}) and outer (R_{seg}) diameters define the geometry. The black dashed line denotes the exact curved surface, while the red line represents the approximation.

visually distinct from the exact profile (black dashed line), the difference in the enclosed areas is small, as confirmed by measuring the surface from the actual model. This validates the approximation for practical purposes, such as force and moment calculation. To compute M_{seg} , the following procedure is applied:

1. *Determine the differential moment:* The moment due to pressure on a differential area element of the rib is calculated by integrating the pressure over the area, multiplied by the distance from the point of application to the axis (diameter of the semicircle). Using polar coordinates, the differential area element dA_{rib} of a single rib is:

$$dA_{\text{rib}} = r \, d\theta \, dr \quad (4.27)$$

The pressure p_{seg} acts normal to the surface and produces differential acting force dF_{rib} :

$$dF_{\text{rib}} = p_{\text{seg}} \, dA_{\text{rib}} = p_{\text{seg}} \, r \, d\theta \, dr \quad (4.28)$$

The moment arm for each point is the distance $r \sin \theta$, resulting in the differential moment dM_{seg} :

$$dM_{\text{seg}} = dF_{\text{seg}} \, r \sin \theta = p_{\text{seg}} \, dA_{\text{rib}} \, r \sin \theta = p \cdot r^2 \sin \theta \, d\theta \, dr \quad (4.29)$$

2. *Integrate over the semicircular annulus:* Integrate over the angle θ from 0 to π :

$$\int_0^\pi \sin \theta \, d\theta = 2 \quad (4.30)$$

Integrate over the radius r from r_{seg} to R_{seg} :

$$\int_{r_{\text{seg}}}^{R_{\text{seg}}} r^2 dr = \frac{R_{\text{seg}}^3 - r_{\text{seg}}^3}{3} \quad (4.31)$$

3. *Compute the moment per rib:*

$$M_{\text{rib}} = p_{\text{seg}} \cdot 2 \cdot \frac{R_{\text{seg}}^3 - r_{\text{seg}}^3}{3} = \frac{2}{3} p_{\text{seg}} (R_{\text{seg}}^3 - r_{\text{seg}}^3) \quad (4.32)$$

4. *Finally, the total moment* is given by multiplying Equation 4.32 by the number of ribs:

$$M_{\text{seg}} = \frac{2}{3} n_{\text{r,seg}} p (R_{\text{seg}}^3 - r_{\text{seg}}^3) \quad (4.33)$$

Each ribbed structure experiences a localized moment M_{seg} , while the radial expansion of the bellows is neglected. The net moment would be zero for a full circular bellow (360°) due to radial symmetry, and the bellow would only expand axially under pressure. However, for a semicircular bellow, the non-symmetric pressure distribution generates a moment. The formula for the moment scales linearly with the number of ribs $n_{\text{r,seg}}$, under the assumption that all ribs are identical and subjected to uniform internal pressure.

Analytical Approximation of the Tension Force

In this step, the tension force F_{seg}/N in a hollow 180-degree semi-annular structure with $n_{\text{r,seg}}$ ribs, subjected to an internal pressure p_{seg} , is approximated (see Figure 4.11a). The derivation follows the procedure:

1. *Projected area of a single rib:*

The projected area of a single rib, modeled as a 180-degree semi-annulus (see Figure 4.11b), is:

$$A_{\text{rib}} = \frac{\pi}{2} (R_{\text{seg}}^2 - r_{\text{seg}}^2) \quad (4.34)$$

2. *Sum of projected areas across ribs for a segment:*

For $n_{\text{r,seg}}$ identical ribs, the total area is:

$$A_{\text{seg}} = n_{\text{r,seg}} \cdot A_{\text{rib}} = n_{\text{r,seg}} \cdot \frac{\pi}{2} (R_{\text{seg}}^2 - r_{\text{seg}}^2) \quad (4.35)$$

3. Total segment tension force:

The tension force is the product of the internal pressure p_{seg} and the total projected area:

$$F_{\text{seg}} = p_{\text{seg}} \cdot A_{\text{seg}} = \frac{\pi}{2} n_{\text{r,seg}} p_{\text{seg}} (R_{\text{seg}}^2 - r_{\text{seg}}^2) \quad (4.36)$$

A few key assumptions are considered:

- The formula assumes that each rib is subjected to uniform internal pressure p_{seg} .
- The area of each rib is calculated based on the geometry of a 180-degree semi-annulus.
- The total tension force scales linearly with the number of ribs ($n_{\text{r,seg}}$).
- This tension force acts axially along the symmetry axis of the bellows structure.

Bending Stiffness of a Bellow Structure

The relationship between the applied moment, material properties, and geometry is examined to approximate the bending stiffness $K_{\text{seg}}/\text{N m rad}^{-1}$ of each bellow structure using the derived moment M_{seg} , as given by (4.33). The bending stiffness is expressed as:

$$K_{\text{seg}} = \frac{EI_{\text{total}}}{L_{\text{seg}}}, \quad (4.37)$$

where E/Pa is Young's modulus, $I_{\text{total}}/\text{m}^4$ is the total second moment of area of the cross-section, and L_{seg}/m is the length of the bellow (see Figure 4.4).

For the calculation of the moment M_{seg} , the projected area of the semi-annulus subjected to pressure is considered (Figure 4.11b). In contrast, the calculation of the second moment of area I_{total} requires accounting for the entire cross-section, including the reinforcement in the form of a rectangular base (Figure 4.12). Due to the ribbed surface of the bellows, the cross-section varies along its length, with the outer diameter ranging between r_{b} and R_{b} . To address this variation, a radius mixing parameter λ is introduced to compute an equivalent radius $R_{\text{b,eq}}$ for approximating the second moment of area. The value of this parameter will be determined through a subsequent optimization procedure. The outer radius, R_{b} , and inner radius, r_{b} , differ from R_{seg} and r_{seg} in that they represent half of the actual outer and inner diameters of the bellow. Conversely, R_{seg} and r_{seg} are measured from the top surface of the reinforcing structure to provide a more accurate approximation of the projected surface.

The process is composed of the following steps:

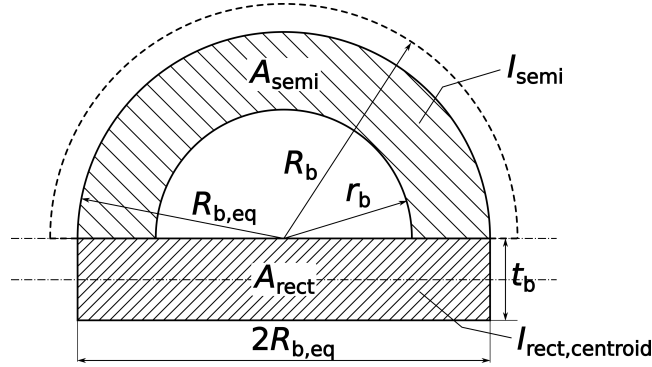


Figure 4.12 Approximation of the rib cross-section relevant for the second moment of area I_{total} computation. The cross-sectional area consists of a hollow semi-annulus and a rectangular thickening element. The hollow semi-annulus is defined by the inner radius r_b and the outer equivalent radius $R_{b,eq}$, which compensates for the ribbed bellow shape. The thickening element is a rectangle with sides $R_{b,eq}$ and t_b . The axes for computing the total second moment of area are indicated, along with the second moments of area of the individual components: I_{semi} for the semi-annulus and I_{rect} for the rectangular element.

1. *Equivalent radius calculation*: The equivalent outer radius $R_{b,eq}$ is calculated using the blending parameter λ :

$$R_{b,eq} = \lambda R_b + (1 - \lambda)r_b \quad (4.38)$$

where R_b is the outer radius and r_b is the inner radius (see Figure 4.12).

2. *Second moment of area calculation*: The cross-section consists of two components:
 1. Hollow Semicircular Annulus; and
 2. Rectangular Base.

Component 1: hollow semicircular annulus (outer radius $R_{b,eq}$, inner radius r_b).

The area A_{semi} of the hollow semicircular annulus is given by:

$$A_{semi} = \frac{\pi}{2} (R_{b,eq}^2 - r_b^2), \quad (4.39)$$

while the second moment of area about the base (neutral axis) is given as:

$$I_{semi} = \frac{\pi}{8} (R_{b,eq}^4 - r_b^4) \quad (4.40)$$

Component 2: Rectangular base (width $2R_{b,eq}$, rectangular support (base) thickness t_b).

Second moment of area about its own centroid is calculated as:

$$I_{\text{rect,centroid}} = \frac{1}{12}(2R_{\text{b,eq}})t_{\text{b}}^3 = \frac{R_{\text{b,eq}}t_{\text{b}}^3}{6} \quad (4.41)$$

The *Parallel Axis Theorem* is now applied to shift to the neutral axis:

$$I_{\text{rect}} = I_{\text{rect,centroid}} + A_{\text{rect}} \left(\frac{t_{\text{b}}}{2} \right)^2, \quad (4.42)$$

where

$$A_{\text{rect}} = 2R_{\text{b,eq}} \cdot t_{\text{b}} \quad (4.43)$$

represents the area of the rectangle, and $\frac{t_{\text{b}}}{2}$ denotes the distance from the centroid to the neutral axis.

Final adjusted second moment of area is given by:

$$I_{\text{rect}} = \frac{R_{\text{b,eq}}t_{\text{b}}^3}{6} + (2R_{\text{b,eq}}t_{\text{b}}) \left(\frac{t_{\text{b}}}{2} \right)^2 = \frac{2R_{\text{b,eq}}t_{\text{b}}^3}{3} \quad (4.44)$$

3. *Total second moment of area calculation:*

$$I_{\text{total}} = \underbrace{\frac{\pi}{8} (R_{\text{b,eq}}^4 - r_{\text{b}}^4)}_{\text{Semicircular annulus}} + \underbrace{\frac{2R_{\text{b,eq}}t_{\text{b}}^3}{3}}_{\text{Rectangular base}} \quad (4.45)$$

4. *Bending stiffness calculation:* Using the relationship between stiffness, Young's modulus E , and geometry:

$$K_{\text{seg}} = \frac{EI_{\text{total}}}{L_{\text{seg}}} \quad (4.46)$$

Substituting I_{total} :

$$K_{\text{seg}} = \frac{E}{L_{\text{seg}}} \left(\frac{\pi}{8} (R_{\text{b,eq}}^4 - r_{\text{b}}^4) + \frac{2R_{\text{b,eq}}t_{\text{b}}^3}{3} \right). \quad (4.47)$$

This approximation of the bending stiffness will serve as a critical component in the following PRB formulation, enabling the accurate modeling of a ribbed bellow segment's resistance to bending.

PRB Model Formulation

The pseudo-rigid-body (PRB) model simplifies the analysis of compliant mechanisms by approximating a flexible beam as a rigid link with a torsional spring at its base. This modeling technique represents compliant structures as a system of rigid bodies connected by joints with spring elements, effectively translating complex deformation behavior into simpler rigid-body kinematics. Compared to FEM analysis, the PRB model significantly reduces computational complexity while maintaining accuracy in capturing large deflections and nonlinear behavior. This approach enables the analysis of compliant systems using methods traditionally applied to rigid-body mechanisms (Howell et al., 2013).

By applying the PRB model to the bellow segments, the kinematics can be defined using rigid-body transformations, while spring elements mimic the material's elastic properties. This combination provides an efficient and accurate framework for modeling the bending behavior of individual bellow segments under actuation. The following analysis applies the proposed methodology to a bellow segment of a finger SPA, with its pseudo-rigid-body moment-motion approximation illustrated in Figure 4.13.

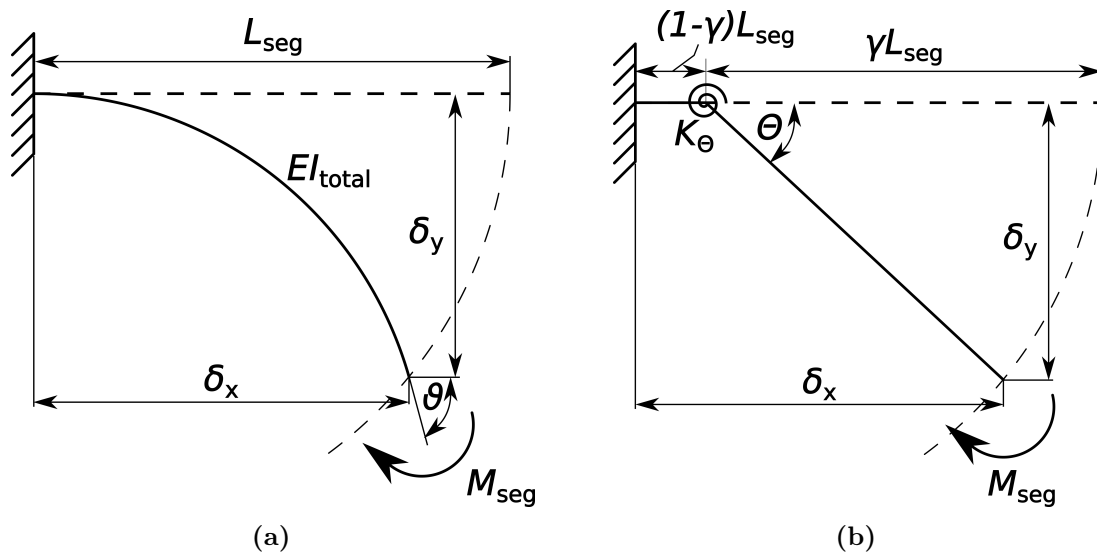


Figure 4.13 Pseudo-rigid-body moment-motion approximation of a ribbed elastic segment: (a) Cantilever beam under end-moment loading, illustrating deflections in the horizontal (δ_x) and vertical (δ_y) directions. (b) Simplified pseudo-rigid-body model using an equivalent torsional spring (K_{Θ}) and rigid links to approximate the bending behavior, with characteristic pivot and radius γ identified.

In the first step, the horizontal (δ_x/m) and vertical (δ_y/m) deflections of the beam tip are calculated. These are given as (Howell et al., 2013):

$$\delta_x = (1 - \gamma)L_{\text{seg}} + \gamma L_{\text{seg}} \cos \Theta \quad (4.48)$$

$$\delta_y = \gamma L_{\text{seg}} \sin \Theta \quad (4.49)$$

where γ is the characteristic radius factor, typically $\gamma = 0.7346$ for end-moment loading; L_{seg}/m is the total length of the beam; and Θ_{rad} is the pseudo-rigid-body angle, which approximates the deformation of the beam (see Figure 4.13). The Equation (4.48) consists of:

$(1 - \gamma)L_{\text{seg}}$: the rigid portion of the beam length that does not contribute to bending.

$\gamma L_{\text{seg}} \cos \Theta$: the horizontal projection of the curved portion of the beam.

Equation (4.49) provides the vertical deflection δ_y , which is entirely due to the curved portion of the beam, represented by $\gamma L_{\text{seg}} \sin \Theta$. The beam end angle ϑ/rad is now calculated in relation to the pseudo-rigid-body angle Θ . These two are related as:

$$\vartheta = c_{\Theta} \cdot \Theta \quad (4.50)$$

where $c_{\Theta} = 1.5164$ is the parametric angle coefficient for end-moment loading, while the equation accounts for the scaling between the pseudo-rigid-body angle Θ and the actual beam end angle ϑ . The stiffness of the equivalent torsional spring is given by:

$$K_{\Theta} = c_{\Theta} \frac{EI_{\text{total}}}{L_{\text{seg}}} = c_{\Theta} K_{\text{seg}} \quad (4.51)$$

The applied moment M_{seg} is related to the pseudo-rigid-body angle Θ as:

$$M_{\text{seg}} = K_{\Theta} \cdot \Theta \quad (4.52)$$

By substituting for K_{Θ} , the following is obtained:

$$M_{\text{seg}} = c_{\Theta} \cdot \frac{EI_{\text{total}}}{L_{\text{seg}}} \cdot \Theta \quad (4.53)$$

Alternatively, using $\Theta = \vartheta/c_\Theta$, M_{seg} can be expressed in terms of ϑ as:

$$M_{\text{seg}} = \frac{EI_{\text{total}}}{L_{\text{seg}}} \cdot \vartheta \quad (4.54)$$

The horizontal and vertical deflections are now determined based on the beam end angle. By substituting $\Theta = \vartheta/c_\Theta$ equations (4.48) and (4.49) are rewritten in terms of ϑ :

$$\delta_x = (1 - \gamma)L_{\text{seg}} + \gamma L_{\text{seg}} \cos\left(\frac{\vartheta}{c_\Theta}\right) \quad (4.55)$$

$$\delta_y = \gamma L_{\text{seg}} \sin\left(\frac{\vartheta}{c_\Theta}\right) \quad (4.56)$$

For end-moment loading, the characteristic radius factor is $\gamma = 0.7346$, and the parametric angle coefficient is $c_\Theta = 1.5164$. These parameters are derived from experimental and theoretical studies to ensure accurate modeling (Howell et al., 2013).

According to the results presented in Section 4.3.3, the proposed PRB model requires minor modifications to accurately capture the small geometric nonlinearities during bending. To improve its precision, an additional quadratic term, β_{EI} , has been incorporated into (4.54). The updated equation explicitly defines the bending angle ϑ as a function of the moment M_{seg} .

$$\vartheta = \frac{M_{\text{seg}}L_{\text{seg}}}{EI_{\text{total}}} \left(1 + \beta_{EI} \frac{M_{\text{seg}}L_{\text{seg}}}{EI_{\text{total}}} \right) \quad (4.57)$$

The introduced PRB parameters γ , c_Θ and β_{EI} will be subject to a subsequent model optimization process.

Axial and Bending Elongation of the Bellow Structure

To account for the elongation of the SPA bellow during bending, the previously introduced PRB model is extended by incorporating axial and bending effects to calculate the total elongation of the bellow structure.

1. *Axial Elongation*: the axial elongation caused by the axial force F_{seg} from (4.36), acting on the bellows, is given by:

$$\Delta L_{\text{axial}} = \frac{FL_{\text{seg}}}{EA_{\text{eq,seg}}} \quad (4.58)$$

where L_{seg}/m is the length of the bellows, $E\text{Pa}$ is the Young's modulus of the material, and $A_{\text{eq,seg}}/m^2$ is the equivalent cross-sectional area of the bellows, computed using (4.39) and (4.43) as $A_{\text{eq,seg}} = A_{\text{semi}} + A_{\text{rect}}$.

2. *Bending Elongation*: suppose the segment radius of curvature caused by bending (see Figure 4.9) is unavailable. In that case, bending elongation can be expressed as a parametric function of measurable parameters such as the bending angle ϑ and the number of ribs $n_{\text{r,seg}}$. Using a fitted model, the bending elongation can be written as:

$$\Delta L_{\text{bending}} = f(\vartheta, n_{\text{r,seg}}) \quad (4.59)$$

For example, if experimental data suggests a quadratic dependence on ϑ and a linear dependence on $n_{\text{r,seg}}$, the bending elongation could be modeled as:

$$\Delta L_{\text{bending}} = \beta_{\vartheta} \vartheta^2 + \beta_n n_{\text{r,seg}} \quad (4.60)$$

where β_{ϑ} and β_n are fitted coefficients based on experimental or simulation data, while ϑ is the bending angle.

3. *Total Elongation*: the total elongation is the sum of the axial and bending contributions:

$$\Delta L_{\text{total}} = \Delta L_{\text{axial}} + \Delta L_{\text{bending}} \quad (4.61)$$

Substituting the expressions for axial and bending elongations:

$$\Delta L_{\text{total}} = \frac{F_{\text{seg}} L_{\text{seg}}}{E A_{\text{eq,seg}}} + f(\vartheta, n_{\text{r,seg}}) \quad (4.62)$$

or, using a specific bending model:

$$\Delta L_{\text{total}} = \frac{F_{\text{seg}} L_{\text{seg}}}{E A_{\text{eq,seg}}} + \beta_{\vartheta} \vartheta^2 + \beta_n n_{\text{r,seg}} \quad (4.63)$$

This formulation accounts for both the axial and bending effects in calculating the total elongation of a bellows structure. The introduced elongation parameters, β_{ϑ} (representing elongation due to bending) and β_n (elongation due to the number of ribs), will be subject to a subsequent model optimization process.

Integrating Individual PRB Models in the Entire Model of the Actuator

By modeling individual ribbed bellow segments using the PRB formulation, individual deflections in the x and y axis directions can be estimated using equations (4.55) and (4.56). Additionally, the total elongation of a single segment can be estimated using equation (4.63). In the SPA, all ribbed segments are connected with rods, dictating inter-joint distances. These distances were kept constant, as analyzed in table 4.8. They will be denoted as $L_{i,i+1}$, where i denotes the joint before the connecting rod, and $i + 1$ the joint after the rod. Possible inter-joint distances are:

- $L_{\text{MCP,PIP}}$ between the MCP and PIP joints,
- $L_{\text{PIP,DIP}}$ between the PIP and DIP joints,
- $L_{\text{DIP,TIP}}$ between the DIP joint and the TIP of the finger.

To express the final pose of the finger in the fixed reference frame originating at the MCP joint, a set of kinematic transformations along the kinematic tree must be properly constructed, starting from the MCP joint and extending to the TIP. Since every deflection and elongation is expressed in its own local coordinate system, a rotational transformation is applied to the deflected coordinates using the rotation angles:

- Deflections due to the elongation of the end of the i -th bellow segment are computed using the i -th cumulative angle ϑ_i
- Deflections due to the bending of the end of the i -th bellow segment are computed using the $(i - 1)$ -th cumulative angle ϑ_{i-1}

The kinematic transformations for the start and end position of the MCP joint bellow segment are, therefore, the following:

$$\begin{aligned}
 x_{\text{start,MCP}} &= 0 \\
 y_{\text{start,MCP}} &= 0 \\
 x_{\text{end,MCP}} &= x_{\text{start,MCP}} + \delta_{x,\text{MCP}} \underbrace{\cos 0}_1 - \delta_{y,\text{MCP}} \underbrace{\sin 0}_0 \\
 &\quad + \Delta L_{\text{total,MCP}} \cos \vartheta_{\text{MCP}} \\
 y_{\text{end,MCP}} &= y_{\text{start,MCP}} + \delta_{x,\text{MCP}} \underbrace{\sin 0}_0 + \delta_{y,\text{MCP}} \underbrace{\cos 0}_1 \\
 &\quad + \Delta L_{\text{total,MCP}} \sin \vartheta_{\text{MCP}}
 \end{aligned} \tag{4.64}$$

The kinematic transformations for the start and end positions of the PIP joint bellow segment are, in turn, the following:

$$\begin{aligned}
x_{\text{start,PIP}} &= x_{\text{end,MCP}} + L_{\text{MCP,PIP}} \cos \vartheta_{\text{MCP}} \\
y_{\text{start,PIP}} &= y_{\text{end,MCP}} + L_{\text{MCP,PIP}} \sin \vartheta_{\text{MCP}} \\
x_{\text{end,PIP}} &= x_{\text{start,PIP}} + \delta_{x,\text{PIP}} \cos \vartheta_{\text{MCP}} - \delta_{y,\text{PIP}} \sin \vartheta_{\text{MCP}} \\
&\quad + \Delta L_{\text{total,PIP}} \cos (\vartheta_{\text{MCP}} + \vartheta_{\text{PIP}}) \\
y_{\text{end,PIP}} &= y_{\text{start,PIP}} + \delta_{x,\text{PIP}} \sin \vartheta_{\text{MCP}} + \delta_{y,\text{PIP}} \cos \vartheta_{\text{MCP}} \\
&\quad + \Delta L_{\text{total,PIP}} \sin (\vartheta_{\text{MCP}} + \vartheta_{\text{PIP}})
\end{aligned} \tag{4.65}$$

The kinematic transformations for the start and end position of the DIP joint bellow segment are following:

$$\begin{aligned}
x_{\text{start,DIP}} &= x_{\text{end,PIP}} + L_{\text{PIP,DIP}} \cos (\vartheta_{\text{MCP}} + \vartheta_{\text{PIP}}) \\
y_{\text{start,DIP}} &= y_{\text{end,PIP}} + L_{\text{PIP,DIP}} \sin (\vartheta_{\text{MCP}} + \vartheta_{\text{PIP}}) \\
x_{\text{end,DIP}} &= x_{\text{start,DIP}} + \delta_{x,\text{DIP}} \cos (\vartheta_{\text{MCP}} + \vartheta_{\text{PIP}}) - \delta_{y,\text{DIP}} \sin (\vartheta_{\text{MCP}} + \vartheta_{\text{PIP}}) \\
&\quad + \Delta L_{\text{total,DIP}} \cos (\vartheta_{\text{MCP}} + \vartheta_{\text{PIP}} + \vartheta_{\text{PIP}}) \\
y_{\text{end,DIP}} &= y_{\text{start,DIP}} + \delta_{x,\text{DIP}} \sin (\vartheta_{\text{MCP}} + \vartheta_{\text{PIP}}) + \delta_{y,\text{DIP}} \cos (\vartheta_{\text{MCP}} + \vartheta_{\text{PIP}}) \\
&\quad + \Delta L_{\text{total,DIP}} \sin (\vartheta_{\text{MCP}} + \vartheta_{\text{PIP}} + \vartheta_{\text{PIP}})
\end{aligned} \tag{4.66}$$

Experimental Validation of the PRB Model

In this section, the PRB parameters are optimized and validated experimentally. The optimization was performed using the `scipy.optimize.basinhopping` algorithm. This global optimization method combines stochastic sampling to escape local minima and identify the optimal solution (Olson et al., 2012; Wales and Doye, 1997). The algorithm is initialized with a predefined decision vector, randomly perturbed by small steps to explore potentially better solutions. Even if a slightly worse solution is found, it may be accepted as a new starting point for subsequent perturbations (or hops) with a certain probability, promoting exploration of the solution space. The following material properties and measured dimensions, obtained from the device prototype, are used as input values for the model optimization:

- Young's modulus for TPU 85A: $E = 27 \text{ MPa}$
- Outer radius for projected surface: $R_{\text{seg}} = 14.7 \text{ mm}$

- Inner radius for projected surface: $r_{\text{seg}} = 8.425$ mm
- Outer bellow radius: $R_{\text{b}} = 11$ mm
- Inner bellow radius: $r_{\text{b}} = 3$ mm
- Thickness of reinforcing layer: $t_{\text{b}} = 2.5$ mm
- Number of ribs per segment for I finger: $n_{\text{r,seg}} = 7, 5$ and 5
- Number of ribs per segment for L finger: $n_{\text{r,seg}} = 7, 5$ and 4

During each iteration, a random step was sampled within the \pm step size range. The initial step size was set to 0.01 and dynamically adjusted throughout the optimization process to improve convergence. Additionally, a variable-specific multiplication factor was applied to the step size to account for differences in magnitude across parameters, as shown in Table 4.10.

Table 4.10 Variable specific step size multiplication factors in BH optimization.

Parameter	λ	γ	c_{Θ}	β_{EI}	β_{ϑ}	β_n
Multiplication Factor	2	2	6	10	10	1

The 6-dimensional optimization process was conducted over 1×10^6 iterations with 4 repetitions, each using a different sampled initial decision vector within the bounds specified in Table 4.11. A temperature parameter 0.2 controlled the acceptance probability of slightly worse solutions, allowing for greater exploration at higher values. A custom adaptive step size was implemented, adjusting every 100 iterations. After each adjustment, the step size was scaled by a factor of 0.9 through multiplication or division, ensuring that approximately 60% of all steps were accepted during the optimization.

The 6-dimensional optimization process was conducted over 1×10^6 iterations with 4 repetitions, each using a different sampled initial decision vector within the bounds specified in Table 4.11. A temperature parameter 0.2 controlled the acceptance probability of slightly worse solutions, allowing for greater exploration at higher values. In the context of the basin-hopping (BH) algorithm, the temperature serves as a parameter in the Metropolis acceptance criterion (Virtanen et al., 2020). It determines the likelihood of accepting solutions with higher function values, facilitating exploration of the search space and enabling jumps between basins of attraction. Higher temperatures increase the probability of accepting worse solutions, promoting global optimization by escaping

local minima. A custom adaptive step size was implemented, adjusting every 100 iterations. After each adjustment, the step size was scaled by a factor of 0.9 through multiplication or division, ensuring that approximately 60% of all steps were accepted during the optimization.

Table 4.11 provides the upper and lower bounds used to constrain the optimization problem and the calculated optimal parameters for each segment of the index and little fingers. Additionally, the table includes the mean and maximum L2 norms (i.e., mean and maximum Euclidean distance errors) for both fingers. These errors represent the positioning error of the modified PRB model with respect to FEM results, taking into account all joints and input pressures within the range of 0 to 3 bar. Notably, the maximum error in both cases remains below 3.8 mm, while the mean error is below 1.3 mm, demonstrating the effectiveness and accuracy of the extended PRB model.

Table 4.11 PRB model optimization limits and optimal parameters.

Parameter	Optimization limits		Index			Little		
	Lower	Upper	MCP	PIP	DIP	MCP	PIP	DIP
λ	0.4	1.5	1.489	1.15	0.509	1.429	0.515	0.404
γ	0	1	0.267	0.684	0.99	0.854	0.719	0.906
c_{Θ}	1	8	1.252	3.154	1.553	3.136	1.661	5.336
β_{EI}	-1	20	10.254	17.464	-0.380	11.728	-0.267	-0.053
β_{ϑ}	0	15	9.976	6.781	9.505	7.338	6.397	2.836
β_n	0	0.2	0.0551	0.0074	0.1704	0.0815	0.163	0.122
Mean L2 norm/mm:			1.279			0.703		
Max L2 norm/mm:			3.799			3.657		

Figure 4.14 presents a comparison between the results obtained from FEM analyses, described in Section 4.3.3, and the PRB-modeled angular motion of the I and L SPAs in the FE plane under varying pressure levels. Both FEM (triangles) and PRB (circles) exhibit similar motion trajectories, demonstrating that the PRB model closely approximates the FEM solution. The color gradient represents the L2 norm difference between the two methods, with higher deviations (yellow regions) indicating points where the PRB model diverges from the FEM results. Overall, the agreement between the two models is strong, particularly for the L finger at lower pressures, where deviations remain minimal. However, slight divergences are observed at higher pressures and larger displacements for both the L and I fingers. Despite these localized differences, the PRB model provides a close approximation to FEM results.

Incorporating material properties into the PRB model offers several advantages over FEM approach, including greater computational efficiency and simplicity. These benefits enable faster design iterations and kinematic computations, making the approach suitable for real-time control applications. This method allows for the adjustment of design dimensions and input pressures to achieve the desired motion profile for a final actuator design compatible with the human hand. The PRB model enables optimizing the actuator's performance for more specific grasp-oriented tasks, as discussed in Chapter 3, by evaluating various parameter combinations quickly. This approach streamlines the design process and minimizes the need for time-intensive physical prototyping.

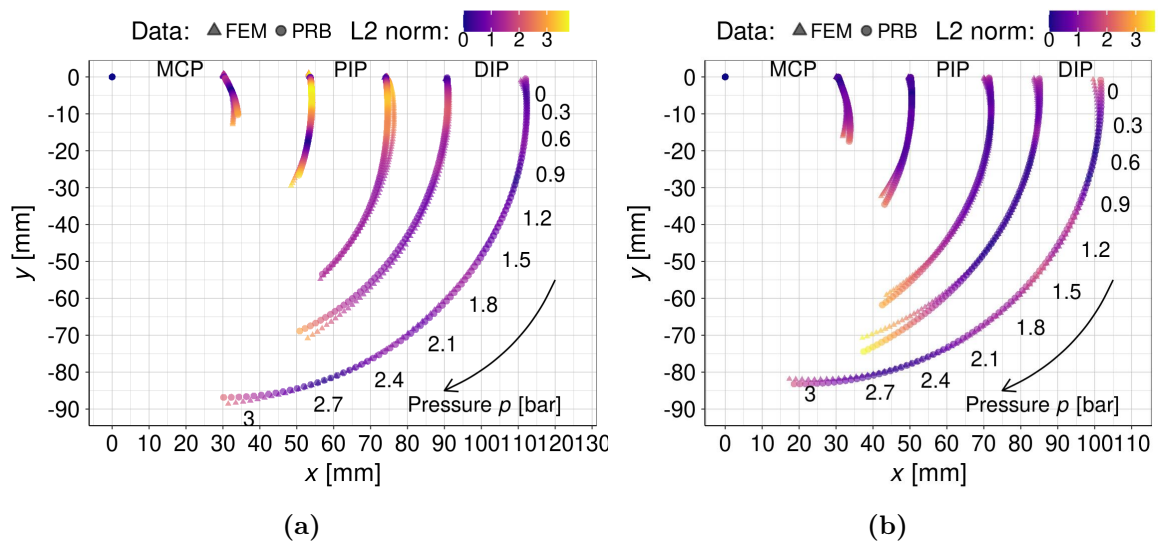


Figure 4.14 Comparison of pressurized bending of SPAs in the FE plane using finite element method (FEM) analyses (triangles) and pseudo-rigid body (PRB) modeling (circles). The L2 norm represents the point-by-point error metric between the two methods. SPAs: (a) Index finger, (b) Little finger.

4.4 Soft Rehabilitation Glove Prototyping and Experimental Validation

In this section, the fabrication process of the soft glove prototype is briefly outlined, employing advanced 3D printing techniques following the SPA specifications provided in Section 4.3.2.

Fabrication of Structural Components

The structural components of the rehabilitation glove were fabricated using a Prusa i3 MK3S 3D printer (Prusa Research, 2023). The print settings were optimized for TPU flexibility and performance. A bed temperature of 50 °C was used to improve the adhesion of the first layer, which was set at 0.25 mm to establish a strong base, while subsequent layers were printed at 0.2 mm. The printing speed was reduced to 10 mm s⁻¹ to enhance control and precision with the flexible material, and the transition speed between extrusion moves was set at 30 mm s⁻¹ to minimize oozing and transition time. Filament retraction was disabled to prevent air bubbles and extrusion issues. An infill density of 35 % was selected to balance material efficiency with structural integrity. The cooling fan was turned off to ensure proper layer adhesion, and the extrusion rate was increased to 105 %, with the first layer set at 110 % to guarantee complete material coverage, eliminating gaps and weak points. The optimal wall thickness for the SPA bellow segments was set to 0.8 mm, balancing flexibility and stiffness.

After the SPAs were fabricated, the mounting frame was 3D-printed using TPU. The frame was designed to wrap around the user's hand, conforming to its shape to ensure a flexible, ergonomic fit, while properly aligning the SPAs. Additional polylactic acid (PLA) rings were utilized to securely attach the actuators to the fingers, while hook-and-loop straps provided easy adjustments and customization based on individual user preferences. Once all components were prepared, the glove was assembled.

Assembly of the Soft Glove

The thumb, index, middle, ring, and little finger actuators were attached to the mounting frame using a sliding dovetail joint (see detail in Figure 4.15a), providing both stability and modularity. This design facilitated easy assembly, disassembly, and adaptability.

The final glove assembly (Figure 4.15b) is connected to FESTO pneumatic tubing catalog number PUN-H 2x0.4 (Festo Corporation, 2024), featuring a 1.2 mm inner diameter. This diameter was chosen to align with the actuators' dimensions, facilitating seamless integration with the glove's support structure. Additionally, the selected tubing provides sufficient airflow for the SPAs, which do not require high-speed operation, ensuring efficient performance.

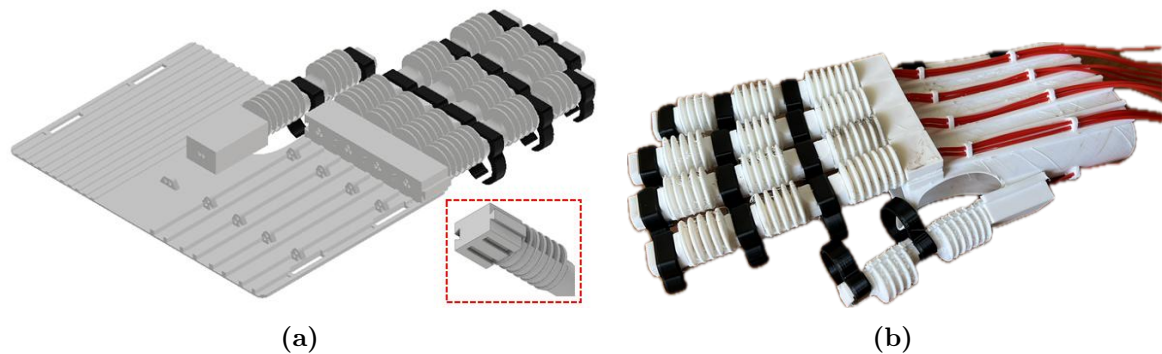


Figure 4.15 Assembling the rehabilitation glove: (a) 3D model of the rehabilitation glove assembly with sliding dovetail joint detail. (b) 3D printed glove prototype with compressed air supply tubes attached and glued for secure connection (Kladarić, 2024).

Functional Testing

Final tests were conducted to evaluate the functionality of the rehabilitation glove prototype. A healthy adult participant voluntarily participated in the experiment and wore the glove. After fitting the glove, the participant assessed its ability to support natural finger movement by applying muscle force. A controlled experiment was performed to simulate real-world usage by gradually increasing the actuator pressure while ensuring the participant's hand remained fully relaxed and without muscle engagement. Figure 4.16a shows the fully assembled soft robotic device in its reference position, while Figure 4.16b illustrates its actuated state.



Figure 4.16 Soft-robotic glove fitted to the user's hand: (a) all SPAs in the initial position and (b) all SPAs activated.

The glove's initial prototype demonstrated basic functionality and an ergonomic design, with the participant reporting ease of use and no discomfort or fatigue after

10 minutes of wear. While further refinements and improvements in the 3D printing process are necessary to enhance durability, this prototype demonstrates the feasibility of 3D printing a functional, flexible, single-body structure for finger rehabilitation.

This chapter presented a comprehensive methodology for designing and developing a grasp-oriented rehabilitation glove. The approach begins with modeling the human finger through kinematic reductions and analysis of range-of-motion limits in relation to anatomical constraints. This finger model serves as the foundation for deriving the kinematic tree and defining the morphology of the SPA used for finger actuation. Material properties were incorporated into the SPA design through FEM modeling to achieve accurate bending deflection estimation. A modified PRB approach was introduced to reduce computational complexity while maintaining accuracy, approximating the FEM-obtained positioning results for efficient design iterations. This approach integrates SPA-specific approximations of moments, forces, and elongations coupled with an optimization procedure.

The rehabilitation glove's functionality can be enhanced by independently controlling the input pressure for each bellow segment. This fine-grained pressure control enables the device to perform various grasp types by modifying the relative bending angle profile between segments, effectively changing intra-joint dependencies through pressure regulation. This capability aligns with the kinematic analysis presented in Chapter 3, which identified such dependencies across 23 different grasps. The 116 intra-finger dependency-movement relationships, categorized into 30 clusters, complement this methodology and establish a pathway toward more refined hand rehabilitation for activities of daily living. By incorporating these kinematic reductions in both the design phase and control system, the glove can support rehabilitation across a broader spectrum of functional grasps.

Future development of the device control system could incorporate intent-driven assistive control based on the Koopman framework for grip force forecasting using sEMG, as detailed in Chapter 2. This integration would further enhance the rehabilitation glove's adaptability, responsiveness to user intentions, and rehabilitation potential.

Chapter 5

Conclusion

This dissertation has explored the intersection of rehabilitation science, biomechanics, and soft robotics to address the significant global challenge of rehabilitating hand function impairments. Three primary aims drove the research: developing a framework for electromyography (EMG)-based real-time grip force estimation and prediction, creating simplified yet accurate kinematic hand models, and designing a framework for prototyping a biomechatronic soft robotic hand rehabilitation device. Through a systematic approach across multiple domains, this work has yielded significant contributions to the field of rehabilitation robotics.

Hypotheses Validation

The first hypothesis proposed that hand grip force could be accurately assessed and predicted in real-time using sEMG signals from a single sensing position. The results from Chapter 2 strongly support this hypothesis, demonstrating:

- Development of optimized signal processing methods that achieved high peak cross-correlations between EMG and grip force signals (median between 0.958 and 0.962) using a single forearm sensing position.
- A weighted mean absolute percentage error (wMAPE) of approximately 5.5% for estimated grip force and approximately 17.9% for predictions with a 0.5-second horizon.
- The algorithm’s ability to process, estimate, and predict a 0.5-second sEMG signal batch in approximately 30 ms, enabling practical real-time implementation.

The results also demonstrated robustness to electrode positioning variations. A 2-factor randomized block design experiment involving 13 participants was conducted to evaluate two sensing positions near the flexor carpi ulnaris muscle while controlling for subject variability as a blocking factor. ANOVA confirmed no statistically significant effect of sensor placement on estimation or prediction errors (p -values of 0.422 and 0.853, respectively), indicating resilience to minor variations in electrode positioning—a critical feature for rehabilitation applications where precise sensor placement cannot always be guaranteed.

The second hypothesis suggested that introducing one-to-one joint dependencies could significantly simplify complex hand kinematics during grasping and generalize it. Chapter 3 verified this hypothesis through:

- Analysis of the largest known database of human hand movements (NinaPro), providing strong evidence for generalization across a demographically diverse sample of 77 subjects and 23 different functional grasps relevant to daily activities.
- Demonstration of significant kinematic reduction, showing that grasp modeling during flexion/extension movements can be achieved with just 5 to 15 degrees of freedom (median 12 DOFs) instead of the hand’s full 16 DOFs for finger joints.

Through correlation analysis, 116 highly correlated dependency-movement relationships were identified across all investigated grasps. Each relationship was modeled using regularized GLM for predictor selection and weighted LME models accounting for subject-specific random and dependency-specific fixed effects. This produced models with absolute wMAE values ranging from 2.4 to 16° (median 7.5°) and relative wwMAPE values from 11 to 56.1% (median 27.9%). Hierarchical clustering further reduced the number of models from 116 to 30 while maintaining prediction accuracy.

The third hypothesis proposed that simplified hand kinematic models, combined with soft-actuator modeling techniques, could be leveraged to design and fabricate 3D-printed soft robotic rehabilitation devices. Chapter 4 supported this through:

- A biomechanically-informed reduced kinematic model of the index finger, including 50th percentile male anthropometry, that served as a basis for designing an asymmetric bellow soft pneumatic actuator (SPA), demonstrating how simplified hand kinematic models can directly inform the workspace requirements and motion constraints for effective rehabilitation devices.

-
- Development of complementary soft actuator modeling techniques that balanced computational complexity with design accuracy: detailed FEM simulations validated the performance characteristics and mechanical behavior of the actuators, while simplified pseudo-rigid-body models enabled rapid design iterations.
 - Successful fabrication of functional soft pneumatic actuators using 3D-printed thermoplastic polyurethane (TPU) as a single-body structure, demonstrating the feasibility of translating simplified kinematic models into physical soft robotic rehabilitation devices through additive manufacturing techniques.

Key Contributions and Implications

Developing a Koopman-based data-driven approach for grip force estimation and prediction represents a significant advancement for rehabilitation robotics. This approach can serve as a basis for adaptive assistance by dynamically supplementing patients' voluntary efforts with only the necessary force. The ability to predict grip force from a single sensor position with high accuracy reduces system complexity and promotes affordability while maintaining effectiveness. The novel spectral mask technique developed for signal processing offers unique insights for EMG analysis beyond rehabilitation applications. This approach could benefit various human-machine interface designs where reliable muscle activity detection is critical by selectively enhancing or attenuating specific frequency components that maximize correlation with grip force.

The reduced kinematic hand modeling approach, through intra-finger dependencies, establishes motion patterns across subjects that significantly reduce the degrees of freedom required for accurate hand modeling. Unlike previous synergy-based approaches that need substantial synergies to account for only $\sim 80\%$ of variance, our simplified models maintain precision while reducing implementation complexity by providing direct one-to-one intra-finger dependencies. This contribution addresses a fundamental challenge in rehabilitation robotics: creating devices that balance biomechanical accuracy with practical simplicity. This research streamlines human hand modeling while preserving the precision needed for effective therapy by identifying clusters of similar dependencies across different grasps.

The iterative methodology for designing, modeling, and fabricating 3D-printed soft actuators, based on finger kinematics models, represents a structured approach to developing rehabilitation devices that adapt to individual patient needs. The dual modeling approach—combining detailed FEM simulations with simplified PRB

models for iterative design—provides both accuracy and computational efficiency. The prototype development demonstrated that soft pneumatic actuators can effectively support hand movements while maintaining the compliance necessary for safe human-robot interaction. This approach offers a promising alternative to rigid exoskeletal designs, often imposing unnatural movement constraints.

Practical Applications

Integrating these three complementary approaches—EMG-driven adaptive control, simplified kinematic models, and optimized soft actuators—establishes a comprehensive framework for developing the next generation of rehabilitation devices. This framework addresses several critical challenges:

- **Personalization:** The EMG-based estimation enables therapy that adapts to individual patient capabilities.
- **Simplicity:** The reduced kinematic models make implementation feasible with fewer actuators.
- **Affordability:** Soft 3D-printed actuators provide a cost-effective alternative to complex rigid systems.
- **Accessibility:** The reduced sensor requirements and computational efficiency make the technology more widely deployable.

Such rehabilitation systems could significantly impact recovery trajectories for stroke patients, who currently face limitations in therapy intensity due to healthcare constraints. These technologies could help bridge the gap between optimal and actual therapy delivery by providing consistent, high-intensity, adaptive assistance.

Limitations and Future Directions

Despite the promising results, several key limitations warrant consideration. First, the EMG-based grip force estimation approach was validated for medium wrap grasp only, and future work must extend this methodology to multiple functional grasp types required for comprehensive ADL support.

Second, while significantly simplified, the kinematic models require further validation in clinical populations with neurological impairments where spasticity, muscle tone abnormalities, and compensatory movement patterns might alter the identified

joint dependencies. Additionally, these models focused only on flexion/extension movements while excluding finger abduction/adduction, which should be incorporated in future iterations to capture the full range of hand motion. This validation should include diverse age groups and varying degrees of motor impairment to ensure broad applicability.

The rehabilitation glove prototype requires further development to increase its technological readiness level (TRL) through iterative refinement and standardized testing protocols. Future work should examine alternative hyperelastic materials and extend the kinematic framework to include thumb articulation, critical for enabling functional opposition movements in precision grasping patterns.

Bibliography

- AM, F. (2022). Ultrafuse tpu 85a - technical data sheet. Accessed: 2025-02-16.
- Ang, B. W. K. and Yeow, C.-H. (2017). Print-it-yourself (piy) glove: A fully 3d printed soft robotic hand rehabilitative and assistive exoskeleton for stroke patients. In *2017 IEEE/RSJ International Conference on Intelligent Robots and Systems (IROS)*, pages 1219–1223. IEEE.
- Ang, B. W. K. and Yeow, C.-H. (2020). Design and modeling of a high force soft actuator for assisted elbow flexion. *IEEE Robotics and Automation Letters*, 5(2):3731–3736.
- Arantes, A. P., Bressan, N., Borges, L. R., and McGibbon, C. A. (2023). Evaluation of a novel real-time adaptive assist-as-needed controller for robot-assisted upper extremity rehabilitation following stroke. *PLOS ONE*, 18(10):e0292627.
- Arbabi, H. and Mezić, I. (2017). Ergodic theory, dynamic mode decomposition, and computation of spectral properties of the koopman operator. *SIAM Journal on Applied Dynamical Systems*, 16(4):2096–2126.
- Arifvianto, B., Iman, T. N., Prayoga, B. T., Dharmastiti, R., Salim, U. A., Mahardika, M., and Suyitno (2021). Tensile properties of the fff-processed thermoplastic polyurethane (tpu) elastomer. *The International Journal of Advanced Manufacturing Technology*, 117(5–6):1709–1719.
- Armanini, C., Boyer, F., Mathew, A. T., Duriez, C., and Renda, F. (2023). Soft robots modeling: A structured overview. *IEEE Transactions on Robotics*, 39(3):1728–1748.
- Assistance, S. U. (2020). Abaqus documentation.
- Barański, R. and Kozupa, A. (2014). Hand grip-EMG muscle response. *Acta Physica Polonica A*, 125(4A):A-7–A-10.
- Bardin, A., Le Gac, P.-Y., Cérantola, S., Simon, G., Bindi, H., and Fayolle, B. (2020). Hydrolytic kinetic model predicting embrittlement in thermoplastic elastomers. *Polymer Degradation and Stability*, 171:109002.
- Bates, D., Mächler, M., Bolker, B., and Walker, S. (2015). Fitting linear mixed-effects models using lme4. *Journal of Statistical Software*, 67(1).
- Bazina, T. (2021a). GitHub - tbazina/godirect-ros: ROS package for reading from Vernier Go Direct® Sensors using BLE. https://github.com/tbazina/godirect_ros. [Accessed 2025-01].

- Bazina, T. (2021b). GitHub - tbazina/shimmer-ros: ROS interface to Shimmer3 EMG sensors. https://github.com/tbazina/shimmer_ros. [Accessed 2025-01].
- Bazina, T. (2022a). GitHub - tbazina/grip-emg-optimize: Forecasting grip force from sEMG. <https://github.com/tbazina/grip-emg-optimize>. [Accessed 2025-01].
- Bazina, T. (2022b). GitHub - tbazina/kinematic-database: A large calibrated database of hand movements and grasps kinematics — github.com. <https://github.com/tbazina/kinematic-database>. [Accessed 07-01-2025].
- Bazina, T., Kamenar, E., Fonoberova, M., and Mezić, I. (2024a). Koopman-driven grip force prediction through emg sensing.
- Bazina, T., Kladarić, M., Kamenar, E., and Gregov, G. (2024b). Development of rehabilitation glove: Soft robot approach. *Actuators*, 13(12):472.
- Bazina, T., Mauša, G., Zelenika, S., and Kamenar, E. (2024c). Reducing hand kinematics by introducing grasp-oriented intra-finger dependencies. *Robotics*, 13(6):82.
- Bazina, T., Schnurrer-Luke-Vrbanić, T., Črnjarić-Žic, N., Zelenika, S., and Kamenar, E. (2022). Hand model with dependency constrained joints for applications in rehabilitation robotics. *Medicina Fluminensis*, 58(4):385–398.
- Bhat, A., Ambrose, J. W., and Yeow, R. C.-H. (2023). Composite soft pneumatic actuators using 3d printed skins. *IEEE Robotics and Automation Letters*, 8(4):2086–2093.
- Buryanov, A. and Kotiuk, V. (2010). Proportions of hand segments. *Int J Morphol*, 28(3):755–758.
- Cappello, L., Meyer, J. T., Galloway, K. C., Peisner, J. D., Granberry, R., Wagner, D. A., Engelhardt, S., Paganoni, S., and Walsh, C. J. (2018). Assisting hand function after spinal cord injury with a fabric-based soft robotic glove. *Journal of neuroengineering and rehabilitation*, 15:1–10.
- Cheng, Y., Lin, Y., Shi, H., Cheng, M., Zhang, B., Liu, X., Shi, C., Wang, Y., Xia, C., and Xie, W. (2024). Projections of the stroke burden at the global, regional, and national levels up to 2050 based on the global burden of disease study 2021. *Journal of the American Heart Association*.
- Chu, C.-Y. and Patterson, R. M. (2018). Soft robotic devices for hand rehabilitation and assistance: a narrative review. *Journal of neuroengineering and rehabilitation*, 15:1–14.
- Cleveland, W. S. (1979). Robust locally weighted regression and smoothing scatterplots. *Journal of the American Statistical Association*, 74(368):829–836.
- Cobos, S., Ferre, M., Sánchez-Urán, M. Á., Ortego, J., and Aracil, R. (2010). Human hand descriptions and gesture recognition for object manipulation. *Comput Methods Biomech Biomed Engin*, 13(3):305–317.
- Cohen, J. (2013). *Statistical Power Analysis for the Behavioral Sciences*. Routledge.

- Colombo, R. and Sanguineti, V. (2018). *Rehabilitation Robotics: Technology and Application*. Academic Press, London.
- Craig, J. J. (2014). *Introduction to Robotics: Mechanics and Control, 3rd edition*. Pearson Education Limited.
- Curkovic, P. and Cubric, G. (2021). Fused deposition modelling for 3d printing of soft anthropomorphic actuators. *International Journal of Simulation Modelling*, 20(2):303–314.
- Cutkosky, M. (1989). On grasp choice, grasp models, and the design of hands for manufacturing tasks. *IEEE Trans. Robot. Automat.*, 5(3):269–279.
- Delp, S. L., Anderson, F. C., Arnold, A. S., Loan, P., Habib, A., John, C. T., Guendelman, E., and Thelen, D. G. (2007). Opensim: Open-source software to create and analyze dynamic simulations of movement. *IEEE Transactions on Biomedical Engineering*, 54(11):1940–1950.
- Dobkin, B. H. (2004). Strategies for stroke rehabilitation. *The Lancet Neurology*, 3(9):528–536.
- Drmač, Z., Mezić, I., and Mohr, R. (2018). Data driven modal decompositions: Analysis and enhancements. *SIAM Journal on Scientific Computing*, 40(4):A2253–A2285.
- Drmač, Z., Mezić, I., and Mohr, R. (2020). On least squares problems with certain vandermonde–khatri–rao structure with applications to DMD. *SIAM Journal on Scientific Computing*, 42(5):A3250–A3284.
- Engelhardt, L., Melzner, M., Havelkova, L., Fiala, P., Christen, P., Dendorfer, S., and Simon, U. (2020). A new musculoskeletal AnyBody™ detailed hand model. *Comput Methods Biomech Biomed Engin*, 24(7):777–787.
- Feigin, V. L., Brainin, M., Norrving, B., Martins, S. O., Pandian, J., Lindsay, P., F Grupper, M., and Rautalin, I. (2025). World stroke organization: Global stroke fact sheet 2025. *International Journal of Stroke*, 20(2):132–144.
- Feix, T., Romero, J., Schmiedmayer, H.-B., Dollar, A. M., and Kragic, D. (2016). The grasp taxonomy of human grasp types. *IEEE Transactions on Human-Machine Systems*, 46(1):66–77.
- Festo Corporation, K. (2024). Plastic tubing pun-h, pun-h-duo. https://www.festo.com/media/catalog/203530_documentation.pdf. [Accessed: March 24, 2025].
- Frame, P. and Towne, A. (2023). Space-time POD and the hankel matrix. *PLOS ONE*, 18(8):e0289637.
- Gracia-Ibáñez, V., Sancho-Bru, J. L., Vergara, M., Jarque-Bou, N. J., and Roda-Sales, A. (2020). Sharing of hand kinematic synergies across subjects in daily living activities. *Scientific Reports*, 10(1).

- Gracia-Ibáñez, V., Vergara, M., Buffi, J. H., Murray, W. M., and Sancho-Bru, J. L. (2016). Across-subject calibration of an instrumented glove to measure hand movement for clinical purposes. *Computer Methods in Biomechanics and Biomedical Engineering*, 20(6):587–597.
- Haggerty, D. A., Banks, M. J., Kamenar, E., Cao, A. B., Curtis, P. C., Mezić, I., and Hawkes, E. W. (2023). Control of soft robots with inertial dynamics. *Science robotics*, 8(81):eadd6864.
- Haid, D. M., Duncan, O., Hart, J., and Foster, L. (2022). Characterisation of thermoplastic polyurethane (tpu) for additive manufacturing. *Tagungsband zum*, 14:85–88.
- Hasson, C. J., Manczurowsky, J., Collins, E. C., and Yarossi, M. (2023). Neurorehabilitation robotics: how much control should therapists have? *Frontiers in Human Neuroscience*, 17.
- Heckert, N. A., Filliben, J. J., Croarkin, C. M., Hembree, B., Guthrie, W. F., Tobias, P., and Prinz, J. (2012). Nist/sematech e-handbook of statistical methods (nist handbook 151).
- Heung, H. L., Tang, Z. Q., Shi, X. Q., Tong, K. Y., and Li, Z. (2020). Soft rehabilitation actuator with integrated post-stroke finger spasticity evaluation. *Frontiers in bioengineering and biotechnology*, 8:111.
- Holzbaur, K. R. S., Murray, W. M., and Delp, S. L. (2005). A model of the upper extremity for simulating musculoskeletal surgery and analyzing neuromuscular control. *Annals of Biomedical Engineering*, 33(6):829–840.
- Howell, L. L. (2001). *Compliant mechanisms*. Wiley. Literaturverzeichnis: Seite 385-397. - Index.
- Howell, L. L., Magleby, S. P., Olsen, B. M., and Wiley, J. (2013). *Handbook of Compliant Mechanisms*. Wiley.
- Huo, Y., Wang, X., Zhao, W., Hu, H., and Li, L. (2023). Effects of emg-based robot for upper extremity rehabilitation on post-stroke patients: a systematic review and meta-analysis. *Frontiers in Physiology*, 14:1172958.
- Iman, R. L., Helton, J. C., and Campbell, J. E. (1981). An approach to sensitivity analysis of computer models: Part i—introduction, input variable selection and preliminary variable assessment. *Journal of Quality Technology*, 13(3):174–183.
- Jarque-Bou, N., Gracia-Ibáñez, V., Sancho-Bru, J., Vergara, M., Pérez-González, A., and Andrés, F. (2016). Using kinematic reduction for studying grasping postures. an application to power and precision grasp of cylinders. *Applied Ergonomics*, 56:52–61.
- Jarque-Bou, N. J., Atzori, M., and Müller, H. (2020a). A large calibrated database of hand movements and grasps kinematics. *Scientific data*, 7(12):1–10.
- Jarque-Bou, N. J., Scano, A., Atzori, M., and Müller, H. (2019). Kinematic synergies of hand grasps: a comprehensive study on a large publicly available dataset. *Journal of neuroengineering and rehabilitation*, 16:1–14.

- Jarque-Bou, N. J., Vergara, M., Sancho-Bru, J. L., Gracia-Ibanez, V., and Roda-Sales, A. (2020b). Hand kinematics characterization while performing activities of daily living through kinematics reduction. *IEEE Trans Neural Syst Rehabil Eng*, 28(7):1556–1565.
- Kamper, D. G., Cruz, E. G., and Siegel, M. P. (2003). Stereotypical fingertip trajectories during grasp. *Journal of Neurophysiology*, 90(6):3702–3710.
- Kapandji, I. A. (2007). *The physiology of the joints: volume one the upper limb*. Churchill Livingstone.
- Kayola, G., Mataa, M. M., Asukile, M., Chishimba, L., Chomba, M., Mortel, D., Nutakki, A., Zimba, S., and Saylor, D. (2023). Stroke rehabilitation in low- and middle-income countries: Challenges and opportunities. *American Journal of Physical Medicine & Rehabilitation*, 102(2S):S24–S32.
- Khan, S. M., Khan, A. A., and Farooq, O. (2024). An early force prediction control scheme using multimodal sensing of electromyography and digit force signals. *Heliyon*, 10(8):e28716.
- Kladarić, M. (2024). Development of rehabilitation glove: soft robotic approach. Master’s thesis, University of Rijeka. Faculty of Engineering.
- Konrad, P. (2006). *The ABC of EMG - A practical introduction to kinesiological electromyography*, volume 1. Noraxon U.S.A. Inc.
- Koo, T. K. and Li, M. Y. (2016). A guideline of selecting and reporting intraclass correlation coefficients for reliability research.
- Lang, C. E., Lohse, K. R., and Birkenmeier, R. L. (2015). Dose and timing in neurorehabilitation: Prescribing motor therapy after stroke. *Current Opinion in Neurology*, 28(6):549–555.
- Li, R., Wang, H., and Liu, Z. (2022). Survey on mapping human hand motion to robotic hands for teleoperation. *IEEE Transactions on Circuits and Systems for Video Technology*, 32(5):2647–2665.
- Luraschi, J., Kuo, K., and Ruiz, E. (2019). *Mastering Spark with R: the complete guide to large-scale analysis and modeling*. O’Reilly Media.
- Ma, R., Zhang, L., Li, G., Jiang, D., Xu, S., and Chen, D. (2020a). Grasping force prediction based on semg signals. *Alexandria Engineering Journal*, 59(3):1135–1147.
- Ma, R., Zhang, L., Li, G., Jiang, D., Xu, S., and Chen, D. (2020b). Grasping force prediction based on semg signals. *Alexandria Engineering Journal*, 59(3):1135–1147.
- Maier, M., Ballester, B. R., and Verschure, P. F. M. J. (2019). Principles of neurorehabilitation after stroke based on motor learning and brain plasticity mechanisms. *Frontiers in Systems Neuroscience*, 13.
- Majidi, C. (2014). Soft robotics: a perspective—current trends and prospects for the future. *Soft robotics*, 1(1):5–11.

- Martinez, I. J. R., Mannini, A., Clemente, F., and Cipriani, C. (2020a). Online grasp force estimation from the transient EMG. *IEEE Transactions on Neural Systems and Rehabilitation Engineering*, 28(10):2333–2341.
- Martinez, I. J. R., Mannini, A., Clemente, F., Sabatini, A. M., and Cipriani, C. (2020b). Grasp force estimation from the transient EMG using high-density surface recordings. *Journal of Neural Engineering*, 17(1):016052.
- Meurer, A., Smith, C. P., Paprocki, M., Čertík, O., et al. (2017). SymPy: symbolic computing in python. *PeerJ Computer Science*, 3:e103.
- Mezić, I. (2005). Spectral properties of dynamical systems, model reduction and decompositions. *Nonlinear Dynamics*, 41:309–325.
- Mezić, I. (2021). Koopman operator, geometry, and learning of dynamical systems. *Not. Am. Math. Soc*, 68(7):1087–1105.
- Mohammadi, A., Lavranos, J., Choong, P., and Oetomo, D. (2018). Flexo-glove: a 3d printed soft exoskeleton robotic glove for impaired hand rehabilitation and assistance. In *2018 40th Annual International Conference of the IEEE Engineering in Medicine and Biology Society (EMBC)*, pages 2120–2123. IEEE.
- Mukaka, M. M. (2012). Statistics corner: A guide to appropriate use of correlation coefficient in medical research.
- Muschter, E., Schulz, J., Tömösközi, M., Herbst, L., Küssel, L., Sefunç, M., Holtzhausen, S., Speidel, S., Fitzek, F. H. P., and Li, S.-C. (2023). Coming in handy: Ceti-age - a comprehensive database of kinematic hand movements across the lifespan. *Scientific Data*, 10(1).
- Nieminen, P. (2022). Application of standardized regression coefficient in meta-analysis. *BioMedInformatics*, 2(3):434–458.
- Ninapro, T. (2020). Ninapro — ninapro.hevs.ch. <https://ninapro.hevs.ch/>. [Accessed 07-01-2025].
- Olson, B., Hashmi, I., Molloy, K., and Shehu, A. (2012). Basin hopping as a general and versatile optimization framework for the characterization of biological macromolecules. *Advances in Artificial Intelligence*, 2012:1–19.
- O’Sullivan, S. B., Schmitz, T. J., and Fulk, G. (2019). *Physical Rehabilitation*. FA Davis.
- Pasvanti, N., Psarros, A., Korbetis, G., Vlahinos, A., and Mihailidis, A. (2019). Lattice structures modeling: introduction to homogenization. In *Proceedings of the 8th before reality conference. Munich, Germany*.
- Patel, R. M. and Bartholomew, J. (2021). Impact of job resources and job demands on burnout among physical therapy providers. *International Journal of Environmental Research and Public Health*, 18(23):12521.
- Peng, Z. and Huang, J. (2019). Soft rehabilitation and nursing-care robots: A review and future outlook. *Applied sciences*, 9(15):3102.

- Polygerinos, P., Wang, Z., Galloway, K. C., Wood, R. J., and Walsh, C. J. (2015). Soft robotic glove for combined assistance and at-home rehabilitation. *Robotics and Autonomous Systems*, 73:135–143.
- Prevete, R., Donnarumma, F., d’Avella, A., and Pezzulo, G. (2018). Evidence for sparse synergies in grasping actions. *Scientific reports*, 8(1):616.
- Proulx, C. E., Beaulac, M., David, M., Deguire, C., Haché, C., Klug, F., Kupnik, M., Higgins, J., and Gagnon, D. H. (2020). Review of the effects of soft robotic gloves for activity-based rehabilitation in individuals with reduced hand function and manual dexterity following a neurological event. *Journal of Rehabilitation and Assistive Technologies Engineering*, 7.
- Prusa Research, a. (2023). Original prusa i3 mk3s handbook. https://cdn.prusa3d.com/downloads/manual/prusa3d_manual_mk3s_en.pdf. [Accessed 24-03-2025].
- Rousseeuw, P. J. and Hubert, M. (2011). Robust statistics for outlier detection. *Wiley interdisciplinary reviews: Data mining and knowledge discovery*, 1(1):73–79.
- Rus, D. and Tolley, M. T. (2015). Design, fabrication and control of soft robots. *Nature*, 521(7553):467–475.
- Saltelli, A., Annoni, P., Azzini, I., Campolongo, F., Ratto, M., and Tarantola, S. (2010). Variance based sensitivity analysis of model output. Design and estimator for the total sensitivity index. *Computer Physics Communications*, 181(2):259–270.
- Schmid, P. J. (2022). Dynamic mode decomposition and its variants. *Annual Review of Fluid Mechanics*, 54(1):225–254.
- Siavashani, A. G., Yousefi-Koma, A., and Vedadi, A. (2023). Estimation and early prediction of grip force based on sEMG signals and deep recurrent neural networks. *Journal of the Brazilian Society of Mechanical Sciences and Engineering*, 45(5).
- Sobinov, A. R. and Bensmaia, S. J. (2021). The neural mechanisms of manual dexterity. *Nature Reviews Neuroscience*, 22(12):741–757.
- Sobol, I. (2001). Global sensitivity indices for nonlinear mathematical models and their monte carlo estimates. *Mathematics and Computers in Simulation*, 55(1–3):271–280.
- Stegeman, D. F., Blok, J. H., Hermens, H. J., and Roeleveld, K. (2000). Surface emg models: properties and applications. *Journal of Electromyography and Kinesiology*, 10(5):313–326.
- Tarantola, S., Gatelli, D., and Mara, T. (2006). Random balance designs for the estimation of first order global sensitivity indices. *Reliability Engineering & System Safety*, 91(6):717–727.
- Tay, J. K., Narasimhan, B., and Hastie, T. (2023). Elastic net regularization paths for all generalized linear models. *Journal of statistical software*, 106.
- Virtanen, P., Gommers, R., Oliphant, T. E., Haberland, M., et al. (2020). SciPy 1.0: fundamental algorithms for scientific computing in python. *Nat Methods*, 17(3):261–272.

- Wales, D. J. and Doye, J. P. K. (1997). Global optimization by basin-hopping and the lowest energy structures of lennard-jones clusters containing up to 110 atoms. *The Journal of Physical Chemistry A*, 101(28):5111–5116.
- Welmer, A., Holmqvist, L., and Sommerfeld, D. (2008). Limited fine hand use after stroke and its association with other disabilities. *Journal of Rehabilitation Medicine*, 40(8):603–608.
- Wickham, H., Averick, M., Bryan, J., Chang, W., McGowan, L. D., François, R., Grolemund, G., Hayes, A., Henry, L., Hester, J., et al. (2019). Welcome to the tidyverse. *Journal of open source software*, 4(43):1686.
- Wu, C., Cao, Q., Fei, F., Yang, D., Xu, B., Zhang, G., Zeng, H., and Song, A. (2021). Optimal strategy of semg feature and measurement position for grasp force estimation. *PLOS ONE*, 16(3):e0247883.
- Yan, Y., Goodman, J. M., Moore, D. D., Solla, S. A., and Bensmaia, S. J. (2020). Unexpected complexity of everyday manual behaviors. *Nature Communications*, 11(1).
- Yi, J., Chen, X., and Wang, Z. (2017). A three-dimensional-printed soft robotic glove with enhanced ergonomics and force capability. *IEEE Robotics and Automation Letters*, 3(1):242–248.
- Young, J. C., Olson, E., Do, T., Shuman, M., Ohta, D., and Han, Y.-L. (2024). Spider legs inspired soft robotic extensor for hand rehabilitation. In *2024 IEEE International Conference on Advanced Robotics and Its Social Impacts (ARSO)*, pages 80–85. IEEE.
- Zhang, D. and Hannaford, B. (2019). IKBT: Solving symbolic inverse kinematics with behavior tree. *Journal of Artificial Intelligence Research*, 65:457–486.
- Zhang, H., Wang, X., Yang, L., Feng, L., Hui, D., and Zhai, Y. (2023). Structural lightweight design of thermoplastic polyurethane elasticity fabricated by fused deposition modeling. *Journal of Materials Engineering and Performance*, 33(21):11992–12009.
- Zhang, N., Li, K., Li, G., Nataraj, R., and Wei, N. (2021). Multiplex recurrence network analysis of inter-muscular coordination during sustained grip and pinch contractions at different force levels. *IEEE Transactions on Neural Systems and Rehabilitation Engineering*, 29:2055–2066.
- Zhang, N., Zhao, Y., Gu, G., and Zhu, X. (2022). Synergistic control of soft robotic hands for human-like grasp postures. *Science China Technological Sciences*, 65(3):553–568.

Nomenclature

Roman Symbols

a	SPA overall length
$A_{\text{eq,seg}}$	Equivalent cross-sectional area of bellows segment
a_{i-1}	Distance from local frame z_{i-1} to z_i along x_{i-1}
α_j	Koopman amplitude
A_{rect}	Area of rectangular base
A_{semi}	Area of hollow semicircular annulus
B	Intercept of the linear relationship
b	SPA connecting segment 1 length
b_i, b_{i+1}	Lower and upper limits defining a subregion
b_j, b_{j+1}	Lower and upper limits for the first time delay shift
b_k, b_{k+1}	Lower and upper limits for the second time delay shift
β_n	Fitted coefficient for linear dependence on number of ribs
β_ϑ	Fitted coefficient for quadratic dependence on bending angle
c	SPA connecting segment 2 length
c_Θ	Parametric angle coefficient for end-moment loading
c_ϑ	Coefficient relating beam end angle to pseudo-rigid-body angle
d_i	Link offsets
dA_{rib}	Differential area element of a rib
Δt	Discrete time step

dF_{rib}	Differential force due to pressure on a rib
$\Delta L_{\text{Total},i}$	Total elongation of MCP, PIP, and DIP bellow segments
dM_{seg}	Differential moment acting on a rib
$L_{\text{DIP,TIP}}$	Distance between <i>DIP</i> joint and fingertip
E	Matrix containing the lifted realizations of e_i
E	Young's modulus of the material
$E(\cdot)$	Expected value operator
e_0	Initial state of the EMG signal
e_i	Processed EMG signal
$e_{\mathbb{I},S_{ijk},\tau_1,\tau_2}[n]$	Gridded indicator observable
$e_{\text{td}(j)}$	Time-delayed observable at step j
$e_{\text{td}(n)}[1 + \tau_1]$	Time-delayed observable at step $1 + \tau_1$
$e_{\text{td}(n)}[1 + \tau_2]$	Time-delayed observable at step $1 + \tau_2$
F	State transition function
G	Matrix containing the lifted realizations of g_i
g	Reported grip force
$G_{e,\text{int}}$	Interaction component of the input data matrix
$G_{e,\text{lift}}$	Koopman-lifted interaction data matrix
$g_{e,\text{lift}(i)}$	Snapshot of lifted interaction terms
\hat{g}	Estimated grip force
g_{raw}	Raw dynamometer signal
i, j	Indices
$I_{\text{rect,centroid}}$	Second moment of area about centroid of rectangular base
I_{rect}	Adjusted second moment of area of rectangular base
I_{semi}	Second moment of area of hollow semicircular annulus
I_{total}	Total second moment of area combining annulus and base

K	Slope of linear relationship between parent and dependent joint angles
$k - folds$	Number of folds in cross-validation
$K_{\vartheta 1,i}, K_{\vartheta 2,i}$	Coefficients for pressure terms in bending angle model
$K_{L1,i}, K_{L2,i}$	Coefficients for pressure terms in elongation model
K_{DIP}	Coefficient linking <i>DIP</i> flexion to <i>MCP</i> joint
K_{PIP}	Coefficient linking <i>PIP</i> flexion to <i>MCP</i> joint
K_{seg}	Bending stiffness coefficient of ribbed bellow segment
K_{Θ}	Equivalent torsional spring stiffness
ℓ	Number of retained Koopman modes
L_i	Segment lengths representing distances between joint centers
ΔL_{axial}	Axial elongation due to internal pressure
$\Delta L_{bending}$	Bending elongation caused by deformation
L_i, L_{i+1}	Inter-joint distances between two consecutive joints
L_{seg}	Length of ribbed bellow segment
ΔL_{total}	Total elongation combining axial and bending contributions
M, N	Distinct spaces in the mapping
M_{bsg}	Moment acting on a ribbed segment
$L_{MCP,PIP}$	Distance between <i>MCP</i> and <i>PIP</i> joints
M_{rib}	Moment per rib due to internal pressure
M_{seg}	Total moment acting on ribbed segment
n	General count variable (e.g., sample size, dataset length, number of origins, state space dimension)
$n_{r,bsg}$	Number of ribs in a ribbed segment
$n_{r,seg}$	Number of ribs per segment
p -value	probability of observing the data under the null hypothesis
P_i^{i-1}	Translation vector

p_{seg}	Internal pressure applied to bellow actuator segments
$L_{\text{PIP,DIP}}$	Distance between <i>PIP</i> and <i>DIP</i> joints
p_y	Position coordinate in the <i>y</i> -direction
p_z	Position coordinate in the <i>z</i> -direction
<i>r</i> -correlation	Correlation coefficient
R_i^{i-1}	Rotational matrix
R_b	Outer radius of hollow semicircular annulus
r_b	Inner radius of hollow semicircular annulus
$R_{b,\text{eq}}$	Equivalent outer radius of hollow semicircular annulus
r_{ij}	Rotation matrix element related to <i>MCP</i> joint motion
R_{seg}	Outer radius of projected surface
r_s	Simplified rotational parameter for transformation equations
r_{seg}	Inner radius of projected surface
S_{ijk}	Subregion in a discretized grid
T_i^{i-1}	General transformation matrix
τ	Time horizon for future predictions
t_b	Thickness of reinforcing layer
ϑ_i	Cumulative bending angle at end of <i>i</i> -th bellow segment
ϑ_{i-1}	Cumulative bending angle at end of (<i>i</i> − 1)-th bellow segment
δ_x	Horizontal deflection of beam tip
δ_y	Vertical deflection of beam tip
ϑ	Beam end angle as function of applied moment
w	Observation weight
\mathbf{x}	State vector
\bar{x}_i	Mean of variable x_i
x_i	Axis along common perpendicular or perpendicular to plane containing both axes

y	Dependent variable
\hat{y}_i	Predicted dependent joint value
y_i	Observation of the dependent joint
Z	Matrix containing Ritz vectors
z_i	Axis of revolution for the i -th joint

Greek Symbols

α_{i-1}	General rotation angle between coordinate axes
β_{EI}	Quadratic correction term in bending angle model
β_i	Inclination angles in the FE plane
β_s^γ	Regularized coefficient
β_s^{OLS}	OLS (Ordinary Least Squares) coefficient
β_{s0j}	Intercept for subject j from set S , representing subject-to-subject variability
β_{si}	Standardized coefficient
$\chi_{S_{ijk}}(e_{\text{td}(n)}, \tau_1, \tau_2)$	Indicator function for determining grid membership
Δd_i	Link elongation for segment i
γ	Mixing parameter for regularization; characteristic radius factor in PRB
\mathcal{K}	Koopman operator
$\bar{\mathcal{K}}$	Estimate of the static Koopman operator
Λ	Diagonal matrix of Ritz values
λ	Tuning parameter
λ_j	Ritz value (eigenvalue) of the Koopman operator
$\mathcal{O}_M, \mathcal{O}_N$	Observable spaces corresponding to M and N
ϕ	Vector of functions used to lift e_i
ψ	Vector of functions used to lift g_i
σ_r^2	Residual variance

σ_s^2	Variance of random effects (subject intercepts)
σ_{x_i}	Standard deviation of variable x_i
τ_1, τ_2	Time delays between chosen data points
Θ	Pseudo-rigid-body angle approximating beam deformation
θ_i	Joint angles
$\theta_{\text{CMC,FE}}$	Flexion/Extension angle of the CMC joint
$\theta_{\text{dependent}}$	Angular position of the dependent joint
$\theta_{\text{DIP,FE}}$	Flexion/Extension angle of the DIP joint
$\theta_{\text{MCP,AA}}$	Abduction/Adduction angle of the MCP joint
$\theta_{\text{MCP,FE}}$	Flexion/Extension angle of the MCP joint
θ_{parent}	Angular position of the parent joint
$\theta_{\text{PIP,FE}}$	Flexion/Extension angle of the PIP joint
ϑ_i	Bending end angle for MCP, PIP, and DIP bellow segments
u_{joint}	Composite angle for joint motion
z_j	Ritz vector (eigenvector) of the Koopman operator

Acronyms / Abbreviations

AA	Abduction/Adduction
ADL	Activities of Daily Living
ASTM	American Society for Testing and Materials
BH	Basin Hopping
CMC	Carpometacarpal Joint
CMR	Common Mode Rejection
DC	Direct Current offset
DH	Denavit-Hartenberg
DIP	Distal Interphalangeal Joint
DOF	Degree of Freedom

EMG	Electromyography
FDM	Fused Deposition Modeling
FE	Flexion/Extension
FEM	Finite Element Method
FFT	Fast Fourier Transform
GLM	Generalized Linear Model
ICC	Intraclass Correlation Coefficient
I	Index Finger
IKBT	Inverse Kinematics Behavior Tree
IK	Inverse Kinematic
IP	Interphalangeal Joint
IQR	Interquartile Range
KOT	Koopman Operator Theory
LBD	Lower Bound Deficit
LH	Latin Hypercube
L	Little Finger
LME	Linear Mixed-Effects Model
LSTM	Long Short-Term Memory
MA	Moving Average
MCP	Metacarpophalangeal Joint
M	Middle Finger
MUAP	Motor Unit Action Potentials
MU	Motor Units
MVC	Maximum Voluntary Contraction
NA	Missing Values (Not Available)
OIML	International Organization of Legal Metrology

OLS	Ordinary Least Squares
PCA	Principal Components Analysis
PIP	Proximal Interphalangeal Joint
PLA	Polylactic Acid
POP	Points of Rotation
PRB	Pseudo Rigid Body
Q1	First Quartile
Q3	Third Quartile
RBD	Randomized Block Design
RMSE	Root Mean Square Error
RMS	Root Mean Square
ROM	Range of Motion
ROS	Robot Operating System
RP	Reference Point
R	Ring Finger
SA	Sensitivity Analysis
sEMG	Surface Electromyography
SI	Sensitivity Indices
SPA	Soft Pneumatic Actuator
TIP	Fingertip
TMC	Trapeziometacarpal Joint
TPU	Thermoplastic Polyurethane
TRL	Technology Readiness Level
T	Thumb Finger
UBD	Upper Bound Deficit
wMAE	Weighted Mean Absolute Error
wwMAPE	Double Weighted Mean Absolute Percentage Error

List of Figures

1.1	Visual overview of the thesis structure	8
2.1	Placement of sEMG electrodes near flexor carpi ulnaris muscle	15
2.2	Signal processing steps for obtaining optimal processed EMG	17
2.3	Preliminary grouped Sobol sensitivity analysis: sensitivity indices	19
2.4	Preliminary sensitivity analysis: projections of Latin hypercube sampling	20
2.5	Iterative multi-step sensitivity analysis and optimization: projections of Latin hypercube sampling	22
2.6	Iterative sensitivity analysis and optimization via frequency component refinement	23
2.7	The effect of sparsity constraints during modeling using gridded indicator observables	28
2.8	Three-dimensional representation of gridded indicator observables	29
2.9	Hyperparameter tuning of Koopman prediction algorithm	34
2.10	Optimized spectral mask for processing EMG signals at both positions P1 and P2	35
2.11	Examples of all signals relevant for grip force modeling - raw and processed EMG signals, estimates, smoothed estimates, forecasts, and measured grip force.	40
3.1	23 ADL grasps and functional movements (Jarque-Bou et al., 2020a)	48
3.2	Joint angle data preprocessing steps	50
3.3	Subject-finger contingency tables	52
3.4	Hierarchical data nesting procedure for dependency correlation analysis	53
3.5	Correlation distributions for intra-finger joint dependencies	54
3.6	Identification of 116 highly correlated intra-finger dependencies	56
3.7	Subject representation in intra-finger dependencies	57

3.8	Data Summary for Dependency-Movement Relationships	58
3.9	ICC and Variance of Random Effects	63
3.10	Summary of Selected Predictors in LME Models	64
3.11	Examples of LME Model Fitting	65
3.12	Summary of Error Metrics	66
3.13	Agglomerative Clustering of Models	68
3.14	Clustered Models Coefficients	70
4.1	Index finger: AA and FE approximation planes and kinematics	77
4.2	Modified DH forward kinematics convention	78
4.3	Kinematic analysis	87
4.4	Cross-sectional design and dimensions of the SPA	90
4.5	Boundary conditions applied to the SPA	91
4.6	Discretized SPA	93
4.7	MCP, DIP, PIP, and TIP location points	94
4.8	FEM Analysis of SPAs	95
4.9	FEM simulation of I and L SPAs in FE plane	96
4.10	Linear regression of joint constraints for index and little fingers	98
4.11	Forces and moments acting on bellows segments due to pressurization, along with a simplified geometric surface approximation	100
4.12	Approximation of the rib cross-section relevant for the second moment of area computation	103
4.13	Pseudo-rigid-body moment-motion approximation of a ribbed elastic segment	105
4.14	Comparison of FEM and PRB modeled bending	113
4.15	Assembling the rehabilitation glove	115
4.16	Soft-Robotic Glove	115
A.1	Raw sEMG measurements, grip force and processed EMG data: P1	144
A.2	Raw sEMG measurements, grip force and processed EMG data: P2	145
B.1	Standardized Coefficient Values with Interactions	148
B.2	Standardized Coefficient Values with Random Effects	149
B.3	Weighted Mean Absolute Error (WMAE)	150
B.4	Double Weighted Mean Absolute Percentage Error (WWMAPE)	151

List of Tables

2.1	Summary of 2-factor RBD experiment.	15
2.2	Optimal hyperparameters for the grip force forecasting model	33
2.3	Mean peak cross-correlations summary statistics after final SA step	34
2.4	Summary of peak cross-correlations and lags for EMG–grip force signals	37
2.5	wMAPE for grip force estimation from EMG across all measurements, including means and effects	38
2.6	wMAPE for grip force forecasting from EMG across all measurements, including means and effects	38
2.7	Assessing the significance of subject and position effects on estimation and forecasting wMAPE	39
3.1	Hand kinematic dataset: subject and experiment identifiers	46
3.2	Grouping data structure for boxplot and summary data on grasping.	49
3.3	Anatomical ROM limits for digit joints during FE movement	51
3.4	Pairwise intra-finger joint dependencies investigated for kinematic model reduction	53
3.5	DOF reductions across 23 grasps with intra-finger dependencies	69
4.1	Finger-specific parameters for the index finger measured from the 50 th percentile male model.	76
4.2	Modified DH parameters for a human finger.	79
4.3	Intra-joint FE dependency coefficients and ROMs.	81

4.4	Inter-finger AA dependency coefficients ROMs	81
4.5	Palmar arc chained dependency (CMC FE) coefficients and ROMs. . .	81
4.6	Modified DH parameters for SPA.	88
4.7	Dimensions of SPAs for different fingers.	90
4.8	Compression of inter-joint distances for the index and little fingers. . .	97
4.9	Linear regression coefficients for joint angles (ϑ) and link elongations (ΔL_{total}) for the index and little fingers.	99
4.10	Variable specific step size multiplication factors in BH optimization. . .	111
4.11	PRB model optimization limits and optimal parameters.	112

Appendix A

Raw sEMG Measurements, Grip Force and Processed EMG Data

This appendix is related to Section 2.2 and Subsection 2.4.2 of Chapter 2. Recordings of grip force measurements and raw EMG signals from all experimental runs are available in this appendix, providing a complete dataset for verification and further analysis across different subjects and sensing positions.

The appendix contains panel plots displaying all recorded data from the 2-factor randomized block design experiment involving 13 male participants (subjects ac, dp, ds, js, lb, lk, lm, ln, md, mm, nk, pb, ss) aged 22 to 24 years. For each subject, measurements were taken at two distinct forearm sensing positions (P1 and P2) near the flexor carpi ulnaris muscle, with two replications per position, resulting in a total of 52 experimental runs.

Figure A.1 presents data collected from position P1, while Figure A.2 shows data from position P2. Each panel displays three synchronized signals: raw sEMG data (labeled emg), simultaneously collected grip force measurements (labeled grip), and processed EMG signals (labeled proc). Above each panel is an experiment identifier consisting of subject abbreviation, position, replication number, and signal type.

These visualizations allow direct comparison of signal characteristics across different subjects, with varying grip levels (100, 75, 50, 25 and 0% of maximum voluntary contraction). The data illustrate the transient phases during grip force changes and the steady-state plateaus.

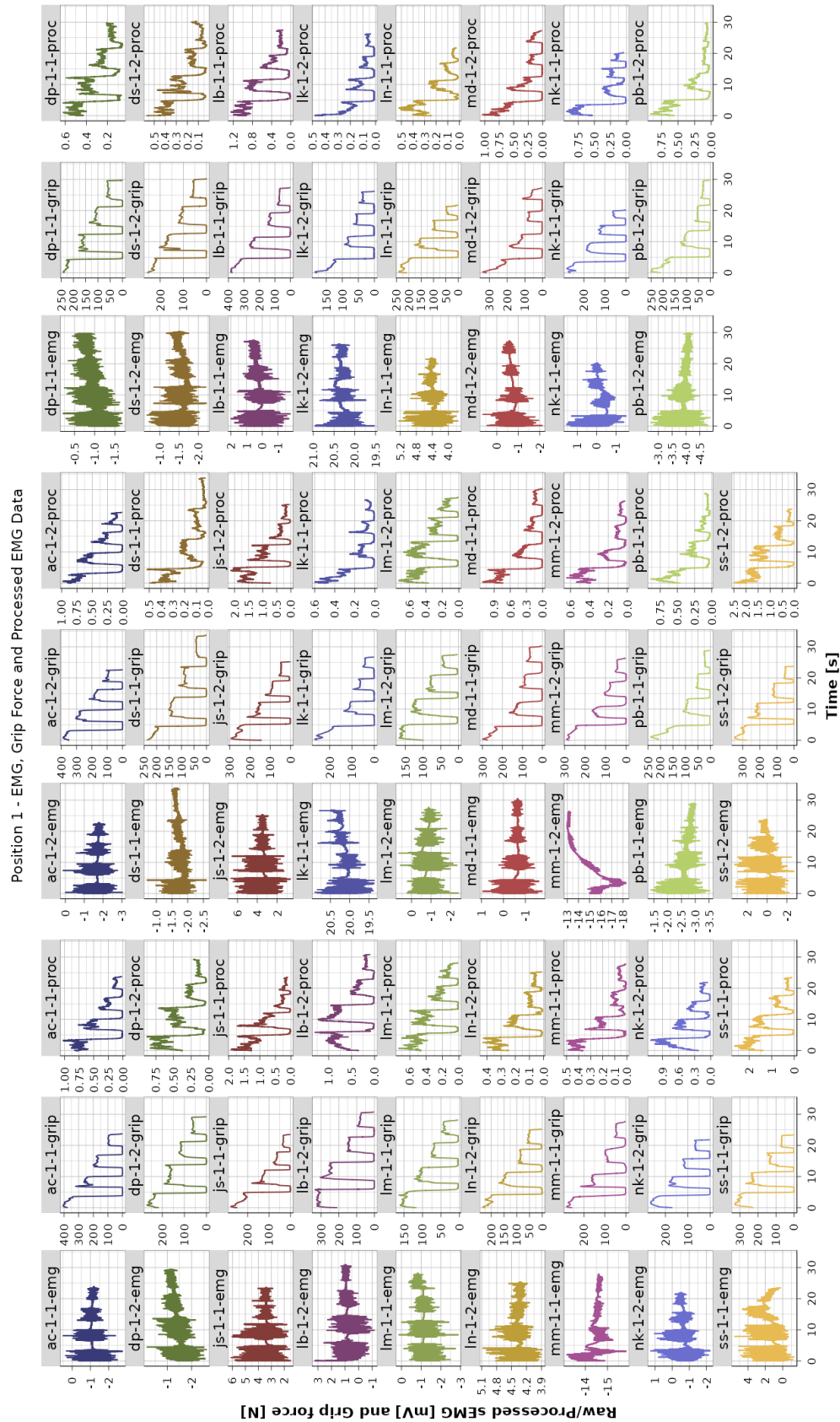


Figure A.1 Raw sEMG measurements, grip force and processed EMG data: Position P1

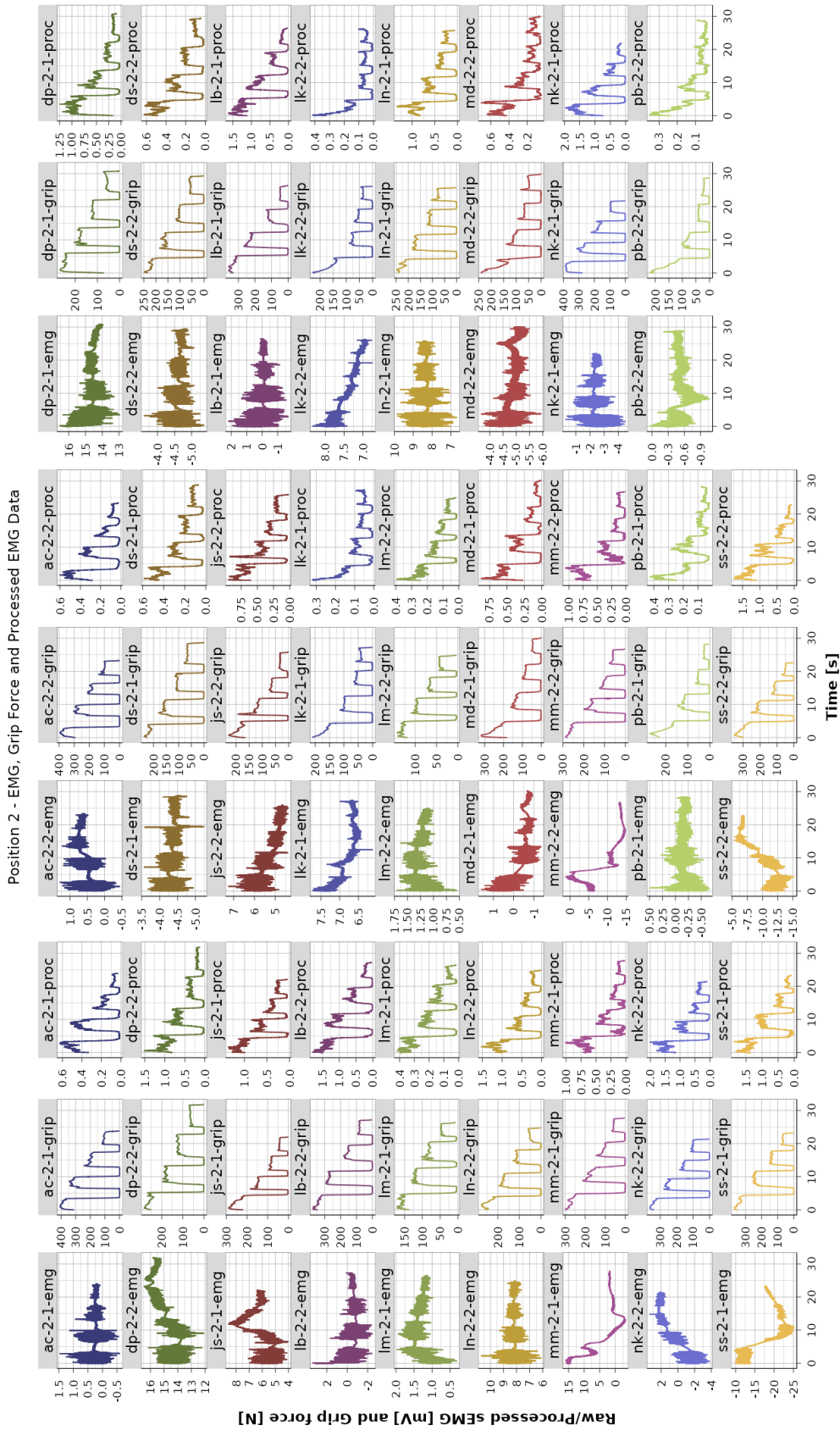


Figure A.2 Raw sEMG measurements, grip force and processed EMG data: Position P2

Appendix B

LME Model Coefficients' Detailed Analysis and Model Error Metric Analyses

This Appendix is related to Section 3.3 of the Chapter 3.

Figures B.1 and B.2 present the standardized coefficients obtained from the LME models across all 116 dependency-movement relationships. When combined, these figures provide a complete overview of the modeled coefficients.

Figure B.2 focuses on linear (*lin*) and polynomial (*poly*) coefficients, including the mean subject intercept as a random effect for all models. In contrast, Figure B.1 also includes up to seven additional model coefficients beyond *lin* and *poly*. The following predictors were found to be both significant and have medium-to-high effect sizes:

- Subject height, or its transformed interaction with other predictors, in 9 out of 116 models,
- Transformed subject weight in interaction with other predictors, in 4 out of 116 models.

For users intending to apply these model coefficients, it is recommended to standardize the variables before use. The scaling and centering of the dependent variable y should be back-transformed using either self-acquired means and standard deviations or the values provided in Table S3 online¹.

¹<https://docs.google.com/spreadsheets/d/122Wf7zkGHR6pxZarTTlsNggakPIXNvEhUHNhUbmZEPA/edit?usp=sharing>

Figure B.3 presents a detailed analysis of the weighted mean absolute error (wMAE), while Figure B.4 shows the double weighted mean absolute percentage error (wwMAPE) on both the training and testing datasets for all 116 models, using both GLM and LME methods. The error metrics are calculated according to Equations (3.6) and (3.7) in Subsection 3.3.2. For readers' convenience, a detailed table representation of these results is available in Table S1 online².

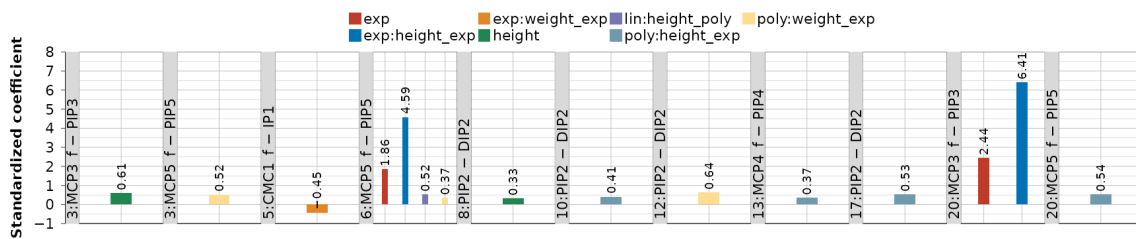


Figure B.1 Standardized coefficient values for modeled dependencies that comprise linear (*lin*) and/or polynomial (*poly*) and other predictors and interactions: exponential (*exp*), height, and weight (“:” denotes interaction).

²<https://docs.google.com/spreadsheets/d/1JkbfzyNAdGuZEg0mXhJGEHl9DEgz nLNN34KvTpnEcuQ/edit?usp=sharing>

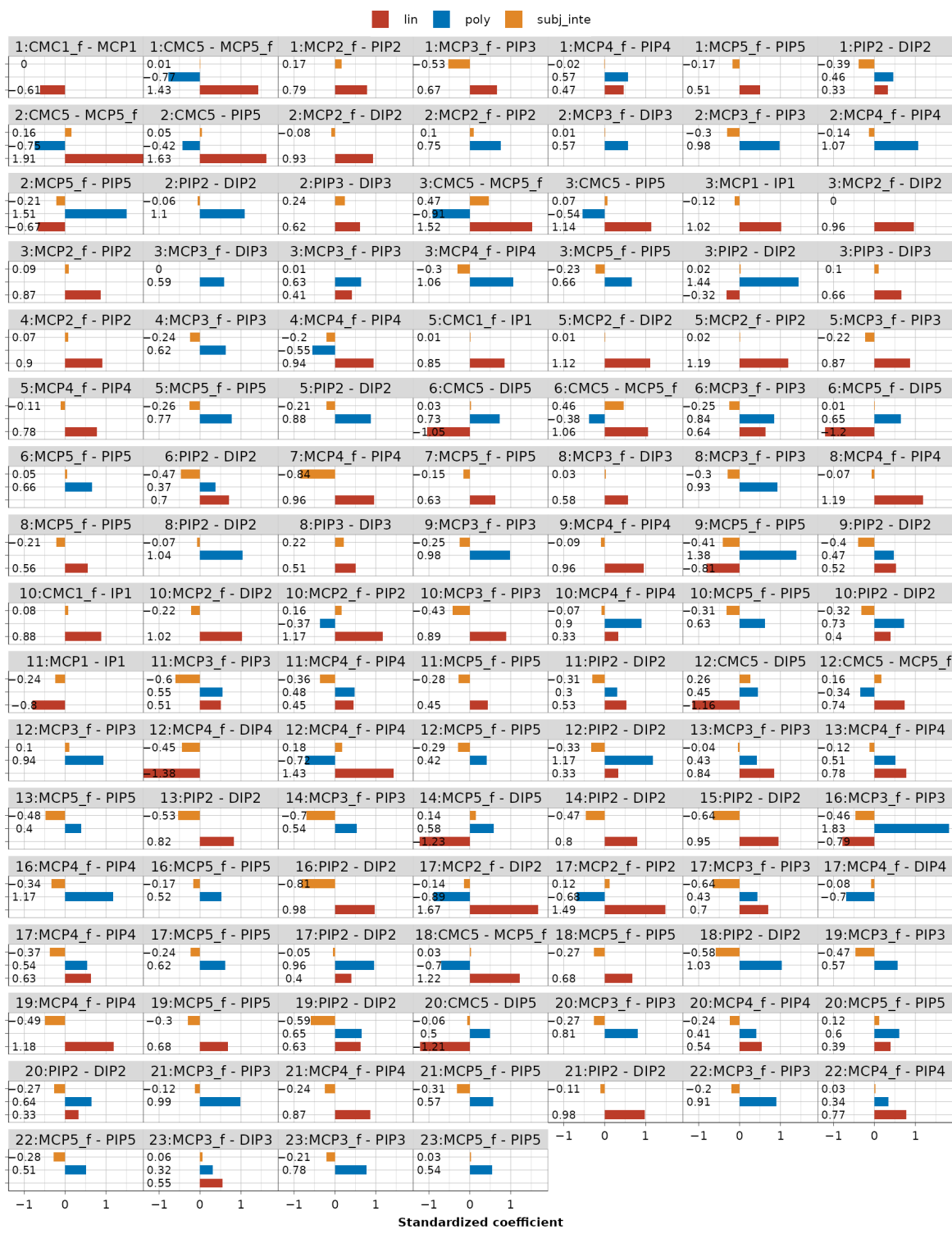


Figure B.2 Standardized coefficient values for all modeled dependencies that consist of random effects—subject intercept (*subj_inte*)—and fixed effects—linear (*lin*) and polynomial (*poly*).

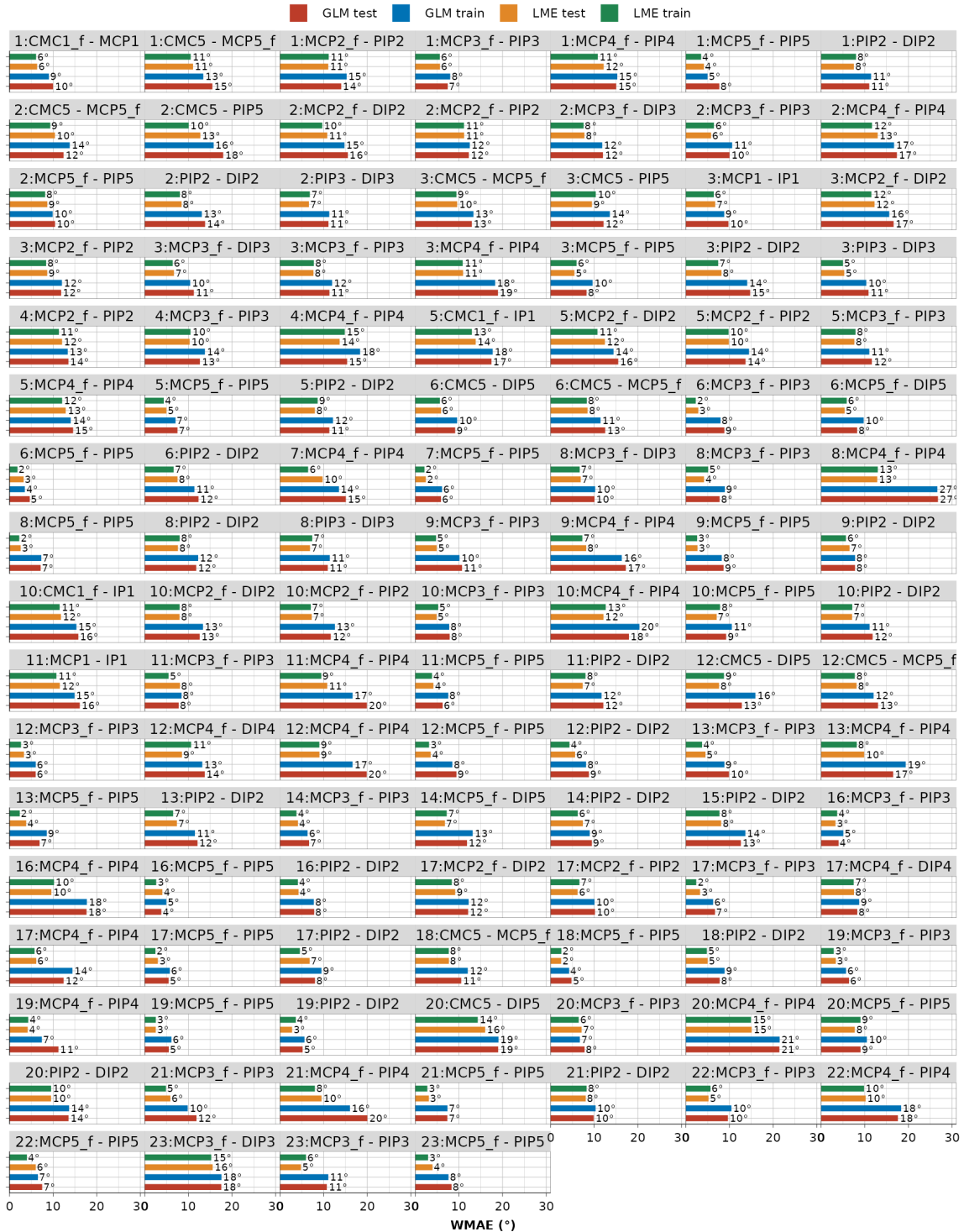


Figure B.3 Weighted mean absolute error (WMAE) on train and test datasets across all 116 modeled dependencies for both GLM and LME models.

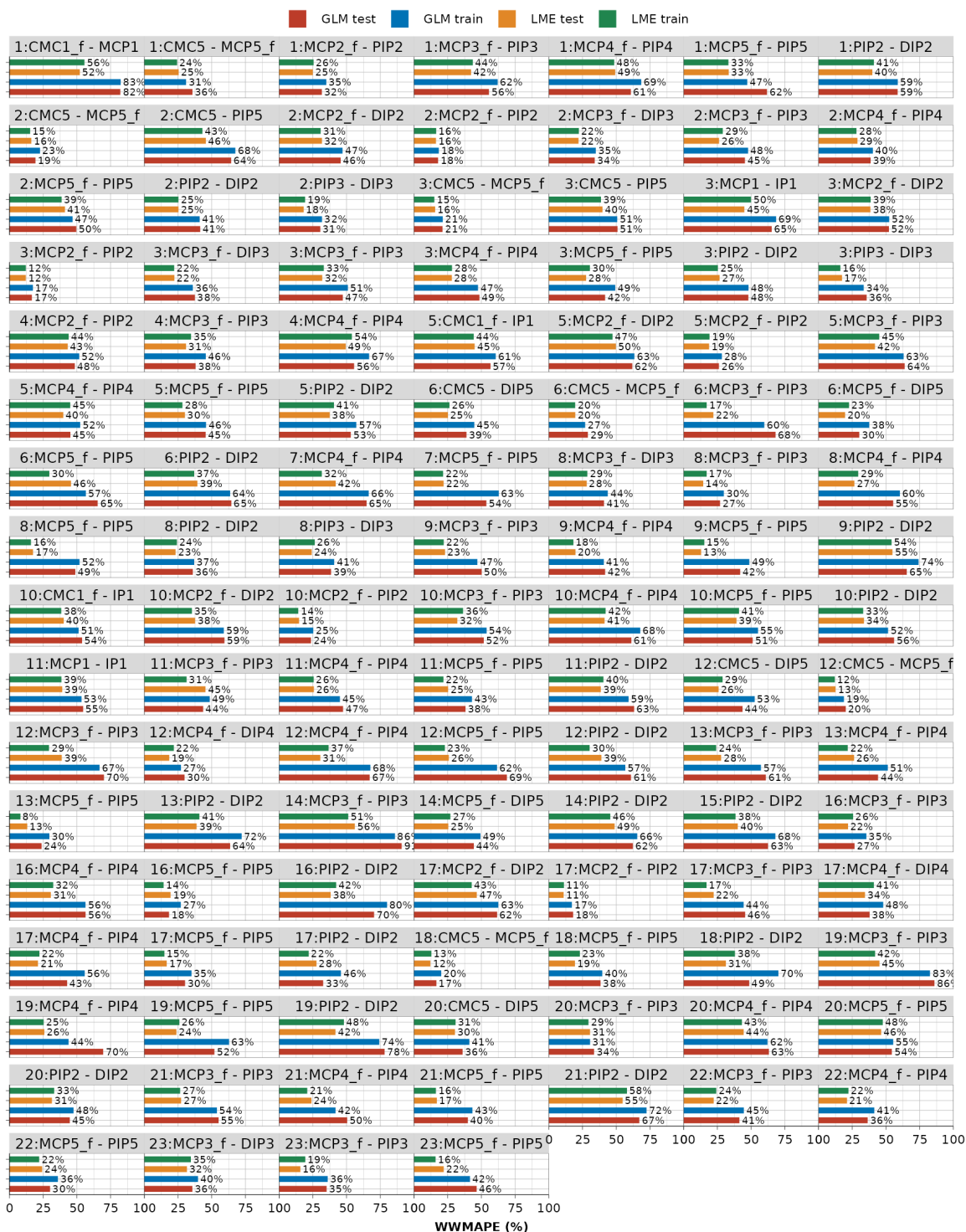


Figure B.4 Double weighted mean absolute percentage error (WWMAPE) on train and test datasets across all 116 modeled dependencies for both GLM and LME models.

Curriculum Vitae

Tomislav Bazina, born in 1991, is a researcher and PhD candidate specializing in data science applications for rehabilitation robotics. He graduated from Tin Ujevic High School in Kutina (2005 to 2009), studying Natural Sciences and Mathematics. After initial studies at the University of Zagreb's Faculty of Mechanical Engineering and Naval Architecture (2009 to 2014), he earned his Bachelor's degree in Mechanical Engineering at the University of Rijeka, Faculty of Engineering (RITEH) (2014 to 2016). He then completed his Master's in Mechanical Engineering at RITEH (2016 to 2019), specializing in Technology Computational Engineering. Since 2019, he has pursued a Postgraduate Doctoral Study in Mechanical Engineering at RITEH. His achievements include a Croatian National Foundation for Student Standard Support scholarship, an Excellence Scholarship from the University of Rijeka, a Dean's Award, and 3rd place at Big Bang Camp, a program for transforming technology into marketable products.

From 2013 to 2019, while pursuing his academic studies, Tomislav gained industry experience as a CAD/CAM/CNC programmer. He began at Hidraulika Kutina d.d. (2013 to 2017), creating programs for CNC lathe control units. After working as a CNC Operator at Elcon Geraetebau d.o.o. (April-June 2015), he joined Mandic Machining (2018 to 2019), where he prepared 3D CAD models and 2D manufacturing drafts, performed CAM-driven machining on CNC lathe and milling machines, and conducted product quality control. Concurrently, he worked as a student Peer Tutor (2015 to 2019) for several courses at RITEH.

Since 2019, Tomislav has been working as a Research and Teaching Assistant at RITEH, contributing to research at the university's centers for Micro and Nano Sciences and Technologies (NANORI) and Artificial Intelligence and Cybersecurity (AIRI). He conducts design tutorials for Control of Mechatronics Systems, Components of Mechatronics Systems, Machine Elements Design I and II, and Laboratory Exercises A and B. He collaborated with Končar D&ST (2019 to 2021) on power transformer vibration analysis. His doctoral research applies data-driven methods to characterize

grip strength and grasp-oriented kinematics, developing a soft robotic glove for hand rehabilitation. He has authored or co-authored five journal articles, eight international conference proceedings, two conference abstracts, and two technical reports, supported by grants from the Air Force Office of Scientific Research and the University of Rijeka.

Since 2022, Tomislav has been providing consulting services in AI/ML solutions engineering, designing and developing solutions for fraud risk analysis, anomaly detection, and data-driven modeling. He has open-sourced three Robot Operating System packages: one for hand and upper limb skeletal models with reduced kinematics, and two for interfacing and real-time signal processing of hand dynamometer and surface electromyography (sEMG) sensors. His additional open-source contributions include software tools for optimizing turning processes and manufacturing multi-part flow line configuration, machine vision-based inspection and metrology, ML-based product detection and recognition, power transformer vibration analysis, hand grasping trajectory analysis, and hand grip-sEMG signal relationship analysis.

Outside of his professional work, Tomislav is a proud husband and father.

List of Publications

Journal Articles

1. Bazina, T., Mauša, G., Zelenika, S., & Kamenar, E. (2024). Reducing Hand Kinematics by Introducing Grasp-Oriented Intra-Finger Dependencies. *Robotics*, 13(6), 82.
2. Bazina, T., Kladarić, M., Kamenar, E., & Gregov, G. (2024). Development of Rehabilitation Glove: Soft Robot Approach. *Actuators*, 13(12), 472.
3. Bazina, T., Kamenar, E., Fonoberova, M., & Mezić, I. (2024). Koopman-driven grip force prediction through EMG sensing. *arXiv preprint arXiv:2409.17340*. (In the process of publication to *IEEE TNSRE*).
4. Bazina, T., Kamenar, E., Zelenika, S., Črnjarić-Žic, N., et al. (2022). Hand model with dependency constrained joints for applications in rehabilitation robotics. *Medicina*, 58(4), 385-398.
5. Ištoković, D., Perinić, M., Doboviček, S., & Bazina, T. (2019). Simulation framework for determining the order and size of the product batches in the flow shop: A case study. *Advances in Production Engineering & Management*, 14(2), 166-176.

Conference Proceedings

1. Bazina, T., Zelenika, S., Mauša, G., & Kamenar, E. (2024). Rehabilitation-oriented human hand model reductions. *24th International EUSPEN Conference*, 77-78.
2. Bazina, T., Kamenar, E., Zelenika, S., & Schnurrer Luke Vrbanić, T. (2023). Grasp-oriented human hand model for use in rehabilitation robotics. *23rd International EUSPEN Conference*, 297-298.
3. Bazina, T., Zelenika, S., Kamenar, E., Schnurrer Luke Vrbanic, T., & Kristina, M. (2022). Reachability analysis and simulation of a forearm rehabilitation device. *Proceedings of 22nd International Conference and Exhibition, EUSPEN 2022*.
4. Bazina, T., Kamenar, E., Vrcan, Ž., Perčić, M., Zelenika, S., Ćučić, B., & Ilijašević, M. (2021). Characterisation of the dynamical behaviour of a power transformer's tank. *Proceedings of the 37th Danubia Adria Symposium*, 23-24.
5. Bazina, T., Zelenika, S., Kamenar, E., Škifić, A., & Schnurrer-Luke-Vrbanić, T. (2021). Kinematic characterization and validation of an upper limb rehabilitation device. *Proceedings of the 21st International Conference of the European Society for Precision Engineering and Nanotechnology*.
6. Bazina, T., Zelenika, S., Kamenar, E., & Schnurrer-Luke-Vrbanić, T. (2020). Critical validation of design strategies for a compact upper limb mechatronics rehabilitation device. *Proceedings of the 20th international conference of the EUSPEN*.
7. Bazina, T., Marković, M., Pavletić, D., & Jurković, Z. (2017). Primjena strojnog vida za detektiranje i prepoznavanje proizvoda dobivenih ubrizgavanjem u kalup. *7 International Conference Mechanical Technologies and Structural Materials*.
8. Bazina, T., Jurković, Z., & Sekulić, M. (2017). Optimizacija procesa tokarenja. *Proceedings of conference with international participation Application of new technologies and ideas in engineering education*, 113-120.

Conference Abstracts

1. Bazina, T., Kamenar, E., Zelenika, S., Schnurrer-Luke-Vrbanić, T., Škifić, A., et al. (2021). Structured open-source procedure for the design and validation of an arm rehabilitation device. *Congress of European Forum for Research in Rehabilitation*, 86-86.

2. Bazina, T., Kamenar, E., & Zelenika, S. (2020). Upper limb mechatronics rehabilitation device. *Book of Abstracts - My First Conference 2020 - 4th Annual PhD Conference*.

Technical Reports

1. Bazina, T., Kamenar, E., Zelenika, S., Perčić, M., Vrcan, Ž., Čučić, B., & Ilijašević, M. (2021). Measurement and analysis of vibrations of power transformers aimed at noise reduction.
2. Bazina, T., Kamenar, E., Vrcan, Ž., Perčić, M., & Zelenika, S. (2019). Report on the measurement performed on a Končar D&ST power transformer by the Precision Engineering Laboratory of the Faculty of Engineering - University of Rijeka.